TESTING THE STANDARD MODEL WITH TOP-QUARK PRODUCTION

BY

ZACK EDWARD SULLIVAN

B.A., Johns Hopkins University, 1993
M.S., University of Illinois at Urbana-Champaign, 1994

THESIS

Submitted in partial fulfillment of the requirements
for the degree of Doctor of Philosophy in Physics
in the Graduate College of the
University of Illinois at Urbana-Champaign, 1998

Urbana, Illinois

TESTING THE STANDARD MODEL WITH TOP-QUARK PRODUCTION

Zack Edward Sullivan, Ph.D.
Department of Physics
University of Illinois at Urbana-Champaign, 1998
Scott S. Willenbrock, Advisor

Now that the existence of the top quark is firmly established, attention turns to measuring its properties. Because of its large mass, the top quark may be sensitive to physics beyond the standard model. A promising candidate for this new physics is supersymmetry. Hence, we calculate the supersymmetric QCD correction to top-quark production at the Fermilab Tevatron, allowing for arbitrary left-right mixing of the squarks. We find that the correction is significant for several combinations of gluino and squark masses, e.g. $+33\%$ for $m_{\widetilde{g}} = 200$ GeV, $m_{\widetilde{t}} = m_{\widetilde{q}} = 75$ GeV.

Single-top-quark production at hadron colliders provides an opportunity to directly probe the charged-current weak interaction of the top quark. We calculate the next-to-leading-order corrections to single-top-quark production via W-gluon fusion at the Fermilab Tevatron, the CERN Large Hadron Collider, and DESY HERA. Using a b-quark distribution function to sum collinear logarithms, we show that there are two independent corrections, of order $1/\ln(m_t^2/m_b^2)$ and α_s. This observation is generic to processes involving a perturbatively derived heavy-quark distribution function at an energy scale large compared with the heavy-quark mass.

Using the next-to-leading-order results for the W-gluon fusion cross section, we analyze the possibilities for studying single-top-quark production at the Tevatron and LHC. We find that there may be evidence for single-top-quark production in Run I data. Run II at the Tevatron should allow the W-gluon fusion cross section to be measured to $\pm 22\%$ with 2 fb^{-1} of

data. The LHC will have a statistical resolution of $\pm 2\%$ with the first 1 fb^{-1} of data. The

implications of these results for measuring V_{tb} and top-quark spin polarization are discussed.

To my parents

and my wife Vivian

Acknowledgments

First, and foremost, I would like to thank my advisor, Scott Willenbrock, for his direction and encouragement. From our many long discussions I have learned how phenomenology is really done. I would like to thank my collaborator, Tim Stelzer, for sharing his understanding of perturbative physics and numerical analysis, and for his friendship.

I wish to thank my mother, Lana Shaw Levine, and father, James Ferguson Sullivan, for their constant support and dedication. They encouraged my curiosity in all things, and taught me to always look a bit further. I have received from them my character and my strength. My most heart-felt thanks go to my wife, Vivian Slager Sullivan. Her love, devotion, and support have brought me to where I am.

I am grateful to all of my teachers, friends, and everyone who has challenged me to re-examine my beliefs.

Table of Contents

List of Tables

List of Figures

Chapter 1

Introduction

Our best understanding of the strong, weak, and electromagnetic forces of Nature is contained in a theory called the standard model. This theory has been tested over a large range of energies, and has been found to provide accurate predictions for physical processes over distance scales of several orders of magnitude. One of these predictions was the existence of a new particle, called the top quark. The top quark was discovered in 1995 by two separate experimental collaborations at the Fermi National Accelerator Laboratory (Fermilab) [1,2].

According to the standard model, there are three types of fundamental particles: leptons, quarks, and gauge bosons. There are six known leptons, which are paired into three families:

$$\begin{pmatrix} \nu_e \\ e \end{pmatrix} \quad \begin{pmatrix} \nu_\mu \\ \mu \end{pmatrix} \quad \begin{pmatrix} \nu_\tau \\ \tau \end{pmatrix}. \tag{1.1}$$

These are the electron (e), muon (μ), tau (τ), and their associated neutrinos (ν). The leptons interact through the electroweak force of Nature. The electric charge is 0 for the neutrinos, and -1 for the particles in the lower half of the doublets above. There are also six known quarks, which are are paired:

$$\begin{pmatrix} u \\ d \end{pmatrix} \quad \begin{pmatrix} c \\ s \end{pmatrix} \quad \begin{pmatrix} t \\ b \end{pmatrix}. \tag{1.2}$$

These are called the up (u), down (d), charm (c), strange (s), top (t), and bottom (b). The

electric charge is $+2/3$ for the particles in the upper half of the doublets above, and $-1/3$ for the particles in the lower half. The weak force mixes these particle states through the Cabibbo-Kobayashi-Maskawa (CKM) matrix [3]. The quarks also have a color charge quantum number associated with the strong force. The leptons and quarks are fermions, which have half-integer spin quantum number and obey Fermi-Dirac statistics.

The gauge bosons are the mediators of the forces of Nature. They have integer spin quantum number and obey Bose-Einstein statistics. The gluon (g) mediates the strong force. The W^+, W^-, and Z^0 are associated with the weak force. The photon (γ) carries the electromagnetic force. These forces are described by a $SU(3)_C \times SU(2)_L \times U(1)_Y$ gauge theory, where the $SU(3)_C$ Lie algebra describes the strong force interactions of quantum chromodynamics (QCD), and the weak and electromagnetic forces are unified into an electroweak force, described by the $SU(2)_L \times U(1)_Y$ Lie algebra. The standard model describes how the $SU(2)_L \times U(1)_Y$ symmetry of the theory breaks down into the weak force, and quantum electrodynamics (QED).

The fermions are massless until electroweak symmetry breaking occurs. The standard model postulates that fermions acquire a mass proportional to their Yukawa couplings to another fundamental boson, called the Higgs (H). As of yet, there is no evidence for the existence of the Higgs boson. However, the most massive particles would interact the most strongly with a Higgs. Hence, studying the interactions of the most massive particles may provide a window into this area of physics.

Now that the top quark has been discovered, its properties are being accurately measured. The cross section for top-quark pair production has been measured to $\pm 25\%$, and the mass to $\pm 3\%$ [4]. Run II at the Fermilab Tevatron, and experiments at the CERN Large

Hadron Collider (LHC), will measure the top-quark cross section to $\pm 6\%$, and the top-quark mass to ± 2 GeV [5].[1] The current world-averaged value for the top-quark mass is $m_t = 174.1 \pm 5.4$ GeV [6]. The Yukawa coupling $Y_t = m_t(2\sqrt{2}G_F)^{1/2}$ is 1.0 given the current central value of the top-quark mass. This is a hint that new physics may couple strongly to the top quark.

The purpose of this thesis is to examine the use of measurements of the properties of the top-quark to test the standard model of physics. A compelling hypothesis for physics beyond the standard model is provided by adding a symmetry to the theory called supersymmetry. At hadron colliders, top-quark pairs are produced via the strong force. In Chapter 2 [7], we present a study of how supersymmetric corrections to QCD would affect the $t\bar{t}$ production cross section. Single-top-quark production proceeds via the charged weak interaction. Because it has the largest cross section, most single-top-quark events at the Fermilab Tevatron, and the CERN LHC, will be produced via W-gluon fusion. In order to normalize the data, we present the first complete and correct calculation of the next-to-leading-order (NLO) cross section for single-top-production via W-gluon fusion in Chapter 3 [8]. In order to extract the properties of the top quark from single-top-quark production, experimenters will have to do an accurate analysis of their detector acceptances, and the backgrounds. Chapter 4 [9] describes an improved method for the detection of these single-top-quark events. We discuss the theoretical issues that must be addressed, and give an indication of how well the electroweak properties of the top quark can be measured. Some of the most important results in particle physics in the next decade may come from these studies of the properties of the top quark.

---

[1]Note that here, and throughout the rest of this thesis, we work in units where $\hbar = 1$, and $c = 1$.

1.1   Supersymmetric extensions of the standard model

Despite its remarkable success, the standard model is generally not considered to be very satisfying. The model contains eighteen free parameters that comprise masses, mixing angles, and coupling constants. The drive to reduce the number of free parameters, and the observation that the coupling constants almost meet when their values are run to near the Planck scale, has led to the introduction of many extensions to the standard model. One of these classes of models is supersymmetry (SUSY). The symmetry of supersymmetry associates fermionic and bosonic degrees of freedom. Though this may seem to be relating two fundamentally different types of fields, very nice properties emerge in a supersymmetric world (or in one where SUSY is softly broken).

The standard model postulates that electroweak symmetry breaking occurs when a fundamental scalar doublet obtains a vacuum expectation value (*vev*) *v* via the Higgs mechanism. Supersymmetry modifies this model slightly by adding at least one more Higgs doublet, and the associated fermionic partners. While at first this may seem to be a step in the wrong direction, investigating the SUSY Higgs sector provides many of the reasons to take supersymmetry seriously. Two of the more compelling reasons are that supersymmetry can provide solutions to the "gauge hierarchy" and "naturalness" problems that plague the standard model.

In the standard model, the electroweak scale is characterized by the mass of the weak particles, namely m_Z of $O(100 \text{ GeV})$. If the gauge symmetries $SU(3)_C \times SU(2)_L \times U(1)_Y$ are unified, this will occur at some scale M_X on the order of 10^{15}–10^{19} GeV, the GUT or Planck scale. The "hierarchy" problem consists of two parts. The first is that at tree level it

4

is expected that the ratio of the *vev v* to the breaking scale M_X should be on the order of 1, specifically $Cv/M_X = 1$ for some constant C. Of course the Z boson mass is on the order of *v*, so this implies that C must be enormous for the Higgs mechanism to still apply. Why this constant is so large rather than equal to one is unexplained. The next question to arise is how to stabilize this ratio against large radiative corrections. This is the "fine-tuning" problem of how to consistently alter C at every order in perturbation theory.

In specific models of supersymmetry both of these questions are addressed naturally, but the technical question of how to keep $v \ll M_X$ is answered in all reasonable SUSY models. The Higgs mechanism occurs at tree level in a SUSY theory, and thus *v* is of $O(M_{SUSY})$. It was proven by Witten [10] that if supersymmetry is not broken at the tree level, then it is not broken at any order in perturbation theory. Hence perturbative radiative corrections will not spoil the tree-level hierarchy of scales (i.e. *v* remains of $O(M_{SUSY})$). Supersymmetry must be broken, but this is achieved through non-perturbative effects that leave the tree-level result unbroken. When soft SUSY breaking occurs at a scale $M_{SUSY} = 10^2$–10^3 GeV, the applicable ratio is $Cv/M_{SUSY} = 1$, and C is of $O(1)$. The non-perturbative mechanism that produces this breaking scale is yet to be explained, and is a well motivated subject for it own reasons.[2]

One of the original motivations for investigating supersymmetry was its solution to the "naturalness" problem. The standard model has three types of particles: fermions, gauge bosons, and Higgs-like scalars. The fermions are naturally light because their masses are protected by a chiral symmetry. The gauge bosons are light because of their gauge symmetries. The scalars, however, do not have any associated symmetry, and so their renormalized

---

[2]Most models of SUSY breaking also produce a relationship to gravity.

masses tend to be large. Therefore a light Higgs is unnatural.[3] Explicitly, $m_H^2 = m_0^2 + \delta m_H^2$

diverges quadratically, where δm_H^2 is due to the self-coupling loop in the scalar propagator.

$$\delta m_H^2 \sim \int^\Lambda \frac{d^4k}{k^2 - m_H^2} \sim \Lambda^2 \tag{1.3}$$

Supersymmetry adds a fermionic partner $\widetilde{H}$ whose mass is degenerate with m_H. Therefore

there is also a contribution due to the fermion loop of

$$\delta m_H^2 \sim -Tr \int^\Lambda \frac{d^4k}{(\not{k} - m_{\widetilde{H}})(\not{k} + \not{q} - m_{\widetilde{H}})} \sim -\Lambda^2 \tag{1.4}$$

that cancels the scalar piece.[4] In unbroken supersymmetry this cancelation is exact, and the

mass of the fundamental scalars is not renormalized. Softly breaking supersymmetry splits

the masses of the particles and their superpartners, but the quadratic divergences still cancel.

The bare mass m_0 is small, and the renormalized mass is of $O(M_{SUSY})$, or about 1 TeV.

Despite sufficient theoretical motivation, contact with experiment must still be made if

supersymmetry is to be anything more than a toy model. Unfortunately, there are over 100

free parameters in the most general supersymmetric theory. Therefore, in order to attain

any sort of predictive power, certain constraints are generally placed on the models studied.

The most practical model is the minimal supersymmetric standard model (MSSM). This is

a direct supersymmetrization of the standard model.

The particle spectrum of the MSSM contains three generations of chiral quark and lepton

superfields, the vector superfields for the $SU(3)_C \times SU(2)_L \times U(1)_Y$ gauge group, and two

chiral Higgs doublet superfields.[5] An added assumption of unification at some scale M_X is

---

[3]The t' Hooft definition of "natural" is that if taking the mass of a particle to zero increases the symmetry of the Lagrangian, it is "natural" for the particle to be light.

[4]The minus sign is for the closed fermion loop. The exact details depend on the interaction terms from a particular model's superpotential.

[5]Two doublets are needed to cancel the hypercharge anomalies between the higgsinos, and to give masses to both up and down type fermions. The later arises because the Lagrangian may not be constructed out of conjugate fields.

generally included. This forces the masses of the scalar-quarks (squarks) and scalar-leptons (sleptons), and the gauge partners (gauginos) to attain masses of m_0 and $m_{1/2}$, respectively, at the unification scale. This also fixes the bilinear and trilinear breaking coefficients to some unified values [11]. Likewise, gauge unification is assumed at $M_X \simeq 10^{16}$ GeV, and this occurs generally as long as m_0 and $m_{1/2}$ do not exceed ~ 10 TeV. Finally, R-parity is assumed to be conserved, which implies sparticles are produced in pairs. This forces the lightest supersymmetric particle (LSP) to be stable.

1.1.1 Direct searches for supersymmetry

Assumptions about unification are useful for symmetry breaking arguments, but the low energy phenomenology beckons for more directly observable quantities. As such, the parameters of the MSSM are usually chosen to be: the top squark and gluino masses, the ratio of the *vev*'s of the two Higgs doublets $\tan\beta \equiv v_2/v_1$, the Higgs mass parameter μ, and the charged Higgs mass. The LSP is almost always considered to be the lightest neutralino $\widetilde{\chi}_1^0$, which is a mixture of mostly photino and some higgsino. Table 1.1 lists the spectrum of the MSSM in terms of both mass and interaction eigenstates.

Direct experimental limits on supersymmetry are mostly based on data from the CERN e^+e^- collider LEP and the Fermilab Tevatron. Searches for supersymmetry are generally performed separately for top squarks $\widetilde{t}$, the light-quark superpartners $\widetilde{q}$, and gluinos $\widetilde{g}$. This is motivated by the minimal supergravity models which argue that all scalar particles acquire a mass on the order of the SUSY breaking scale (see Sec. 1.1 and [13, 14]). A heavy top-quark loop dominates the running of the masses to low energies, forcing the mass of the two top squarks below that of the rest of the squarks [11]. Additionally, mixing of the left-right

7

Table 1.1: The MSSM physical spectrum in terms of both mass eigenstates and interaction eigenstates. The nomenclature is chosen to be identical with that of Haber and Kane [12].

Particles	Weak Interaction Eigenstates		Mass Eigenstates	
Symbol	Symbol	Name	Symbol	Name
$q = u,d,s$ c,b,t	$\widetilde{q}_L, \widetilde{q}_R$	scalar-quark	$\widetilde{q}_1, \widetilde{q}_2$	scalar-quark
$\ell = e,\mu,\tau$	$\widetilde{\ell}_L, \widetilde{\ell}_R$	scalar-lepton	$\widetilde{\ell}_1, \widetilde{\ell}_2$	scalar-lepton
$\nu = \nu_e, \nu_\mu, \nu_\tau$	$\widetilde{\nu}$	scalar-neutrino	$\widetilde{\nu}$	scalar-neutrino
g	$\widetilde{g}$	gluino	$\widetilde{g}$	gluino
$W^\pm$	$\widetilde{W}^\pm$	wino		
H_1^+	$\widetilde{H}_1^+$	higgsino	$\widetilde{\chi}_{1,2}^\pm$	charginos
H_2^-	$\widetilde{H}_2^-$	higgsino		
γ	$\widetilde{\gamma}$	photino		
Z^0	$\widetilde{Z}^0$	zino	$\widetilde{\chi}_{1,2,3,4}^0$	neutralinos
H_1^0	$\widetilde{H}_1^0$	higgsino		
H_2^0	$\widetilde{H}_2^0$	higgsino		

Table 1.2: Current experimental limits on superparticle masses from direct searches.

Sparticle	Limit	Notes	Source
$\widetilde{t}$	> 67 GeV	Any $\theta_{\widetilde{t}}$; Any decay	ALEPH [16]
	> 65 GeV	channel	OPAL [17]
	> 70 GeV	Preliminary	ALEPH [18]
$\widetilde{q}$	> 176 GeV	$m_{\widetilde{g}} < 300$ GeV; with cascade decays	D0 [19]
	> 224 GeV	$m_{\widetilde{g}} < m_{\widetilde{q}}$; with cascade decays	CDF [20]
	> 74 GeV	$B(\widetilde{q} \to q\widetilde{g} \text{ or } q\widetilde{\gamma}) = 1$	UA2 [6]
	> 45 GeV	$Z \to \widetilde{q}\bar{\widetilde{q}}$	DELPHI [6]
$\widetilde{g}$	> 154 GeV	Any $m_{\widetilde{q}}$; with cascade	CDF [20]
	> 144 GeV	decays	D0 [19]

weak eigenstates of the top squarks may result in the top squark $\widetilde{t}_1$ becoming the lightest squark [15]. The most recent experimental limits on the masses of the top-squark, the light-quark superpartners, and the gluino are presented in Table 1.2. Other regions of parameter space have been eliminated [21,22], but these limits are highly model dependent [14]. Further constraints on the mass spectrum are derived from cosmological considerations and indirect searches, such as B_0-$\bar{B}_0$ mixing [23].

The limits in Table 1.2 are currently the least model dependent results available. However, the remaining assumptions do leave room for the limits to be relaxed [24]. The most important assumption in these searches is a value for $\tan\beta$. This ratio is between 2 and $m_t/m_b \simeq 35$,[6] and is usually chosen to be between 2 and 4 at hadron colliders. It was shown

---

[6]See Drees and Martin [11] for motivation of these limits.

[25] that the limits on the gluino $\widetilde{g}$, "heavy squark" $\widetilde{q}$, and other superparticle masses are far less stringent for values of $\tan\beta = 2$ than for $\tan\beta = 30$. This is an important point since we must choose appropriate values for the masses in Chapter 2. Since our calculation does not depend on $\tan\beta$, and in order to allow for the widest range of allowed parameter space, we use the most conservative limits of $m_{\widetilde{l}}, m_{\widetilde{q}} > 50$ GeV from the lepton colliders, and $m_{\widetilde{g}} > 150$ GeV.

The next generation of accelerators should cover a large region of the allowed supersymmetry parameter space. The potential for discovery of Higgs bosons and the electroweak superpartners (charginos, neutralinos, and sleptons) is greatest at e^+e^- colliders. For charged particles, limits may be placed on the masses at roughly $\sqrt{s}/2$ minus a few percent from threshold effects. A Higgs can be discovered up to a mass of roughly $\sqrt{s} - 100$ GeV. Most sparticles are expected to have masses below 1 TeV, but the unification bound only necessitates that they be less than ~ 10 TeV. One notable exception is the lightest Higgs h^0 which cannot exceed ~ 125 GeV.[7] If no Higgs is found below ~ 150 GeV, supersymmetry will either have to be abandoned or some new physics will have to occur between the SUSY breaking scale and the GUT scale.

While the extraction of SUSY parameters is more model dependent at hadron colliders, they are more suited to the search for squarks and gluinos because of the high masses of colored superpartners and their strong coupling [26]. Exhaustive direct searches will reach 300 GeV for gluinos and 100 GeV for top squarks with 10 fb^{-1} of data at the Tevatron [5]. The chargino/neutralino reach is 150–250 GeV [25]. Until the advent of the CERN Large Hadron Collider, the presence of heavier SUSY particles will only be suggested by their

---

[7]Preliminary ALEPH results from the 183 GeV run at LEP indicate $m_{h^0} > 64.5$ GeV [18].

effects on standard model processes.

1.1.2   An indirect search for supersymmetry via top-quark production

Given the model dependence and other limitations of doing a full direct search at current energies, another approach to observing supersymmetry is desirable. One approach is to see how quantum corrections due to superparticles change the standard model predictions. The largest corrections would be expected to arise in the strong force since its coupling constant at low energies is the highest. Measuring cross sections of strong processes might therefore yield some interesting results.

Heavy scalar propagators tend to suppress radiative corrections by the square of the scalar mass. Since the top squarks are expected to be the lightest squarks, we expect the top-quark cross section to exhibit the largest supersymmetric corrections. (Prospects for observing this are explored in detail in Chapter 2.) In contrast to the direct searches for su-persymmetry of Sec. 1.1.1, the model dependence of these corrections is greatly reduced. None of the assumptions about SUSY breaking, or unification, or values of $\tan\beta$ are needed. If R-parity is conserved, only the physical masses of the top squarks, the heavy squarks, and the gluinos, and the mixing for the top squarks and the heavy squarks are required. This leaves seven parameters, not dozens, to describe all of the SUSY QCD enhancement to the $t\bar{t}$ cross section.

1.2   Single-top-quark production

Single-top-quark production provides a unique opportunity to study the charged-current weak-interactions of the top quark. Within the standard model, this process provides the best

direct measurement of the Cabibbo-Kobayashi-Maskawa matrix element V_{tb}. The spin of

the top quark can be measured via its decay products, and compared with the standard model

prediction. Beyond the standard model, this process is sensitive to fourth generation quarks,

new top-quark decay channels, supersymmetry, technicolor, effective $V + A$ interactions,

and more (see e.g. [27–35]).

The only diagonal Cabibbo-Kobayashi-Maskawa (CKM) matrix element which has not

been measured directly is V_{tb}. Despite this, in the context of three generations, V_{tb} is the

most constrained CKM element. The 90% confidence level constraint $0.9991 \leq |V_{tb}| \leq$

0.9994 is the result of the small values of $|V_{ub}|$ and $|V_{cb}|$, combined with the unitarity require-

ment $|V_{ub}|^2 + |V_{cb}|^2 + |V_{tb}|^2 = 1$ [6]. Limits from indirect measurements are currently much

weaker. CLEO measurements of B_0–$\overline{B}_0$ mixing place a three generation limit of $|V_{tb}| > 0.76$,

assuming that no new physics occurs [6].

If the possibility of new physics at the Wtb vertex is considered, then the lower limit on

$|V_{tb}|$ from unitarity is relaxed, and $|V_{tb}|$ becomes almost entirely unconstrained, $0 < |V_{tb}| \leq$

0.9994 [6]. A direct measurement of $|V_{tb}|$ can therefore explore the possibility of new physics

(e.g. a fourth generation). Furthermore, a measurement of $|V_{tb}|^2 > 0.5$ will confirm that the

quark recently discovered at the Tevatron is indeed the SU(2) partner of the bottom quark.

The first analysis of V_{tb}, done by CDF, focused on $t\bar{t}$ pairs, since they dominate the top-

quark data sample. In $t\bar{t}$ production, $|V_{tb}|$ determines the branching fraction B of top quarks

which decay into bottom quarks ($t \rightarrow Wb$) compared with other kinematically-allowed quark

decays ($t \rightarrow Wq$):

$$B \equiv \frac{|V_{tb}|^2}{|V_{td}|^2 + |V_{ts}|^2 + |V_{tb}|^2} . \tag{1.5}$$

The current result from CDF is $B = 0.94 \pm 0.27(stat) \pm 0.13(syst)$ [36]. Unitarity of the

CKM matrix requires that the denominator be less than or equal to one even if there are more than three generations. Therefore the CDF measurement of B provides an *upper bound* on V_{tb} of $|V_{tb}|^2 \leq B$. If B is measured to be a bit less than one this would be a major discovery, since three generation unitarity requires $|V_{tb}| > 0.9991$. However, if B is measured to be consistent with one, V_{tb} remains unconstrained, and could be significantly less than one.

Since the measured branching fraction in $t\bar{t}$ production is really a ratio of double b-tagged events to single b-tagged events, it is possible that new physics might mimic both signals, removing the sensitivity of B to V_{tb}. It has been shown that supersymmetric production of top squarks, and decays of $(t \to \tilde{t}_1)$, can pass the top-quark analysis [37]. In this case, the measured branching fraction may not be used to extract $|V_{tb}|$, even if there are only three generations.

The non-exotic case of a fourth generation poses a clearer problem with using $t\bar{t}$ production to extract $|V_{tb}|$. In this case, unitarity implies $|V_{td}|^2 + |V_{ts}|^2 + |V_{tb}|^2 + |V_{tb'}|^2 = 1$, and the denominator of B can be anything less than one. Thus, if $|V_{tb}| < 1$, and $V_{td}, V_{ts} \ll 1$, B will be one and provide no information about V_{tb}. This is familiar from b physics where the branching ratio $B(b \to c) \simeq 1$, even though $V_{cb} \ll 1$. It is therefore important to study other processes which can provide additional information on $|V_{tb}|$.

Single-top-quark production is the best process for measuring $|V_{tb}|$ at hadron colliders. The production cross section is proportional to $|V_{tb}|^2$ and therefore provides a direct measurement of $|V_{tb}|$. Experiments actually measure $\sigma(t) \times B(t \to Wb)$. Since the branching ratio is at most 1.0, measuring $\sigma(t) \times B(t \to Wb)$ provides a *lower bound* on $|V_{tb}|$.

This lower bound can be improved to an equality by combining information from $t\bar{t}$ production and single-top-quark events. The $t\bar{t}$ cross-section experiments really measure

13

$\sigma(t\bar{t}) \times B^2(t \to Wb)$. The branching ratio $B(t \to Wb)$ can be extracted by comparing the calculated cross section with the observed cross section. Then this branching ratio can be input into the single-top-quark analysis to obtain a direct measurement of $|V_{tb}|$. In addition to strengthening the lower bound to an equality, this combination tends to reduce systematic effects, such as uncertainties in the luminosity and the top-quark mass.

In order to perform the analyses required to extract information from single-top-quark production, the experimenters will need to have accurate calculations of the cross sections. There are three modes of single-top-quark production (these are shown in Fig. 4.1). The cross section for s-channel production is known to $\pm 6\%$ [38], but only produces 25% of the events at the Fermilab Tevatron, and less than 4% at the CERN Large Hadron Collider (LHC). The cross section for Wt production accounts for less than 4% of the events at the Tevatron, and 20% at the LHC. Most single-top-quark events at both machines will come from W-gluon fusion. The LHC will measure the cross section to a few percent. Thus a full next-to-leading-order (NLO) result with errors on the order of $\pm 5\%$ is presented in Chapter 3.

In addition to the experimental need for an accurate single-top-quark cross section, W-gluon fusion provides a wealth of theoretical challenges that we address in Chapter 3. In the calculation itself, large logarithms of order $\ln(m_t^2/m_b^2)$ appear at every order in perturbation theory. The resolution of this problem requires an investigation of factorization and parton distribution functions. This leads to a reordering of perturbation theory, and two independent types of corrections to the leading-order result of order α_s and $1/\ln(m_t^2/m_b^2)$.

Factorizing the W-gluon fusion cross section introduces two factorization scales into the problem. At NLO, color conservation forbids strong interactions between the incom-

ing gluon line and the light-quark that emits the W. Thus the problem reduces to one of double deep-inelastic scattering (double DIS). Large logarithms are resummed in the factorization process, and set the factorization scale μ in DIS for each incoming parton. This scale is $\mu^2 = Q^2 + m_q^2$, where Q^2 is the virtuality of the W, and m_q is the mass of the final state quark. Hence, for a light quark final state, the scale is the usual DIS scale $\mu^2 = Q^2$. However, for a top-quark final state, the natural scale is $\mu^2 = Q^2 + m_t^2$.

Measurement of the single-top-quark cross sections requires accurate analyses of the experimental acceptances and backgrounds to each process. The rate to produce one top quark is roughly half of the $t\bar{t}$ production rate. Since both processes give a reconstructed top-quark mass, we must cut out $t\bar{t}$ events that mimic single top-quark production. In Ref. [5] an analysis was presented that estimated how well the W-gluon fusion cross section can be extracted from data at Run II of the Fermilab Tevatron. In Chapter 4 we improve on this analysis by scaling the signal to the full NLO cross section calculated in Chapter 3, and extending the analysis to the LHC. The large logarithms $\ln(m_t^2/m_b^2)$ mentioned above also affect this calculation. Thus we discuss the correct way to integrate over the problem region, and incorporate the NLO result. We discuss the tenability for discovering single-top-quark production at Run I of the Tevatron. We also determine how accurately the CKM matrix element V_{tb} can be directly measured at Run II, and the LHC.

Due to the $V - A$ nature of the electroweak force, the top quark in single-top-quark production is produced with a 100% polarization in the direction of the d-type quark in the event [39]. Since the top quark decays before if hadronizes [40], this polarization information is transferred to the top-quark decay products [41]. If there is any new physics that produces an effective $V + A$ interaction at the Wtb vertex, the polarization in this basis will

be reduced proportional to the strength of the new interaction. Hence, a measurement of the distribution of these particles could be a window into new physics. We suggest a method for extracting this polarization from the data, and estimate how well it can be measured.

Chapter 2

Supersymmetric QCD correction to top-quark production at the Fermilab Tevatron

The discovery of the top quark [2] provides a unique opportunity to search for effects beyond the standard model. The top quark mass $m_t = 174.1 \pm 5.4$ GeV has been measured to 3%, and the cross section has been measured to $\approx 25\%$ [4,6]. With the copious production of top quarks in Run II of the Fermilab Tevatron and future upgrades, the cross section will be measured to within 6% with 10 fb^{-1} of data [5]. Comparison of the theoretical $t\bar{t}$ cross section to that measured will test the standard model and may indicate the presence of new physics.

Supersymmetry is a promising candidate for new physics. Currently, only lower bounds on the masses of the superpartners have been set (see Sec. 1.1.1). Barring discovery, direct searches for supersymmetry (SUSY) will eliminate a small range of parameter space, since these searches depend strongly on the modeling of the decays of the supersymmetric parti-cles [14]. In contrast, some effects of virtual supersymmetry are less model dependent, thus extending the reach of experiment. If virtual SUSY effects are found to be large enough, an indirect search may provide the first sign of supersymmetry. In this chapter we present the

supersymmetric QCD correction to $t\bar{t}$ production at the Fermilab Tevatron.

The next-to-leading-order (NLO) QCD cross section for $t\bar{t}$ production with resummed gluon emission at a $\sqrt{S} = 2\,\text{TeV}$ $p\bar{p}$ collider has been calculated [42]. The dominant mechanism of top-quark production at the Tevatron is $q\bar{q}$ annihilation. It is expected that the dominant SUSY contribution to top-quark production will be in the form of QCD corrections to this process. We consider the SUSY correction to the cross section as a correction to the dominant process as shown in Fig. 2.2.

The calculation of the supersymmetric correction to top-quark production is different from typical SUSY calculations in that the number of assumptions about supersymmetry necessary to predict phenomenologically interesting results is minimal. It is assumed that R-parity is conserved so that the interaction terms in the Lagrangian are the simple supersymmetrization of the standard model interactions. No assumptions about the mechanism of SUSY breaking or of unification are required. In a strong-interaction process, the correction depends only on the observed masses of the gluino and squarks, and the mixing angle that relates the squark mass eigenstates to their interaction eigenstates. For the purpose of this calculation, and in order to cover the greatest range of models, we treat top squarks $\widetilde{t}$ separately from the light-quark superpartners $\widetilde{q}$. We present analytic and numerical results for degenerate squark masses, and for the case where the top squarks are light compared to the light-quark superpartners, the "heavy squarks". Results for $m_{\widetilde{t}}, m_{\widetilde{q}} > 50$ GeV, $m_{\widetilde{g}} > 150$ GeV, and arbitrary left-right mixing of the squarks are presented.

The SUSY QCD correction to top-quark production in e^+e^- annihilation was first studied in Ref. [43]. The correction in $p\bar{p}$ annihilation has been presented in Refs. [44–46] for the case of degenerate squark masses. The calculations of Refs. [44,45] neglect the contri-

bution of the vacuum polarization and the crossed-box diagram, which arises because the gluino is a Majorana particle. In addition, Ref. [45] assumes that the box contribution may be ignored. We find that these contributions are numerically significant, as demonstrated in Sec. 2.2.1. Our results are numerically comparable to Ref. [46], however there is an important sign discrepancy between the two box terms that we discuss in Sec. 2.1. There also appears to be a misprint in the analytic results of that paper that we describe at the end of Appendix A. We provide a complete calculation of the SUSY correction to the cross section for arbitrary masses and top-squark mixing, and discuss the phenomenological significance of the result. In addition, we discuss the tenability of finding SUSY thresholds in $t\bar{t}$ invariant mass distributions. Finally we address the issue of parity violation in a supersymmetric strong force.

This chapter is organized as follows. In Sec. 2.1, we present the analytic form of the $O(\alpha_s)$ SUSY QCD correction to the $p\bar{p} \to t\bar{t}$ cross section. In Sec. 2.2.1, we remark on the relative size of the terms in the correction. We present numerical results for the correction to the $p\bar{p} \to t\bar{t}$ cross section in Sec. 2.2.2. In Sec. 2.2.3, we show $t\bar{t}$ invariant mass distributions for several choices of gluino mass. We discuss the size of the strong force parity-violating left-right asymmetry in Sec. 2.2.4. Conclusions are presented in Sec. 2.3. We present analytic expressions for the vacuum, vertex and box terms in Appendix A, and Fortran code used in the numerical evaluations in Appendix B.

2.1 Analytic Supersymmetric QCD Correction

Supersymmetry replaces the fields in the QCD Lagrangian with sets of superfields. In softly broken supersymmetry, this leads to additional interactions between the particles and

their superpartners. These new interactions provide virtual corrections to the top-quark production cross section.

The supersymmetric Feynman rules used in the calculation are derived from the Lagrangian [12],

$$
\begin{aligned}
\mathcal{L} =\ & -i g_s A_\mu^A \widetilde{q}_a^* (T^A)_{ab} \overleftrightarrow{\partial^\mu} \widetilde{q}_b \\
& + i \frac{1}{2} g_s f^{ABC} \overline{\widetilde{g}}^A \gamma^\mu \widetilde{g}^B A_\mu^C \\
& + g_s^2 (T^A T^B)_{ab} A_\mu^A A^{\mu B} \left[\widetilde{q}_{La}^* \widetilde{q}_{Lb} + \widetilde{q}_{Ra}^* \widetilde{q}_{Rb} \right] \\
& - \sqrt{2} g_s (T^A)_{ab} \left[\overline{q}_a P_R \widetilde{g}^A \widetilde{q}_{Lb} - \overline{q}_a P_L \widetilde{g}^A \widetilde{q}_{Rb} + \overline{\widetilde{g}}^A P_L q_b \widetilde{q}_{La}^* - \overline{\widetilde{g}}^A P_R q_b \widetilde{q}_{Ra}^* \right] \,, \quad (2.1)
\end{aligned}
$$

where $P_L = (1 - \gamma_5)/2$, $P_R = (1 + \gamma_5)/2$, g_s is the strong coupling constant, T^A are $SU(3)$ color generators, a, b, c are colors, and A_μ is the field for the gluon g. Figure 2.1 lists the Feynman rules for the particle-sparticle interaction vertices. The direction of particle flow is indicated via arrows for the fermions. In all cases, the momentum is assumed to be in the direction of the arrows as well. The rules are shown for the physically-relevant mass eigenstates of the squarks rather than the interaction eigenstates. Mixing of the squarks is therefore explicit and parameterized by mixing angles $\theta_{\widetilde{t}}$ and $\theta_{\widetilde{q}}$ for the top squarks and light-quark superpartners, respectively:

$$
\begin{aligned}
\begin{pmatrix} \widetilde{t}_1 \\ \widetilde{t}_2 \end{pmatrix} &= \begin{pmatrix} \cos\theta_{\widetilde{t}} & \sin\theta_{\widetilde{t}} \\ -\sin\theta_{\widetilde{t}} & \cos\theta_{\widetilde{t}} \end{pmatrix} \begin{pmatrix} \widetilde{t}_L \\ \widetilde{t}_R \end{pmatrix} \\
\begin{pmatrix} \widetilde{q}_1 \\ \widetilde{q}_2 \end{pmatrix} &= \begin{pmatrix} \cos\theta_{\widetilde{q}} & \sin\theta_{\widetilde{q}} \\ -\sin\theta_{\widetilde{q}} & \cos\theta_{\widetilde{q}} \end{pmatrix} \begin{pmatrix} \widetilde{q}_L \\ \widetilde{q}_R \end{pmatrix} \,.
\end{aligned} \qquad (2.2)
$$

The one-loop supersymmetric QCD contribution to the $q\bar{q} \to t\bar{t}$ cross section at leading order in α_s is attributed to the cross term in the matrix element between the tree-level diagram and the one-loop diagrams presented in Fig. 2.2. The general form of the vertex

20

$$-ig_s(p+k)^{\mu}(T^A)_{ab}$$

$$-g_s f^{ABC}\gamma^{\mu}$$

$$2ig_s^2(T^AT^B)_{ab}g^{\mu\nu}$$

$\widetilde{q}_1 : ig_s\sqrt{2}(T^A)_{ab}\left[-\cos\theta_{\widetilde{q}}P_R + \sin\theta_{\widetilde{q}}P_L\right]$

$\widetilde{q}_2 : ig_s\sqrt{2}(T^A)_{ab}\left[\quad\sin\theta_{\widetilde{q}}P_R + \cos\theta_{\widetilde{q}}P_L\right]$

$\widetilde{q}_1 : ig_s\sqrt{2}(T^A)_{ab}\left[-\cos\theta_{\widetilde{q}}P_L + \sin\theta_{\widetilde{q}}P_R\right]$

$\widetilde{q}_2 : ig_s\sqrt{2}(T^A)_{ab}\left[\quad\sin\theta_{\widetilde{q}}P_L + \cos\theta_{\widetilde{q}}P_R\right]$
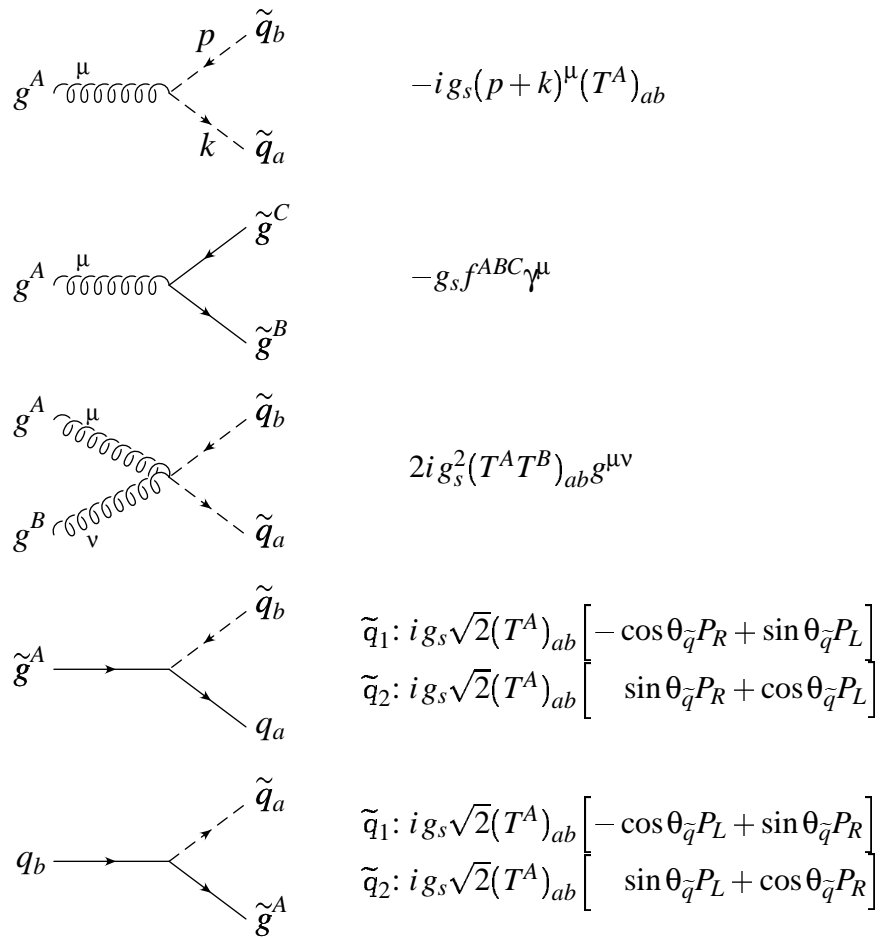
Figure 2.1: Supersymmetric QCD Feynman rules.
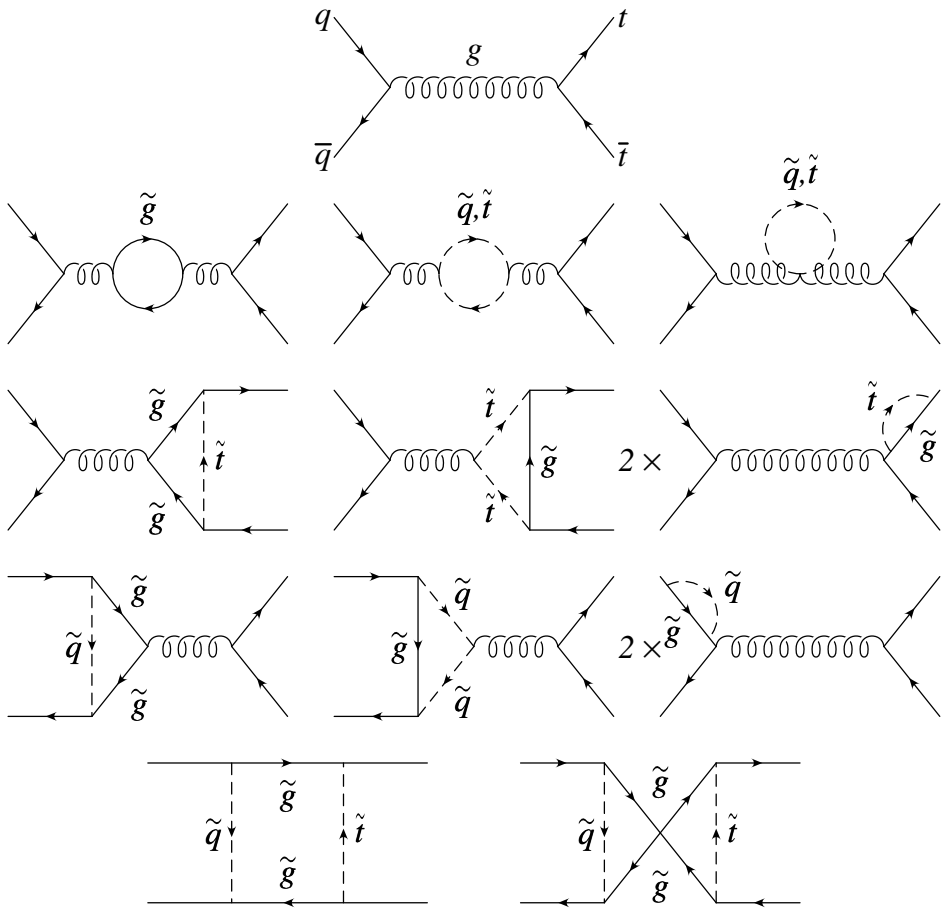
Figure 2.2: Feynman diagrams for the one-loop SUSY QCD correction to top quark production at the Tevatron. The first row contains the tree-level diagram. The second row contains the vacuum polarization correction to the gluon propagator due to squarks and gluinos. The third row contains the final state vertex correction and wave-function renormalization diagrams. The fourth row contains the initial state vertex correction and wave-function renormalization diagrams. The last row contains the box and crossed-box diagrams.

corrections, consistent with current conservation, is

$$
\begin{aligned}
i\bar{u}(p_1)\Gamma^{\mu,A}v(p_2) = &-ig_s\left[\bar{u}(p_1)T^A\gamma^\mu v(p_2)\right.\\
&\left.-\frac{\alpha_s}{4\pi}\,\bar{u}(p_1)T^A\left[V\gamma^\mu + S(p_1^\mu - p_2^\mu)/m_q + A(\gamma^\mu q^2 - 2m_q q^\mu)\gamma_5\right]v(p_2)\right],
\end{aligned}
\tag{2.3}
$$

where p_1 and p_2 are the momenta of the quark and antiquark, $q = p_1 + p_2$, and V, S, and A are the vector, scalar, and anapole form factors, respectively. The analytic forms of V, S, A, the gluon vacuum polarization Π, and the corrections due to the box and crossed-box diagrams, B and C, are given in Appendix A. The anapole term A does not contribute to the total cross section at this order in the expansion. It is used in Sec. 2.2.4, however, in determining the parity-violating left-right asymmetry due to the squark mixing. The Dirac algebra and loop integrals were evaluated using dimensional regularization. The analytic cross section was derived in the modified minimal subtraction ($\overline{\text{MS}}$) renormalization scheme.

The spin- and color-averaged parton-level differential cross section is given by

$$
\frac{d\hat{\sigma}}{dz} = \frac{\beta}{32\pi\hat{s}}|M|^2 ,
\tag{2.4}
$$

where z is the cosine of the angle between the incoming quark and the top quark, $\sqrt{\hat{s}}$ is the parton center-of-momentum energy, and $\beta = \sqrt{1 - 4m_t^2/\hat{s}}$. The Born matrix element squared is given by

$$
|M_0|^2 = \frac{32\pi^2\alpha_s{}^2}{9}[2 - \beta^2(1 - z^2)] .
\tag{2.5}
$$

Integrating over $-1 \leq z \leq 1$ readily yields the Born-level cross section

$$
\hat{\sigma}_0 = \frac{4\pi\alpha_s^2\beta}{9\hat{s}}(1 - \beta^2/3) .
\tag{2.6}
$$

The correction arises from the cross term in the square of the amplitude. This correction

23

is the sum of the terms:

$$2\text{Re}[M_0^\dagger M_\Pi] = -\frac{\alpha_s}{2\pi}|M_0|^2\text{Re}[\Pi(\hat{s}) - \Pi(0)] , \qquad (2.7)$$

$$2\text{Re}[M_0^\dagger M_V] = -\frac{\alpha_s}{2\pi}|M_0|^2\text{Re}[V] ,$$

$$2\text{Re}[M_0^\dagger M_S] = \frac{32\pi\beta^2\alpha_s^3}{9}(1-z^2)\text{Re}[S] ,$$

$$2\text{Re}[M_0^\dagger M_{BOX}] = \frac{32\pi\alpha_s^3}{9\hat{s}}\text{Re}\left[\frac{7}{3}B + \frac{2}{3}C\right] .$$

We renormalize the vacuum polarization correction $\Pi(\hat{s})$ so that it corresponds to the known value of α_s in the $\overline{\text{MS}}$ scheme at low energy. This is necessary, because perturbation theory is invalid at low $\hat{s}$. Therefore, we explicitly employ a dispersion relation to integrate out the non-perturbative regime from the calculation [47].

The integration over phase space is trivial except for the box and crossed-box matrix elements, B and C, which depend implicitly on z. The relative sign between the box and crossed-box terms should be noted. The color factor associated with C is $-2/3$. However, Fermi statistics provides a non-trivial relative sign difference between the two diagrams. The net result is that the two contributions constructively interfere. Eq. 2.7 reflects this explicitly as $\frac{7}{3}B + \frac{2}{3}C$. This disagrees with the calculation of Ref. [46], which claims that the terms destructively interfere.

We should look carefully at the value of the sign between the box diagrams. When writing down the matrix element, the usual rule is to oppose the direction of fermion flow when ordering the spinors. The implementation is obvious for Dirac spinors, but the gluinos are Majorana particles. As may be seen in Fig. 2.3, the direction of particle flow is not clear in the crossed-box diagram. This leaves a sign ambiguity between the box and crossed-box diagrams. In order to determine the relative sign between the box and crossed-box diagrams,

24
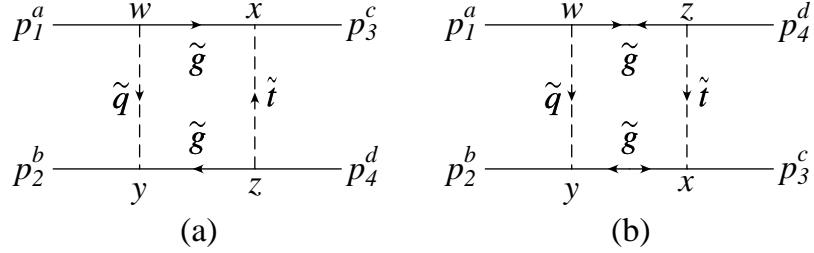
Figure 2.3: The vertices are labeled with *w–z*, and the color indices *a–d* are associated with each particle's momentum for the box diagram (a), and the crossed-box diagram (b).

we must derive the matrix elements, M_B and M_C, from a field theoretic point of view.

The matrix elements for the box terms are constructed by placing copies of the quark-squark-gluino interaction terms from the Lagrangian between the initial and final states, $< p_4, p_3|$ and $|p_1, p_2 >$. We first evaluate the color terms for both diagrams.

Before writing down the color factors for the box diagrams, we will need

$$
\begin{aligned}
\text{Tr}(T^A T^B T^C) &= \frac{1}{2}\text{Tr}\left(\{T^A, T^B\}T^C + [T^A, T^B]T^C\right) \\
&= \frac{1}{4}(d^{ABC} + i f^{ABC}).
\end{aligned}
\tag{2.8}
$$

The color factor from the tree-level diagram is $(T^C)_{ab}(T^C)_{dc}$, where *a–d* correspond to the color indices for the momenta in Fig. 2.3.

The color factor for the box diagram is $(T^A T^B)_{cd}(T^B T^A)_{ba}$. Therefore the total color factor for *B* is

$$
\begin{aligned}
\text{Tr}(T^A T^B T^C)\text{Tr}(T^C T^B T^A) &= \frac{1}{16}(d^{ABC}d^{ABC} + f^{ABC}f^{ABC}) \\
&= 5/6 + 3/2 = 7/3.
\end{aligned}
\tag{2.9}
$$

The color factor for the crossed-box diagram is $(T^A T^B)_{cd}(T^A T^B)_{ba}$. Therefore the total

25

color factor for C is

$$\text{Tr}(T^A T^B T^C)\text{Tr}(T^A T^B T^C) = \frac{1}{16}(d^{ABC} + f^{ABC})^2$$

$$= 5/6 - 3/2 = -2/3. \tag{2.10}$$

The portion of the matrix element that depends on the fields is

$$< p_4, p_3| \left[\bar{t}_i (P_R \tilde{t}_L - P_L \tilde{t}_R)_{ij} \tilde{g}^A_j \right]_x \left[\bar{\tilde{g}}^A_k (P_L \tilde{t}_L - P_R \tilde{t}_R)_{kl} t_l \right]_z \times$$

$$\left[\bar{q}_m (P_R \tilde{q}_L - P_L \tilde{q}_R)_{mn} \tilde{g}^A_n \right]_y \left[\bar{\tilde{g}}^A_o (P_L \tilde{q}_L - P_R \tilde{q}_R)_{op} q_p \right]_w |p_1, p_2 > , \tag{2.11}$$

where we use the labels w, x, y, and z to denote the corresponding vertex (see Fig. 2.3). The labels i–p keep track of the components of the non-commuting matrices.

In order to obtain the Dirac spinors and propagators, we contract the fields in the order indicated by the lines below (from inside to out). The terms involving projection operators are abbreviated by the first piece. For the box diagram,

$$< p_4, p_3| \left[\bar{t}_i (P_R \tilde{t}_L)_{ij} \tilde{g}_j \right]_x \left[\bar{\tilde{g}}_k (P_L \tilde{t}_L)_{kl} t_l \right]_z \left[\bar{q}_m (P_R \tilde{q}_L)_{mn} \tilde{g}_n \right]_y \left[\bar{\tilde{g}}_o (P_L \tilde{q}_L)_{op} q_p \right]_w |p_1, p_2 > . \tag{2.12}$$

If we denote the momentum of the gluino by p, we find for the contraction of two Majorana fermions,

$$g_a \bar{\tilde{g}}_b = (\not{p} + m_{\tilde{g}})_{ab}, \tag{2.13}$$

$$g_a g_b = -(\not{p} + m_{\tilde{g}})_{ab} C,$$

$$\bar{\bar{\tilde{g}}}_a \bar{\tilde{g}}_b = C^{-1}(\not{p} + m_{\tilde{g}})_{ab},$$

where C is the charge conjugation matrix satisfying [12]

$$C^\dagger = C^{-1}, \tag{2.14}$$

$$C^{\mathrm{T}} = -C,$$

$$C^{-1}\Gamma_i C = \Gamma_i^{\mathrm{T}}, \text{ for } \Gamma_i = 1, i\gamma_5, \gamma_\mu\gamma_5,$$

$$C^{-1}\Gamma_i C = -\Gamma_i^{\mathrm{T}}, \text{ for } \Gamma_i = \gamma_\mu, \sigma_{\mu\nu} = \frac{1}{2}i[\gamma_\mu, \gamma_\nu].$$

The field component of the box matrix element is

$$M_B \sim -1 \times \bar{u}_3(P_R\tilde{t}_L)(\not{p} + m_{\tilde{g}})_{xw}(P_L\tilde{q}_L)u_1\bar{v}_2(P_R\tilde{q}_L)(\not{p} + m_{\tilde{g}})_{yz}(P_L\tilde{t}_L)v_4. \qquad (2.15)$$

For the crossed-box diagram,

$$< p_4, p_3 | \left[\bar{t}_i(P_R\tilde{t}_L)_{ij}\tilde{g}_j\right]_x \left[\bar{\tilde{g}}_k(P_L\tilde{t}_L)_{kl}t_l\right]_z \left[\bar{q}_m(P_R\tilde{q}_L)_{mn}\tilde{g}_n\right]_y \left[\bar{\tilde{g}}_o(P_L\tilde{q}_L)_{op}q_p\right]_w | p_1, p_2 > .$$

$$(2.16)$$

We must choose which order to write down $\bar{\tilde{g}}_k\bar{\tilde{g}}_o$. In order for the matrix multiplication to line up in the matrix element, we must choose $\bar{\tilde{g}}_o\bar{\tilde{g}}_k$ which gives an overall $+1$ sign from ordering the fields. The field component of the crossed-box matrix element is

$$M_C \sim +1 \times \bar{u}_3(P_R\tilde{t}_L)(-\not{p} - m_{\tilde{g}})_{xy}C(P_R\tilde{q}_L)^{\mathrm{T}}\bar{v}_2^{\mathrm{T}}u_1^{\mathrm{T}}(P_L\tilde{q}_L)^{\mathrm{T}}C^{-1}(\not{p} + m_{\tilde{g}})_{wz}(P_L\tilde{t}_L)v_4. \quad (2.17)$$

Combining the color and Fermi statistics results, we see that the overall sign between the matrix elements is the same. If we multiply both matrix elements by the propagators for the scalar particles, and use the correct momenta for the gluinos, we may reproduce the full matrix elements. After crossing in the fields from the tree-level matrix element, we reproduce the corrections B and C in Appendix A.[1]

We are now in a position to calculate the total cross section. The total cross section for top-quark production in $p\bar{p}$ annihilation is obtained by convolving the parton cross section

---

[1] Since the publication of these results, a paper has appeared that confirms the signs derived here [48].

for annihilation into a $t\bar{t}$ final state with the parton distribution functions of the proton and antiproton. The integral may be parameterized as

$$\sigma = \int_{4m_t^2/S}^{1} d\tau \,\hat{\sigma}(\tau S) \int_{\ln(\tau)/2}^{-\ln(\tau)/2} d\eta \, P(\sqrt{\tau}e^{\eta}, \sqrt{\hat{s}}) \, \overline{P}(\sqrt{\tau}e^{\eta}, \sqrt{\hat{s}}) \,, \qquad (2.18)$$

where $\sqrt{S} = 2$ TeV, $\tau = \hat{s}/S$ and $P(x_1, \mu), \overline{P}(x_2, \mu)$ are the proton and antiproton parton distribution functions (PDF's).

In the following section, numerical results are presented for a top quark of mass $m_t = 175$ GeV. Analytic expressions were reduced to scalar n-point integrals [49] and evaluated with the aid of the code FF [50] in order to ensure numerical stability. For those cases that FF does not handle, the analytic solutions to the integrals were substituted. The Fortran code that performs these reductions is in Appendix B. The integrals were evaluated using both the MRS(A$'$) [51] and CTEQ3M [52] PDF's. The running of α_s was evaluated using two-loop renormalization group equations [53] and fixed in the PDF's in order to be consistent. Nearly identical results were obtained using both sets, therefore, only the results obtained using the MRS(A$'$) PDF's are presented.

2.2 Numerical results

2.2.1 Relative size of the correction terms

In Fig. 2.4 we show the correction to the total cross section as a function of common squark mass $m_{\tilde{Q}} \equiv m_{\tilde{q}} = m_{\tilde{t}}$, for $m_{\tilde{g}} = 200$ GeV. The contribution of the vacuum, vector, scalar, and box terms are shown separately. The full correction is also shown for comparison. The box diagrams give the largest contribution to the cross section for $m_{\tilde{Q}} < 110$ GeV, and are significant for $m_{\tilde{Q}} < 400$ GeV. This invalidates the assumption of Ref. [45] that the

28
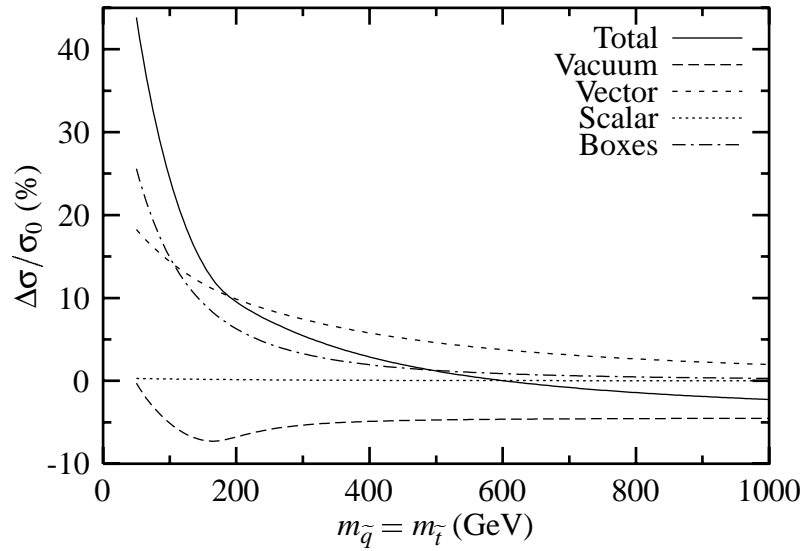
Figure 2.4: Contribution of each term to the correction for $p\bar{p} \to t\bar{t}$ as a function of $m_{\tilde{q}} = m_{\tilde{t}}$, for $m_{\tilde{g}} = 200$ GeV.
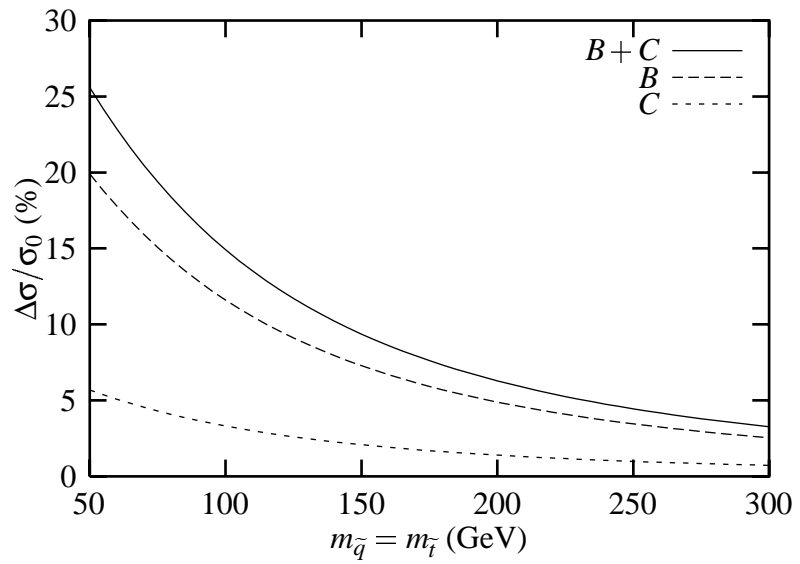
Figure 2.5: The contribution of the box B and crossed-box C terms to the correction for $p\bar{p} \to t\bar{t}$ as a function of $m_{\tilde{q}} = m_{\tilde{t}}$, for $m_{\tilde{g}} = 200$ GeV. The sum of the corrections is shown for comparison with Fig. 2.4.

box terms may be neglected over the range of masses they investigated. Similarly it contradicts the conclusion of Ref. [46] that the contribution of the box terms is small. The vacuum correction, that was ignored in Refs. [44,45], also plays an important role. The gluino loops in the vacuum polarization give a constant negative correction when the squarks decouple. When $m_{\widetilde{Q}} = 1$ TeV, the correction is seen to come almost entirely from the vacuum polarization. The contribution of the scalar term S is negligible. It first appears at this order in the final state correction, and is suppressed relative to the other terms by a power of the top-quark mass. The decoupling of the vector, scalar, and box terms is evident in Fig. 2.4, as the corrections decrease when the squark mass increases.

The correction due to the box B and crossed-box C terms is shown separately in Fig. 2.5. The constructive interference between B and C is clearly non-negligible. At $m_{\widetilde{Q}} = 100$ GeV, Ref. [46] underestimates of the contribution of the box terms to the cross section by $1/2$, by assuming destructive interference. This explains the mis-statement that the box terms are not important. The total correction in that paper is thus too small by $1/4$ (a 17.8% correction to $t\bar{t}$ production instead of 24.4%).

2.2.2 $t\bar{t}$ cross section

The correction to the $p\bar{p} \rightarrow t\bar{t}$ cross section is shown in Fig. 2.6 as a function of the gluino mass for a wide range of degenerate squark masses $m_{\widetilde{Q}}$, where $m_{\widetilde{Q}} \equiv m_{\widetilde{q}} = m_{\widetilde{t}}$. As expected from decoupling, the magnitude of the correction decreases as the squark mass increases. Squarks of mass 50 GeV set the range of the correction from -11.8% for a gluino of 150 GeV to $+44\%$ for a gluino of 200 GeV. The correction changes sign as $m_{\widetilde{g}}$ approaches m_t. The correction changes rapidly as the threshold for gluino production moves through the
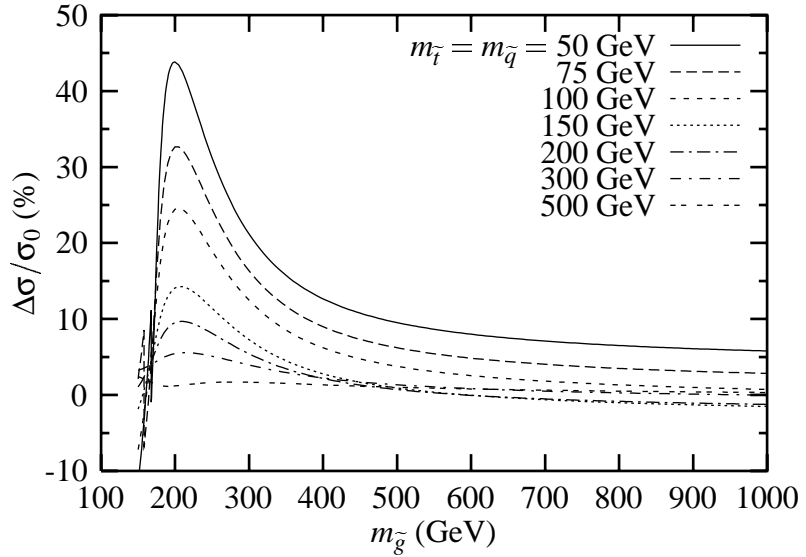
Figure 2.6: Change in the cross section for $p\bar{p} \rightarrow t\bar{t}$, as a function of gluino mass $m_{\tilde{g}}$, for $m_t = 175$ GeV. Curves of constant degenerate squark mass $m_{\tilde{q}} = m_{\tilde{t}}$ are shown.

top-quark threshold. Note that the correction is very slowly dependent on gluino mass when $m_{\tilde{g}} > 500$ GeV. In this region, the correction is entirely dominated by the squark vacuum terms and, to a lesser extent, the box terms.

In Fig. 2.8 we show the correction to the total cross section as a function of degenerate squark mass $m_{\tilde{Q}} \equiv m_{\tilde{q}} = m_{\tilde{t}}$, for several gluino masses. Once $m_{\tilde{Q}} > 400$ GeV, the correction becomes small and the squarks effectively decouple. In this region, the correction is dominated by the gluino vacuum terms. In Figs. 2.7 and 2.8 there is a large jump in the cross section when $m_t^2 = m_{\tilde{t}}^2 + m_{\tilde{g}}^2$. In Fig. 2.7, the correction is discontinuous at $m_{\tilde{g}} = 168$ GeV when $m_{\tilde{Q}} = 50$ GeV, and at $m_{\tilde{g}} = 158$ GeV when $m_{\tilde{Q}} = 75$ GeV. In Fig. 2.8, the correction jumps from $+6.5\%$ to -9.3% for $m_{\tilde{g}} = 150$ GeV, $m_{\tilde{t}} = 90.1$ GeV. These jumps correspond to a discontinuity in the real part of the C_0 scalar loop-integral in the final-state vertex correction [54]. Such a discontinuity arises when the anomalous threshold crosses the real

31
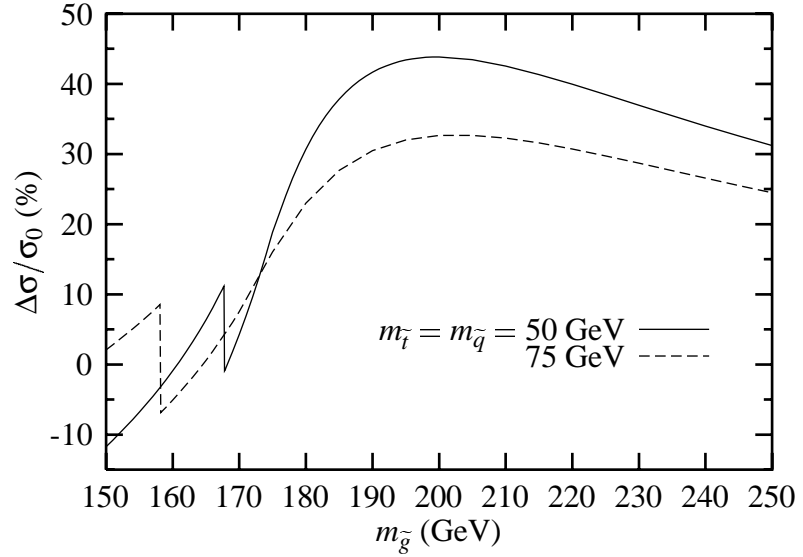
Figure 2.7: Enlargement of the discontinuous region of Fig. 2.6. The change in the cross section for $p\bar{p} \to t\bar{t}$, as a function of gluino mass $m_{\tilde{g}}$, for $m_t = 175$ GeV. Curves of constant degenerate squark mass $m_{\tilde{q}} = m_{\tilde{t}}$ are shown.
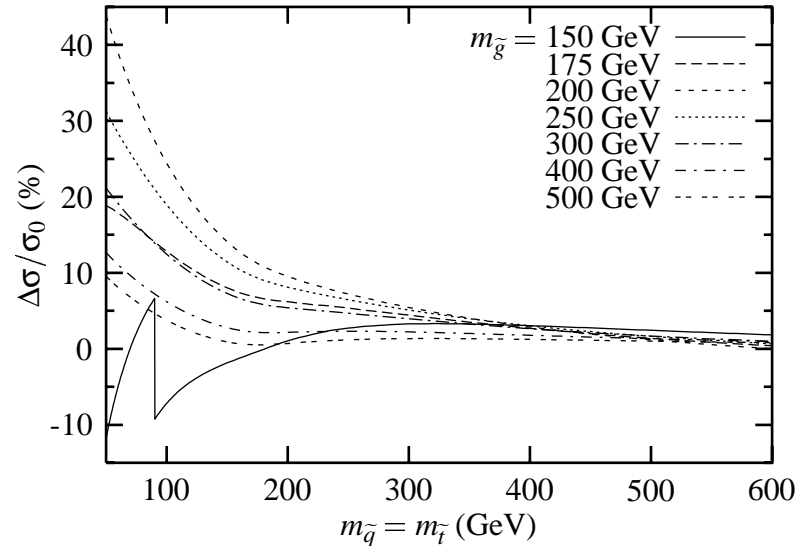
Figure 2.8: Change in the cross section for $p\bar{p} \to t\bar{t}$, as a function of degenerate squark mass $m_{\tilde{q}} = m_{\tilde{t}}$, for $m_t = 175$ GeV. Curves of constant gluino mass $m_{\tilde{g}}$ are shown.
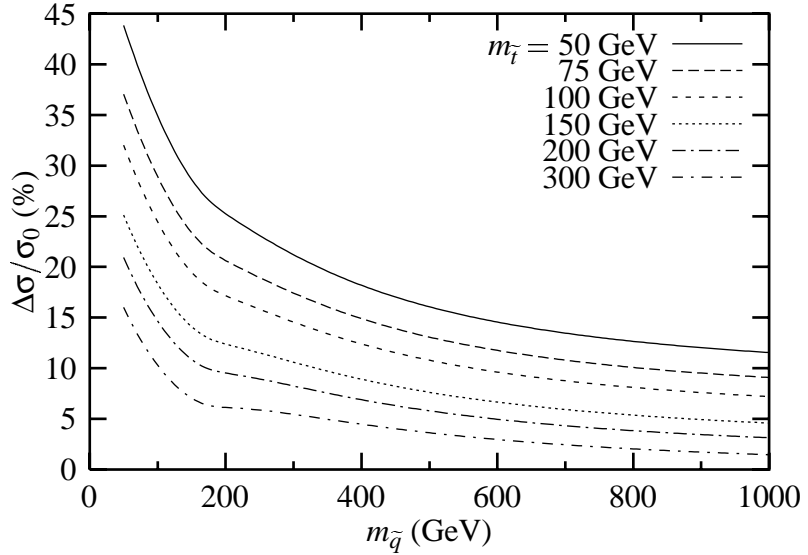
Figure 2.9: Change in the cross section for $p\bar{p} \to t\bar{t}$, as a function of heavy-squark mass $m_{\tilde{q}}$, for $m_t = 175$ GeV, and $m_{\tilde{g}} = 200$ GeV. Curves of constant top-squark mass $m_{\tilde{t}}$ are shown.

threshold for superpartner production in the complex $\hat{s}$-plane [55].

The largest correction occurs when $m_{\tilde{g}} = 200$ GeV. This mass is used in Fig. 2.9 to show the correction as a function of heavy-squark mass $m_{\tilde{q}}$, for a variety of top-squark masses. This figure demonstrates that the correction is mostly influenced by the mass of the top squark. For example, the correction is 21% for $m_{\tilde{t}} = 50$ GeV, and $m_{\tilde{q}} = 300$ GeV; whereas the correction is 16% for $m_{\tilde{t}} = 300$ GeV, and $m_{\tilde{q}} = 50$ GeV. Even if the heavy squarks decouple, the correction remains significant as long as $m_{\tilde{t}} < 150$ GeV.

In general, the left and right eigenstates of the squarks receive different corrections to their masses. This causes the mass of $\widetilde{Q}_R$ to be less than the mass of $\widetilde{Q}_L$. Top-squark masses are more effected by renormalization group running than the heavy-squark masses, because of the direct coupling of the top quark to the top squarks. Many analyses assume that the
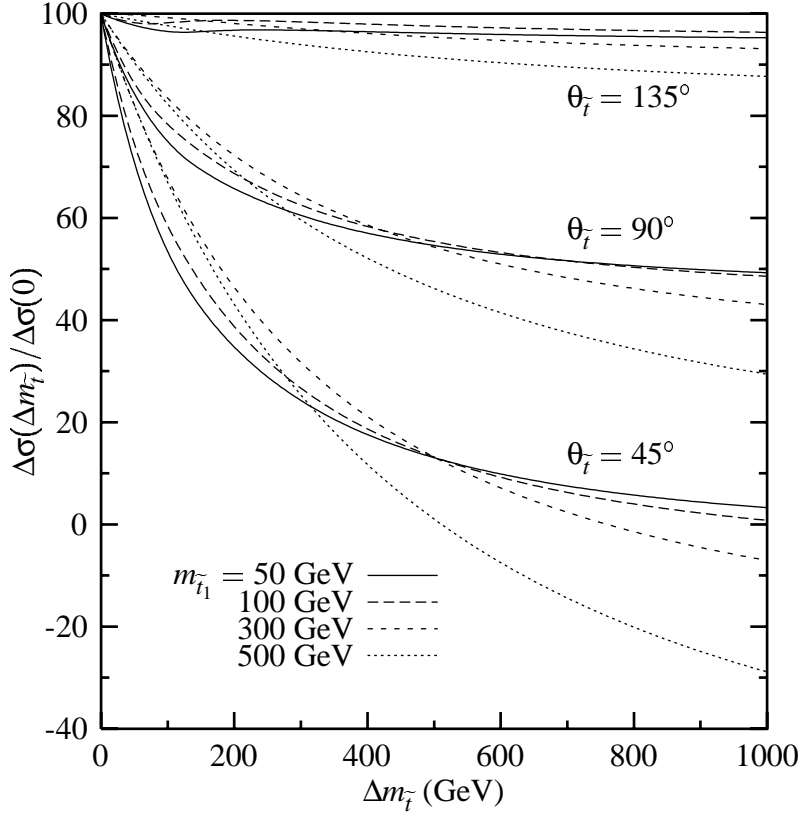
Figure 2.10: The relative change to the correction is shown as a function of top-squark mass difference $\Delta m_{\tilde{t}} = (m_{\tilde{t}_2} - m_{\tilde{t}_1})$, for various $m_{\tilde{t}_1}$, and mixing angles $\theta_{\tilde{t}}$, with $m_t = 175$ GeV, and $m_{\tilde{g}} = 200$ GeV.

only light squark is $\tilde{t}_1$, and look for top quarks decaying into them [22]. In Fig. 2.10 we show the ratio of the correction at $\Delta m_{\tilde{t}} = (m_{\tilde{t}_2} - m_{\tilde{t}_1})$ to the correction at a common top-squark mass $\Delta m_{\tilde{t}} = 0$, for $m_{\tilde{g}} = 200$ GeV and $m_{\tilde{q}} = 300$ GeV. The ratio does not change by more than 2% for different values of $m_{\tilde{q}}$. We present three mixing angles, $\theta_{\tilde{t}} = 45°$, $90°$, and $135°$ that define the extremes of the mixing dependence of the correction.

The form of the correction is $a + b\sin(2\theta_{\tilde{t}})$, thus the contribution of any mixing angle may be interpolated from the curves shown, where $\theta_{\tilde{t}} = 90°$ is the central value. Note that if $\theta_{\tilde{t}} = 135°$, then the correction is nearly independent of $m_{\tilde{t}_2}$. This is because the terms for

34

the left- and right-handed squarks enter with different signs in the Lagrangian (Eq. 2.1), and $\widetilde{t}_2 = (\widetilde{t}_L + \widetilde{t}_R)/\sqrt{2}$ (Eq. 2.3). Whereas if $\theta_{\widetilde{t}} = 90°$, where the mass eigenstates are the interaction eigenstates ($\widetilde{t}_1 = \widetilde{t}_R$, $\widetilde{t}_2 = \widetilde{t}_L$), the correction is roughly split between the two top squarks. To evaluate the correction for non-degenerate top-squark masses and top-squark mixing, multiply the ratio from Fig. 2.10 by the correction from Figs. 2.8 or 2.9. For example, the correction to top-quark production is $7.7 \pm 0.1\%$, when $m_{\widetilde{t}_1} = 100$ GeV, $m_{\widetilde{t}_2} = 400$ GeV, $m_{\widetilde{g}} = 200$ GeV, $m_{\widetilde{q}} = 400$ GeV, and $\theta_{\widetilde{t}} = 90°$.

2.2.3 $t\bar{t}$ invariant mass distributions

Since total cross section measurements are difficult to normalize, it is advantageous to look for deviations from the line-shapes predicted by the standard model. A sampling of the invariant mass of $t\bar{t}$ events provides another avenue to search for supersymmetry. In Fig. 2.11 we show the total differential cross section as a function of $t\bar{t}$ invariant mass $M_{t\bar{t}}$, for gluinos of mass $m_{\widetilde{g}} = 150$, 175, 200, and 225 GeV. Several choices of degenerate squark mass $m_{\widetilde{Q}} \equiv m_{\widetilde{q}} = m_{\widetilde{t}}$, are presented. By looking for an excess in the invariant mass distribution, a gluino of mass between 175 GeV and 225 GeV may be observable.

There are two types of enhancement to the cross section that appear in Fig. 2.11. If $m_{\widetilde{g}} \approx m_t$, the maximum of the invariant mass distribution is shifted toward the common threshold. This would also produce a steeper top-quark threshold region in the data. An integrable singularity at the threshold for gluino pair production causes a cusp at $2m_{\widetilde{g}}$. We can understand this singularity by looking at the gluino-loop contribution to the gluon vacuum polarization. If we cut the fermion loop (see Fig. 2.12), a dispersion relation relates the real part of the vacuum polarization $\Pi(s)$ to the imaginary part. This gives

35
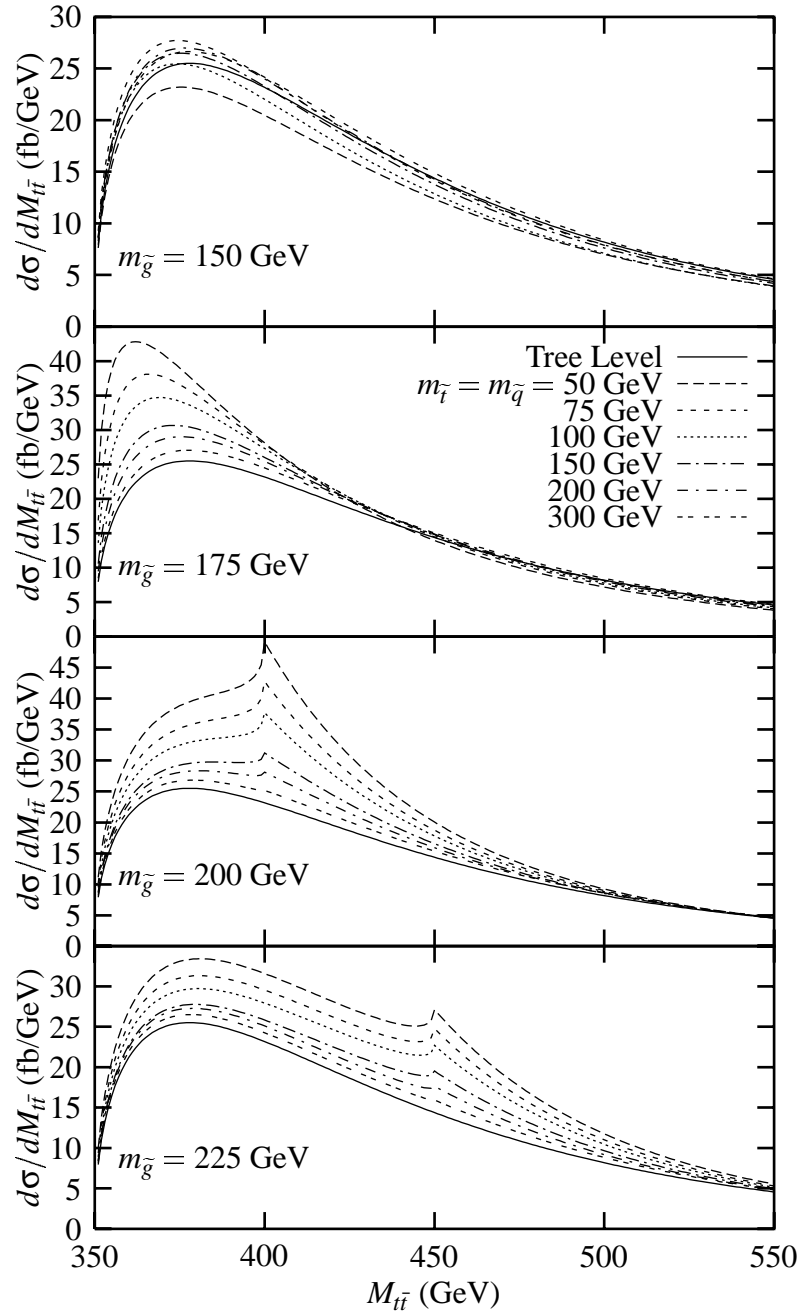
Figure 2.11: Differential cross section for $p\bar{p} \to t\bar{t}$, as a function of $t\bar{t}$ invariant mass $M_{t\bar{t}}$, for $m_t = 175$ GeV. Figures are shown for $m_{\tilde{g}} = 150, 175, 200,$ and 225 GeV. Curves of constant degenerate squark mass $m_{\tilde{q}} = m_{\tilde{t}}$ are shown.
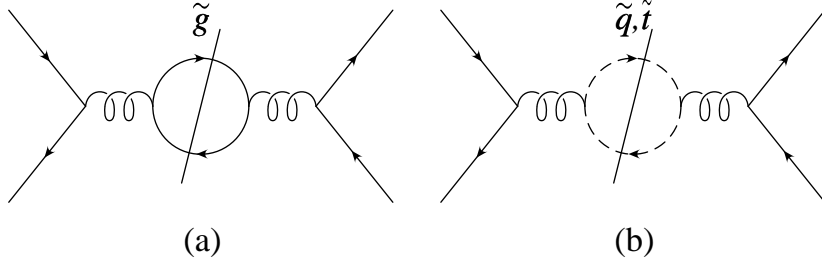
Figure 2.12: Cutting the (a) gluino loop, or (b) squark loop, in the vacuum polarization leads to a dispersion relation.

$$\mathrm{Re}\Pi(s) \sim \int_{4m^2}^{\infty} ds' \frac{\beta^{2\ell+1}}{s'-s} \,, \tag{2.19}$$

where $\beta = (1 - 4m^2/s')^{1/2}$. The s-channel gluon has spin $S = 1$. Hence, to produce two $S = 1/2$ gluinos, $L = 0$, and $m \equiv m_{\widetilde{g}}$. Conservation of momentum tells us that $s = M_{t\bar{t}}^2$. Therefore,

$$\mathrm{Re}\Pi(M_{t\bar{t}}^2) \sim \int_{4m_{\widetilde{g}}^2}^{\infty} ds' \frac{(1 - 4m_{\widetilde{g}}^2/s')^{1/2}}{s'-M_{t\bar{t}}^2} \,. \tag{2.20}$$

When $M_{t\bar{t}} = 2m_{\widetilde{g}}$, this looks like

$$\mathrm{Re}\Pi(M_{t\bar{t}}^2) \sim \int_{4m_{\widetilde{g}}^2}^{\infty} ds' \frac{1}{(s')^{1/2}(s' - 4m_{\widetilde{g}}^2)^{1/2}} \,, \tag{2.21}$$

which is integrable, but has a singularity at the lower limit of integration. Since the equation is integrable, the value as a function of $M_{t\bar{t}}$ is continuous. At threshold, however, this term picks up negative contributions from the pole at $s' = M_{t\bar{t}}^2$. The total vacuum polarization (and vertex corrections) will have a cusp at this point. The contribution due to the squarks does not exhibit a cusp; since the squarks have spin $S = 0, L = 1$, and the integrand is finite everywhere.

The largest cusp in Fig. 2.11 occurs when $m_{\widetilde{g}} = 200$ GeV, and $m_{\widetilde{Q}} = 50$ GeV. The am-

plitude of the cusp is 112% of the Standard Model differential cross section at this point. Despite the large normalization, the cusp will sit on a large continuum background. If we assume purely statistical errors, this cusp would appear at the 3σ level with 3 fb^{-1} of integrated luminosity. For $m_{\tilde{g}} \approx 200$ GeV, the correction is most apparent for $m_{\tilde{Q}} < 150$ GeV. If $m_{\tilde{g}} > 225$ GeV, then even with light squarks, the correction will be difficult to observe.

2.2.4   Strong force parity violation

In the standard model, the top quark decays before its spin flips [40]. The helicity of the top quark is reflected in the angular distribution of the decay products of the W boson in $t \rightarrow bW \rightarrow b\ell^+\nu$ and $t \rightarrow bW \rightarrow b\bar{d}u$ decays. (See Ref. [41] for a detailed account of the analyzing power of these decays.) The $gt\tilde{t}$ interaction term in the SUSY Lagrangian treats left- and right-handed top squarks differently. This leads to the interesting possibility of searching for parity violation in strong force interactions by analyzing the decay products in top-quark production.

An asymmetry in the number of left and right-handed top quarks arises in the production cross section when the top squarks have different masses. This asymmetry is given by

$$\Delta\hat{\sigma}_A = \hat{\sigma}_L - \hat{\sigma}_R = \frac{2\beta^2\alpha_s^3}{27\hat{s}}\text{Re}[A] \, , \tag{2.22}$$

where σ_L, σ_R are the cross sections for the left and right helicities of the top quark. The measured left-right asymmetry A_{LR} is the ratio of the integrated $\Delta\hat{\sigma}_A$ to the total measured cross section

$$A_{LR} = \frac{\Delta\sigma_A}{\sigma_{TOT}} = \frac{n_L - n_R}{n_L + n_R} \, , \tag{2.23}$$

where n_L, n_R are the number of left and right-handed top quarks respectively. Unfortunately,

38

we find that A_{LR} is always less than 1% for any choice of the SUSY parameters. There-fore, if supersymmetric parity violation in the strong force exists, it will be very difficult to measure.[2]

2.3 Conclusions

The supersymmetric QCD correction to the top-quark cross section, as measured at the Tevatron, has been calculated. We present analytic results for a minimal supersymmetric model that depends only on the masses of the superpartners and their mixing. We obtain numerical results for the total correction for all masses $m_{\tilde{g}} > 150$ GeV, $m_{\tilde{q}} > 50$ GeV and $m_{\tilde{t}} > 50$ GeV. The correction is found to be large for gluino masses near 200 GeV. The correction is greater than $+10\%$ for $m_{\tilde{g}} = 200$ GeV and $m_{\tilde{q}} = m_{\tilde{t}} < 190$ GeV. If light top squarks $m_{\tilde{t}} < 150$ GeV exist, then the correction should be observable with 10 fb^{-1} at the Tevatron for $m_{\tilde{g}} < 400$ GeV, even if the heavy squarks decouple. If all of the squarks remain light, then the correction is significant even if the gluinos decouple. When considering a mass splitting between the top squarks, the mixing angle $\theta_{\tilde{t}}$ plays an important role. If $\theta_{\tilde{t}}$ is near $45°$, or $135°$, then the correction is almost entirely dependent on the mass of only one of the top squarks.

Should the gluino mass turn out to be near the current experimental limits, a gluino-pair threshold may be found near the top-quark production threshold. The advantage of looking for a cusp in the $t\bar{t}$ invariant mass distribution, is that the normalization of the top-quark cross section is not necessarily a limiting factor. Detector resolution effects and smearings will make this search very challenging. It is reasonable to expect that at least 10 fb^{-1} of

[2]Since the publication of these results, a paper has appeared which confirms that the parity violation arising from the box diagrams is negligible compared with the vertex correction [48].

39

integrated luminosity would be required to find a cusp for the best case of $m_{\tilde{g}} \approx 200$ GeV, and $m_{\tilde{Q}} < 150$ GeV. Virtual SUSY thresholds are common in quark production [56]. A full detector-based analysis of these threshold regions would help determine the experimental significance of our results.

Parity violation in a purely strong force interaction arises in a supersymmetric standard model because the left- and right-handed top squarks interact differently. As long as the top-squark masses are different, an asymmetry in the number of left and right-handed top quarks will arise. Unfortunately, the effect is less than 1%, and will be very difficult to measure.

Chapter 3

Single-top-quark production via W-gluon fusion at next-to-leading order

Now that the existence of the top quark is firmly established [2], attention turns to testing its properties. A powerful probe of the charged-current weak interaction of the top quark at hadron colliders is single-top-quark production. The two primary processes are quark-antiquark annihilation via a virtual s-channel W boson [57, 58] and W-gluon fusion, which involves a virtual t-channel W boson (Fig. 3.1) [59–61]. Within the context of the standard model, these processes provide a direct measurement of the Cabibbo-Kobayashi-Maskawa (CKM) matrix element V_{tb}. Beyond the standard model, they are sensitive to new physics associated with the charged-current weak interaction of the top quark [27–34].

Both the precise measurement of V_{tb} and the indirect detection of new physics require an accurate calculation of the single-top-quark production cross section. The quark-antiquark-annihilation cross section has been calculated at next-to-leading order in QCD, with a theoretical uncertainty of $\pm 6\%$ [38]. The purpose of this chapter is to calculate the next-to-leading-order correction to the W-gluon-fusion cross section.

A complete calculation of the next-to-leading-order correction to W-gluon fusion has already been presented in the literature [62]. However, we show that this calculation is incor-

41
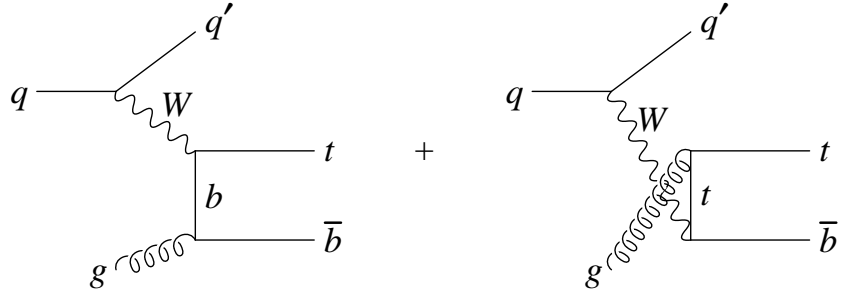
Figure 3.1: Single-top-quark production via W-gluon fusion.

rect, due to the factorization scheme used to subtract collinear divergences. We argue that

the CTEQ b-quark distribution function used in that calculation [63], although nominally in

the deep-inelastic scattering (DIS) scheme, is actually not compatible with that scheme, and

yields incorrect results. To avoid this problem, we perform our calculation entirely in the

modified minimal subtraction ($\overline{\text{MS}}$) scheme [64]. Our numerical results differ significantly

from those of Ref. [62].

We make several other contributions to the calculation of the next-to-leading-order cor-

rection to the W-gluon-fusion process:

1. We show that there are two independent corrections, of order $1/\ln(m_t^2/m_b^2)$ and α_s,

    which are numerically comparable. The leading-order process is $qb \to q't$, as shown

    in Fig. 3.2(a). The $1/\ln(m_t^2/m_b^2)$ correction is associated with the diagrams in Figs.

    3.2(b), 3.2(c), while the α_s correction arises from the diagrams in Figs. 3.3, 3.4. The

    existence of a correction of order $1/\ln(\mu^2/m_Q^2)$ is a generic feature of calculations in-

    volving perturbatively-derived heavy-quark distribution functions at an energy scale

    μ large compared with the heavy-quark mass m_Q.

2. We perform the calculation in a simple and systematic way using a structure-function approach [65, 66]. This allows the calculation to be organized in a straightforward manner, making use of its similarity with deep-inelastic scattering.

3. We carefully analyze the appropriate scale in the parton distribution functions. We show that the correct scale in the light-quark distribution function is $\mu^2 = Q^2$ (Q^2 is the virtuality of the W boson), with essentially no scale uncertainty. However, the appropriate scale in the b-quark distribution function is $\mu^2 \approx Q^2 + m_t^2$.

The chapter is organized as follows. In Sec. 3.1 we show that the next-to-leading-order corrections are of two types, $1/\ln(m_t^2/m_b^2)$ and α_s. We then argue that these corrections are most reliably calculated in the $\overline{\text{MS}}$ factorization scheme. In Sec. 3.2 we introduce the structure-function approach to calculating these corrections. In Sec. 3.3 we give our numerical results and draw conclusions. We give results for the Fermilab Tevatron $p\bar{p}$ collider for $\sqrt{S} = 1.8$ and 2 TeV, the CERN Large Hadron Collider (LHC), a pp collider with $\sqrt{S} = 14$ TeV, and the DESY ep collider HERA with $\sqrt{S} = 314$ GeV. The analytic expressions for the next-to-leading-order structure functions are gathered in Appendix C.

3.1   Next-to-leading-order corrections
3.1.1 $1/\ln(m_t^2/m_b^2)$ correction

The tree-level diagrams for W-gluon fusion are shown in Fig. 3.1. Since the b-quark mass is small compared with m_t, let us neglect it for the moment. If the b quark is massless, the first of these diagrams is singular when the final $\bar{b}$ quark is collinear with the incoming gluon. This kinematic configuration corresponds to the incoming gluon splitting into a real

43
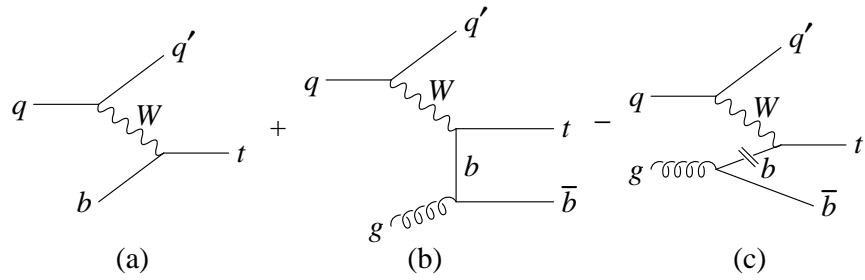
Figure 3.2: (a) Leading-order process for single-top-quark production, using a b-quark distribution function. (b) Correction to the leading-order process from an initial gluon. (c) Subtracting the collinear region from (b), corresponding to a gluon splitting into a $b\bar{b}$ pair. (b) and (c) taken together constitute a correction of order $1/\ln(m_t^2/m_b^2)$ to the leading-order process in (a).
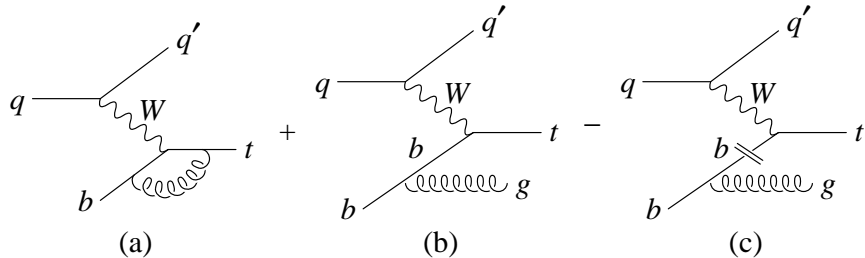
Figure 3.3: Order α_s correction to the heavy-quark vertex in the leading-order process $qb \to q't$. (c) represents the subtraction of the collinear region from (b).
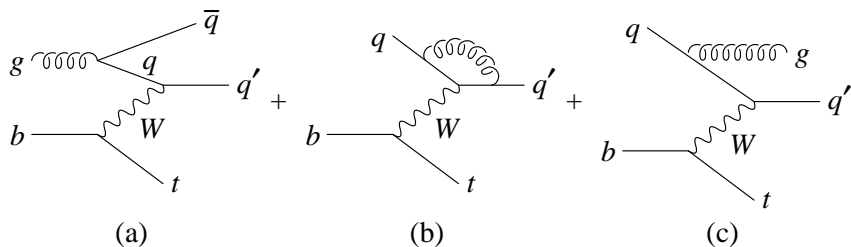
Figure 3.4: Order α_s correction to the light-quark vertex in the leading-order process $qb \to q't$.

44

$b\bar{b}$ pair. The propagator of the internal b quark in the diagram is therefore on-shell, and is infinite.

In reality the b quark is not massless, and its mass regulates the collinear singularity which exists in the massless case. The collinear singularity manifests itself in the total cross section as terms proportional to $\alpha_s \ln[(Q^2 + m_t^2)/m_b^2] + O(\alpha_s)$, where $Q^2 \equiv -q^2$ is the virtuality of the W boson of four-momentum q. Since the virtuality of the W boson is controlled by the W propagator, Q^2 is typically less than or of order M_W^2. For readability, we write the logarithm as $\ln(m_t^2/m_b^2)$ in the following discussion (since $m_t^2 \gg M_W^2$), although we use the exact expression in all calculations.

The total cross section for W-gluon fusion contains the logarithmically enhanced terms, of order $\alpha_s \ln(m_t^2/m_b^2)$, as well as terms of order α_s (both terms also carry a factor of α_W^2, which we suppress in the following discussion). Furthermore, logarithmically enhanced terms, of order $\alpha_s^n \ln^n(m_t^2/m_b^2)/n!$, appear at every order in the perturbative expansion in the strong coupling, due to collinear emission of gluons from the internal b-quark propagator. Since the logarithm is large, $\alpha_s \ln(m_t^2/m_b^2) \sim 0.7$–$0.8$, and the perturbation series does not converge quickly. Thus it appears difficult to obtain a precise prediction for the total cross section.

Fortunately, this difficulty can be obviated. A formalism exists to sum the collinear logarithms to all orders in perturbation theory [67–69]. The coefficient of the logarithmically-enhanced term is the Dokshitzer-Gribov-Lipatov-Altarelli-Parisi (DGLAP) splitting function P_{qg}, which describes the splitting of a gluon into a $b\bar{b}$ pair. One can sum the logarithms by introducing a b-quark distribution function $b(x, \mu^2)$ and calculating its evolution with μ (from some initial condition) via the DGLAP equations. Thus the b-quark distribution func-

tion can be regarded as a device to sum the collinear logarithms. Since it is calculated from the splitting of a gluon into a collinear $b\bar{b}$ pair, it is intrinsically of order $\alpha_s \ln(\mu^2/m_b^2)$. We elaborate on this point at the end of this section.

Once a b-quark distribution function is introduced, it changes the way one orders perturbation theory. The leading-order process is now $qb \to q't$, shown in Fig. 3.2(a). This cross section is of order $\alpha_s \ln(m_t^2/m_b^2)$, due to the b-quark distribution function ($\mu \approx m_t$). The W-gluon-fusion process, shown in Fig. 3.2(b), contains terms of both order $\alpha_s \ln(m_t^2/m_b^2)$ and α_s, as discussed above. However, the logarithmically enhanced terms have been summed into the b-quark distribution function and thus are already present in Fig. 3.2(a). It is therefore necessary to remove these terms from the W-gluon fusion process to avoid double counting. This is indicated schematically in Fig. 3.2(c); the double lines crossing the internal b-quark propagator indicate that it is on-shell, which corresponds to the kinematic region responsible for the large collinear logarithm [67–69].

After the subtraction of the terms of order $\alpha_s \ln(m_t^2/m_b^2)$ in Fig. 3.2(b) by the terms in Fig. 3.2(c), the remaining terms are of order α_s. Compared with the leading-order process in Fig. 3.2(a), this is suppressed by a factor $1/\ln(m_t^2/m_b^2)$. Thus the diagrams of Figs. 3.2(b) and 3.2(c), taken together, correspond to a correction to the leading-order cross section of $1/\ln(m_t^2/m_b^2)$, not of order α_s. This is an essential point which has been previously overlooked.

This observation is generic to any process involving a perturbatively derived heavy-quark distribution function in the region $\mu^2 \gg m_Q^2$. For example, the calculation analogous to the diagrams in Figs. 3.2(b), 3.2(c) for charm production in neutral-current deep inelastic scattering [69] corresponds to a correction of order $1/\ln(Q^2/m_c^2)$ for $Q^2 \gg m_c^2$.

46

Let us elaborate on our contention that the b-quark distribution function is intrinsically of order $\alpha_s \ln(\mu^2/m_b^2)$, rather than merely of order α_s. If one neglects gluon bremsstrahlung and the scale dependence of the gluon distribution function and the strong coupling, one can solve the DGLAP equation for the b-quark distribution function analytically [with the initial condition $b(x,\mu^2) = 0$ at $\mu = m_b$] [67–69]:

$$b(x,\mu^2) = \frac{\alpha_s(\mu^2)}{2\pi} \ln\left(\frac{\mu^2}{m_b^2}\right) \int_x^1 \frac{dz}{z} P_{qg}(z) g\left(\frac{x}{z},\mu^2\right) , \qquad (3.1)$$

where the DGLAP splitting function is given by

$$P_{qg}(z) = \frac{1}{2}[z^2 + (1-z)^2] . \qquad (3.2)$$

Equation (3.1) shows that $b(x,\mu^2)$ is of order $\alpha_s \ln(\mu^2/m_b^2)$ compared with the gluon distribution function. To support this, we show in Fig. 3.5 the ratio $b(x,\mu^2)/g(x,\mu^2) \times 2\pi/\alpha_s(\mu^2)$ as a function of μ for various fixed values of x, using the CTEQ4M parton distribution functions [70]. Note that $x \sim m_t/\sqrt{S} \sim 0.1$ at the Tevatron, and $x \sim 0.01$ at the LHC. The curves are approximately linear when μ is plotted on a logarithmic scale, indicating that $b(x,\mu^2) \propto [\alpha_s(\mu^2)/2\pi] \ln(\mu^2/m_b^2) g(x,\mu^2)$.

The b-quark distribution function is on a different footing from the light-quark distribution functions. The light-quark distribution functions involve nonperturbative QCD, and must be measured (or calculated nonperturbatively). The b-quark distribution function involves energies of order m_b and larger, so it can be calculated perturbatively; no measurement is necessary. Given the gluon and light-quark distributions functions, perturbative QCD makes a definite prediction for the b-quark distribution function.

3.1.2 α_s correction

There are also bona fide α_s corrections to the leading-order process $qb \to q't$. The di-

47
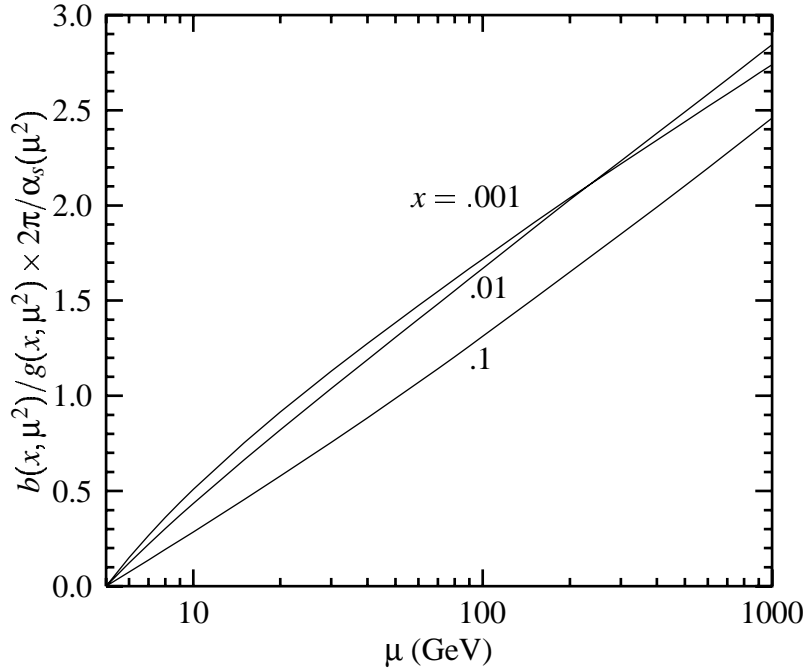
Figure 3.5: The ratio of the b-quark distribution function to the gluon distribution function, times $2\pi/\alpha_s(\mu^2)$, versus the factorization scale μ, for various fixed values of x. The curves are approximately linear when μ is plotted on a logarithmic scale, indicating that $b(x,\mu^2) \propto [\alpha_s(\mu^2)/2\pi] \ln(\mu^2/m_b^2)g(x,\mu^2)$, as suggested by the approximation of Eq. (3.1).

agram in Fig. 3.3(a) is such a correction; it is of order $\alpha_s^2 \ln(m_t^2/m_b^2)$ [including the factor

$\alpha_s \ln(m_t^2/m_b^2)$ from the b-quark distribution function], so it is suppressed by a factor of α_s

with respect to the leading-order process.

The diagram of Fig. 3.3(b) contains terms of order $\alpha_s^2 \ln^2(m_t^2/m_b^2)$ and $\alpha_s^2 \ln(m_t^2/m_b^2)$.

The former terms arise from the collinear emission of the gluon, which gives rise to another

factor of $\ln(m_t^2/m_b^2)$ (on top of the factor from the b-quark distribution function). Similar to

the discussion above, another power of this logarithm appears at every order in the strong

coupling, and summation is required to improve the convergence of perturbation theory.

The coefficient of this logarithmically enhanced term is the DGLAP splitting function P_{qq},

48

which describes the splitting of a quark into a quark and a gluon. The collinear logarithms are summed by adding another term, corresponding to gluon emission, to the DGLAP evolution equation for the b-quark distribution function. Once this is done, the collinear region must be subtracted from Fig. 3.3(b); this is shown schematically in Fig. 3.3(c). The remaining terms are of order $\alpha_s^2 \ln(m_t^2/m_b^2)$, so they are bona fide α_s corrections to the leading-order process.

Finally, there are the corrections to the light-quark vertex in the leading-order process, as shown in Fig. 3.4. These are also bona fide α_s corrections. Figs. 3.4(a), 3.4(b) contain collinear logarithms $\ln(Q^2/m_q^2)$ (where m_q is a light-quark mass) which are absorbed by the light-quark distribution functions in the usual way. Since the light-quark distribution functions are intrinsically of zeroth order in α_s, the remaining corrections are of order α_s.

3.1.3   Higher orders

Consider the next-to-next-to-leading-order diagram in Fig. 3.6. This diagram generates terms of order $\alpha_s^2 \ln^2(m_t^2/m_b^2)$, $\alpha_s^2 \ln(m_t^2/m_b^2)$, and α_s^2. The term of order $\alpha_s^2 \ln^2(m_t^2/m_b^2)$ comes from the region in which the initial gluon splits into a collinear $b\bar{b}$ pair, and the b quark subsequently radiates a collinear gluon. This term is summed by the leading-order DGLAP equation, which sums all leading logarithms $\alpha_s^n \ln^n(m_t^2/m_b^2)/n!$, as discussed in Sec. 3.1.1. Thus this term is already present in the leading-order diagram, Fig. 3.2(a).

The terms of order $\alpha_s^2 \ln(m_t^2/m_b^2)$ come from two sources. The first is when the initial gluon splits into a collinear $b\bar{b}$ pair, and the b quark subsequently radiates a noncollinear gluon. This is associated with the diagrams in Figs. 3.3(b) and 3.3(c), taken together, which correspond to noncollinear gluon radiation. The logarithm is summed via the leading-order

49
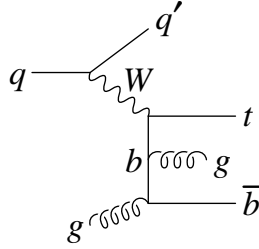
Figure 3.6: Next-to-next-to-leading-order contribution to single-top-quark production via W-gluon fusion.

DGLAP equation into the b-quark distribution function in Figs. 3.3(b), 3.3(c), so this term is already accounted for.

The other term of order $\alpha_s^2 \ln(m_t^2/m_b^2)$ is summed by extending the DGLAP splitting function P_{qg} to next-to-leading order. This sums the first subleading logarithms, of order $\alpha_s^n \ln^{n-1}(m_t^2/m_b^2)$ ($n \geq 2$) into the b-quark distribution function of the leading-order process, Fig. 3.2(a). The remaining term, of order α_s^2, is a correction of order $\alpha_s \times 1/\ln(m_t^2/m_b^2)$ compared with the leading-order process of Fig. 3.2(a).

This analysis demonstrates that all collinear logarithms are ultimately summed into the b-quark distribution function; no explicit collinear logarithms remain. The remaining terms are all of order α_s^n or, if the diagram has a b quark in the initial state, of order $\alpha_s^n \ln(m_t^2/m_b^2)$. These correspond to corrections of order $\alpha_s^{n-1} \times 1/\ln(m_t^2/m_b^2)$ or α_s^{n-1}, respectively, compared with the leading-order process. For a more detailed discussion of higher orders, see Ref. [71].

3.1.4   Factorization scheme for heavy quarks

The factorization scheme used to eliminate the collinear divergences from the parton

cross section must be the same as the scheme used to define the parton distribution functions in order to yield a correct (and scheme-independent) result. In the $\overline{\text{MS}}$ scheme, the b-quark distribution function $b(x,\mu^2)$ is defined to be zero at $\mu = m_b$, and is then evolved to higher values of μ via the DGLAP equations [64]. This is the definition of the b-quark distribution function employed in the CTEQ $\overline{\text{MS}}$ parton distribution functions [63, 70].

Another popular factorization scheme is the DIS scheme. In this scheme, the neutral-current structure function $F_2(x,Q^2)$ is defined to have no radiative correction for light quarks. For $\mu \gg m_b$, the b quark is essentially a light quark, so a natural interpretation of the DIS scheme for the b quark is that its contribution to $F_2(x,Q^2)$ has no radiative correction. This is the interpretation that was made in Ref. [62], which adopted the DIS scheme for the parton cross section and used the CTEQ DIS distribution functions [63]. However, the CTEQ DIS b-quark distribution function is actually not in the DIS scheme as interpreted in Ref. [62]. Rather, the b-quark distribution function is again defined by the initial condition $b(x,\mu^2) = 0$ at $\mu = m_b$, and evolved to higher values of μ via the DGLAP equations. There is no sense in which this yields a b-quark distribution function which is formally equivalent to the usual DIS scheme. As a consequence, it is not correct to calculate the parton cross section in the usual DIS scheme when using the CTEQ DIS b-quark distribution function. The same is true of the CTEQ DIS charm distribution function.

To avoid this problem, we calculate entirely in the $\overline{\text{MS}}$ scheme. This yields very different numerical results from the calculation of Ref. [62] in the DIS scheme.

3.2   Structure-function approach

Inspecting the leading-order process in Fig. 3.2(a), $qb \to q't$, one observes that it is
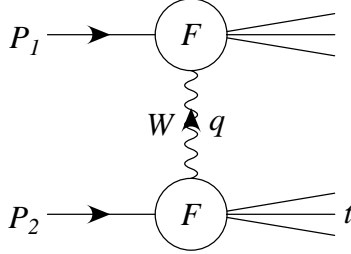
Figure 3.7: Single-top-quark production via W-gluon fusion from a structure-function point of view. The W boson initiates deep inelastic scattering on both hadrons.

analogous to charged-current deep-inelastic scattering. In fact, it is double deep-inelastic scattering; the virtual W boson is probing both the hadron containing the b quark, and the hadron containing the light quark, q. This is shown schematically in Fig. 3.7. We can exploit this analogy to calculate the corrections to this process in a compact way, in terms of next-to-leading-order hadronic structure functions [65, 66]. This factorization of the process is exact at next-to-leading order, because diagrams involving gluon exchange between the light-quark and heavy-quark lines do not interfere with the tree diagram, due to color conservation.[1]

The hadronic tensor describing a W boson of four-momentum q striking a hadron of four-momentum P can be written in terms of five structure functions:

$$
\begin{aligned}
MW_{\mu\nu}(x,Q^2) &= F_1(x,Q^2)\left(-g_{\mu\nu}+\frac{q_\mu q_\nu}{q^2}\right)+\frac{F_2(x,Q^2)}{P\cdot q}\left(P_\mu-\frac{P\cdot q}{q^2}q_\mu\right)\left(P_\nu-\frac{P\cdot q}{q^2}q_\nu\right) \\
&\quad -i\frac{F_3(x,Q^2)}{2P\cdot q}\varepsilon_{\mu\nu\rho\sigma}P^\rho q^\sigma+F_4(x,Q^2)q_\mu q_\nu+F_5(x,Q^2)(P_\mu q_\nu+P_\nu q_\mu)\,, (3.3)
\end{aligned}
$$

where $Q^2 = -q^2$. If the struck quark, and the quark into which it is converted, are both massless, then the current with which the W interacts is conserved, and one has $q^\mu W_{\mu\nu} =$

---

[1] Since $\mathrm{Tr}(T^A) = 0$, terms in the square of the matrix element that involve only one internal gluon vanish.

52

$q^{\nu}W_{\mu\nu} = 0$. This implies that the structure functions F_4, F_5 vanish. The scaling variable x is given by $x = Q^2/2P \cdot q$, as usual.

If the quark into which the struck quark is converted is massive, such as the top quark, then the current is no longer conserved, and F_4, F_5 are nonvanishing (although we will find that they do not enter our calculation). Furthermore, the scaling variable is now given by $x = (Q^2 + m_t^2)/2P \cdot q$.

The hadronic cross section in Fig. 3.7 is obtained by contracting the hadronic tensors at each vertex with the square of the W propagator connecting them. Due to current conservation of the light-quark tensor, the $q^{\mu}q^{\nu}/M_W^2$ term in the numerator of the W propagator does not contribute, so one simply contracts the two tensors together. One finds

$$MW_{\mu\nu}(x_1, Q^2)MW^{\mu\nu}(x_2, Q^2) =$$

$$3F_1(x_1, Q^2)F_1(x_2, Q^2)$$

$$+ F_1(x_1, Q^2)F_2(x_2, Q^2)\frac{P_2 \cdot (-q)}{q^2} + F_2(x_1, Q^2)F_1(x_2, Q^2)\frac{P_1 \cdot q}{q^2}$$

$$+ F_2(x_1, Q^2)F_2(x_2, Q^2)\frac{1}{P_1 \cdot qP_2 \cdot (-q)}\left(P_1 \cdot P_2 - \frac{P_1 \cdot qP_2 \cdot q}{q^2}\right)^2$$

$$+ \frac{1}{2}F_3(x_1, Q^2)F_3(x_2, Q^2)\left(\frac{P_1 \cdot P_2 q^2}{P_1 \cdot qP_2 \cdot q} - 1\right), \tag{3.4}$$

where

$$Q^2 = -q^2, \tag{3.5}$$

$$x_1 = \frac{Q^2}{2P_1 \cdot q}, \tag{3.6}$$

$$x_2 = \frac{Q^2 + m_t^2}{2P_2 \cdot (-q)}. \tag{3.7}$$

The heavy-quark structure functions F_4, F_5 do not contribute to this expression because they are the coefficients of tensors which contain q^{μ}, q^{ν}, or both. These tensors give vanishing

53

contribution when contracted with the light-quark tensor, due to current conservation. The W boson interacts with massless quarks in the hadron of four-momentum P_1, and interacts with a b quark in the hadron of four-momentum P_2, as indicated in Fig. 3.7. Note that the latter hadron is probed by a W boson of four-momentum $-q$, which results in $P_2 \cdot (-q)$ appearing in several places in Eq. (3.4). One must also add the contribution where the W boson interacts with massless quarks in the hadron of four-momentum P_2 and with the b quark in the hadron of four-momentum P_1.

The differential hadronic cross section is given by [66][2]

$$d\sigma = \frac{1}{2S} 4 \left(\frac{g^2}{8}\right)^2 \frac{1}{(Q^2+M_W^2)^2} MW_{\mu\nu}(x_1,Q^2) MW^{\mu\nu}(x_2,Q^2) (2\pi)^2 \frac{1}{4S} dQ^2 dW_1^2 dW_2^2 \;, \quad (3.8)$$

where $W_1^2 = (P_1+q)^2$ and $W_2^2 = (P_2-q)^2$ are the squared invariant masses of the hadron remnants (including the top quark), and $S = 2P_1 \cdot P_2$ is the square of the hadronic center-of-momentum energy. Using

$$2P_1 \cdot q \;=\; W_1^2 + Q^2 \;, \quad (3.9)$$

$$2P_2 \cdot (-q) \;=\; W_2^2 + Q^2 \;, \quad (3.10)$$

we can write Eq. (3.4) in terms of the integration variables Q^2, W_1^2, W_2^2:

$$MW_{\mu\nu}(x_1,Q^2) MW^{\mu\nu}(x_2,Q^2) =$$

$$3F_1(x_1,Q^2)F_1(x_2,Q^2)$$

$$-\frac{1}{2}F_1(x_1,Q^2)F_2(x_2,Q^2)\frac{W_2^2+Q^2}{Q^2} - \frac{1}{2}F_2(x_1,Q^2)F_1(x_2,Q^2)\frac{W_1^2+Q^2}{Q^2}$$

$$+ F_2(x_1,Q^2)F_2(x_2,Q^2)\frac{1}{(W_1^2+Q^2)(W_2^2+Q^2)}\left(S - \frac{(W_1^2+Q^2)(W_2^2+Q^2)}{2Q^2}\right)^2$$

$$+ F_3(x_1,Q^2)F_3(x_2,Q^2)\left(\frac{SQ^2}{(W_1^2+Q^2)(W_2^2+Q^2)} - \frac{1}{2}\right) \;, \quad (3.11)$$

---

[2]This equation is obtained from Eq. (2) of Ref. [66] by setting $d\Gamma = 0$ and integrating out the four-dimensional Dirac δ function.

54

where

$$x_1 = \frac{Q^2}{W_1^2 + Q^2} \,, \tag{3.12}$$

$$x_2 = \frac{Q^2 + m_t^2}{W_2^2 + Q^2} \,. \tag{3.13}$$

The physical region is given by

$$W_1 \geq 0 \,, \tag{3.14}$$

$$W_2 \geq m_t \,, \tag{3.15}$$

$$W_1 + W_2 \leq \sqrt{S} \,, \tag{3.16}$$

$$Q^2_{\substack{max \\ min}} = \frac{1}{2}[S - W_1^2 - W_2^2 \pm \lambda^{1/2}(S, W_1^2, W_2^2)] \,, \tag{3.17}$$

$$\lambda(a,b,c) = a^2 + b^2 + c^2 - 2ab - 2ac - 2bc \,. \tag{3.18}$$

The next-to-leading-order expressions for the structure functions are given in Appendix C. We use the $\overline{\text{MS}}$ scheme, for the reasons discussed in Sec. 3.1.4. After the subtraction of the collinear logarithms $\ln[(Q^2 + m_t^2)/m_b^2]$, we set the b-quark mass to zero, since it is small compared with the top-quark mass.[3] When evaluating the next-to-leading-order contribution to the cross section, we use the next-to-leading-order expression for the structure function corresponding to the light quark or the heavy quark, but not both at the same time, as this would yield a contribution of next-to-next-to-leading order.

3.2.1 Factorization scale

The similarity of the leading-order process $qb \to q't$ with deep inelastic scattering suggests that the relevant scale in the light-quark distribution function is $\mu^2 = Q^2$. If the parton

---

[3]In practice, it is simpler to set the b-quark mass to zero from the outset, and evaluate the cross section in $N = 4 - 2\varepsilon$ dimensions. The collinear logarithms appear as terms proportional to $1/\varepsilon - \gamma + \ln 4\pi$, and are subtracted in the $\overline{\text{MS}}$ scheme.

distribution functions were extracted solely from deep-inelastic-scattering data at the same values of x and Q^2 relevant to this process, this statement would be exactly correct, because the radiative corrections to deep-inelastic scattering are precisely the same as those to the light-quark vertex in $qb \to q't$. The latter process has additional radiative corrections, both to the heavy-quark vertex and between the two quark lines, but these are unrelated to the scale in the light-quark distribution function.

The actual situation is not far from the situation described above. Most of the information on the light-quark distribution functions does come from deep inelastic scattering, and the relevant values of x and Q^2 are within the range of the HERA ep collider: $x \sim m_t/\sqrt{S} \sim$ 0.1 at the Tevatron and $x \sim 0.01$ at the LHC, with $Q^2 \lesssim M_W^2$. We therefore set $\mu^2 = Q^2$ in the light-quark distribution function and refrain from varying the scale, as is usually done to estimate the theoretical uncertainty from uncalculated higher-order corrections.

The situation is entirely different for the scale in the b-quark distribution function. The collinear logarithm that results from the diagrams in Figs. 3.2(b) and 3.3(b) is $\ln[(Q^2 + m_t^2)/m_b^2]$. Upon subtraction of the collinear region via the diagrams in Figs. 3.2(c) and 3.3(c), the remaining logarithm is $\ln[(Q^2 + m_t^2)/\mu^2]$ (see Appendix C). The appropriate scale in the b-quark distribution function is therefore $\mu^2 \approx Q^2 + m_t^2$. Since the b-quark distribution is obtained from an entirely theoretical calculation, we vary this scale in order to estimate the uncertainty from uncalculated higher-order corrections.

The argument above shows that the appropriate scales in the light-quark and b-quark distribution functions are different. Although it may seem unfamiliar to have different scales in the parton distribution functions of a given hadronic process, we have shown that it is appropriate in this case. The appropriate scale for the production of a quark of mass m_Q

via charged-current deep inelastic scattering is $\mu^2 = Q^2 + m_Q^2$, which yields $\mu^2 = Q^2$ for the light-quark structure function and $\mu^2 = Q^2 + m_t^2$ for the top-quark charged-current structure function.

3.3 Results and Conclusions

We evaluate the next-to-leading-order cross section for single-top-quark production via W-gluon fusion using the latest CTEQ $\overline{MS}$ distribution functions, CTEQ4M [70]. The cross sections at the Tevatron (1.8 and 2 TeV) and the LHC for the sum of t and $\bar{t}$ production for[4] $m_t = 175$ GeV are given in[5] Table 3.1, assuming $V_{tb} = 1$. The leading-order cross sections are also evaluated with the CTEQ4M distribution functions. (When evaluated with the CTEQ4L leading-order distribution functions, the leading-order cross sections are 1.61, 2.31, and 237 pb at the three machines.) The $1/\ln(m_t^2/m_b^2)$ and α_s corrections are listed separately. The $1/\ln(m_t^2/m_b^2)$ correction is -20% at the Tevatron, and -11% at the LHC. This confirms previous calculations of this correction in the $\overline{MS}$ scheme [27,72,73]. The α_s correction is $+12\%$ at the Tevatron, and $+2\%$ at the LHC. The next-to-leading-order cross section is the sum of the leading-order cross section and these two corrections. The fact that the α_s correction partially compensates the $1/\ln(m_t^2/m_b^2)$ correction is a numerical accident, as these are two truly independent parameters.

Also given in Table 3.1 is the cross section for $e^- p \rightarrow \nu_e \bar{t} b$ or $e^+ p \rightarrow \bar{\nu}_e t \bar{b}$ at HERA [74–76]. (The leading-order cross section is 1.21×10^{-4} pb when evaluated with the CTEQ4L

---

[4]The current world-average top-quark mass is 174.1 ± 5.4 GeV [6].

[5]The numerical results in Table 3.1 were obtained by evaluating the weak coupling constant g in terms of the Fermi coupling G_F and the W-boson mass M_W, via $g^2 = 8G_F M_W^2 / \sqrt{2}$, where $G_F = 1.16639 \times 10^{-5}$ GeV^{-2} and $M_W = 80.4$ GeV. These numerical results are approximately 2% less than the values which appear in the published version of this chapter [Phys. Rev. D **56**, 5919 (1997)].

Table 3.1: Cross sections for single-top-quark production via W-gluon fusion at the Tevatron, LHC, and HERA for $m_t = 175$ GeV. The cross sections are the sum of t and $\bar{t}$ production at the Tevatron and the LHC, and either t (positron beam) or $\bar{t}$ (electron beam) at HERA. The first column gives the leading-order cross section [Fig. 3.2(a)]; the second column the correction of order $1/\ln(m_t^2/m_b^2)$ [Figs. 3.2(b), 3.2(c)]; the third column the correction of order α_s (Figs. 3.3, 3.4); and the last column the next-to-leading-order cross section (the sum of the first three columns). All calculations are performed in the $\overline{\text{MS}}$ scheme using CTEQ4M parton distributions functions with $\mu^2 = Q^2$ for the light-quark vertex and $\mu^2 = Q^2 + m_t^2$ for the heavy-quark vertex.

$\sqrt{S}$	LO (pb)	$1/\ln(m_t^2/m_b^2)$ (pb)	α_s (pb)	NLO (pb)
1.8 TeV $p\bar{p}$	1.84	-0.39	0.25	1.70
2 TeV $p\bar{p}$	2.67	-0.55	0.32	2.44
14 TeV pp	270	-31	6	245
314 GeV ep	1.02×10^{-4}	-0.34×10^{-4}	0.36×10^{-4}	1.04×10^{-4}

leading-order distribution functions.) The $1/\ln(m_t^2/m_b^2)$ correction is -33%, and the α_s correction is $+36\%$. An integrated luminosity of about 10 fb^{-1} would be needed to produce a single event. This is unattainable given the design luminosity of the machine ($\mathcal{L} = 1.6 \times 10^{31}/cm^2/s$).

We argued in Sec. 3.1.3 that the CTEQ DIS b-quark distribution function is incompatible with the usual DIS scheme, and yields incorrect results. To demonstrate this, we also perform the calculation in the DIS scheme using CTEQ4D distribution functions. The next-to-leading-order cross sections at the Tevatron (1.8 and 2 TeV) and the LHC are found to be 2.24, 3.20, 290 pb. These differ from the results in the $\overline{\text{MS}}$ scheme by much more than the theoretical uncertainty in that calculation, which we now estimate.

To estimate the uncertainty from uncalculated higher-order corrections, we vary the scale in the b-quark distribution function about the central value $\mu^2 = Q^2 + m_t^2$. The results are

shown in Fig.3.8 at the Tevatron (2 TeV) and the LHC, for both the leading-order and next-to-leading-order cross sections, using the CTEQ4M parton distribution functions. The next-to-leading-order cross section is considerably less sensitive to μ, as expected. Varying μ between one-half and twice its central value yields an uncertainty in the next-to-leading-order cross section of $\pm 5\%$ at the Tevatron and $\pm 4\%$ at the LHC. As discussed in Sec. 3.2, we do not vary the scale in the light-quark distribution function, where $\mu^2 = Q^2$. Although our estimate of the theoretical uncertainty in the cross section from uncalculated higher orders is rather small, it would be worthwhile to pursue the calculation to the next order in α_s.

Another source of uncertainty stems from the uncertainty in the top-quark mass. The cross section as a function of the top-quark mass is shown in Fig. 3.9 at the Tevatron (2 TeV) and the LHC. The cross section is relatively insensitive to the top-quark mass because the decrease in the parton distribution functions with increasing m_t is not augmented by a decrease in the partonic cross section, which scales like $1/M_W^2$ instead of $1/\hat{s}$. The present uncertainty of ± 5.4 GeV in the top-quark mass [6] corresponds to an uncertainty of $\pm 9\%$ in the cross section at the Tevatron and $\pm 5\%$ at the LHC. Anticipating an uncertainty of ± 2 GeV in the top-quark mass from Run II at the Tevatron and/or from the LHC reduces the uncertainty in the cross section from the top-quark mass to $\pm 3\%$ at the Tevatron and $\pm 2\%$ at the LHC.

The most significant source of uncertainty is currently the uncertainty in the gluon distribution function, which reflects itself as an uncertainty in the b-quark distribution function. A recent paper by the CTEQ collaboration [77] has attempted to quantify this uncertainty for the CTEQ4M [70] distribution functions. Specifically, they have made a very conservative estimate of the error in gluon-gluon, and gluon-quark initial states. The result is that for
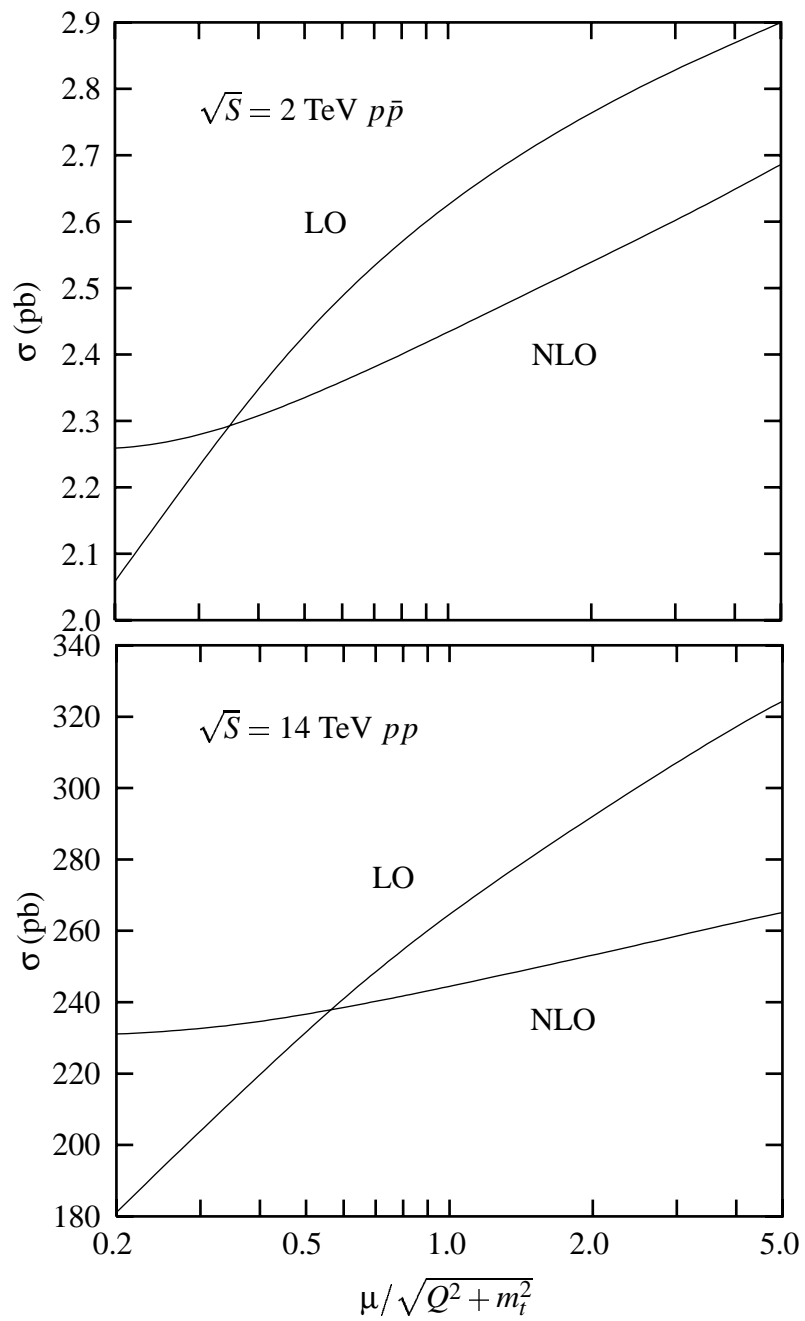
Figure 3.8: Cross section for single-top-quark production via W-gluon fusion at the Tevatron and the LHC for $m_t = 175$ GeV, versus the ratio of the factorization scale μ to its natural value, $\mu = \sqrt{Q^2 + m_t^2}$. Both the leading-order and next-to-leading-order cross sections are shown.
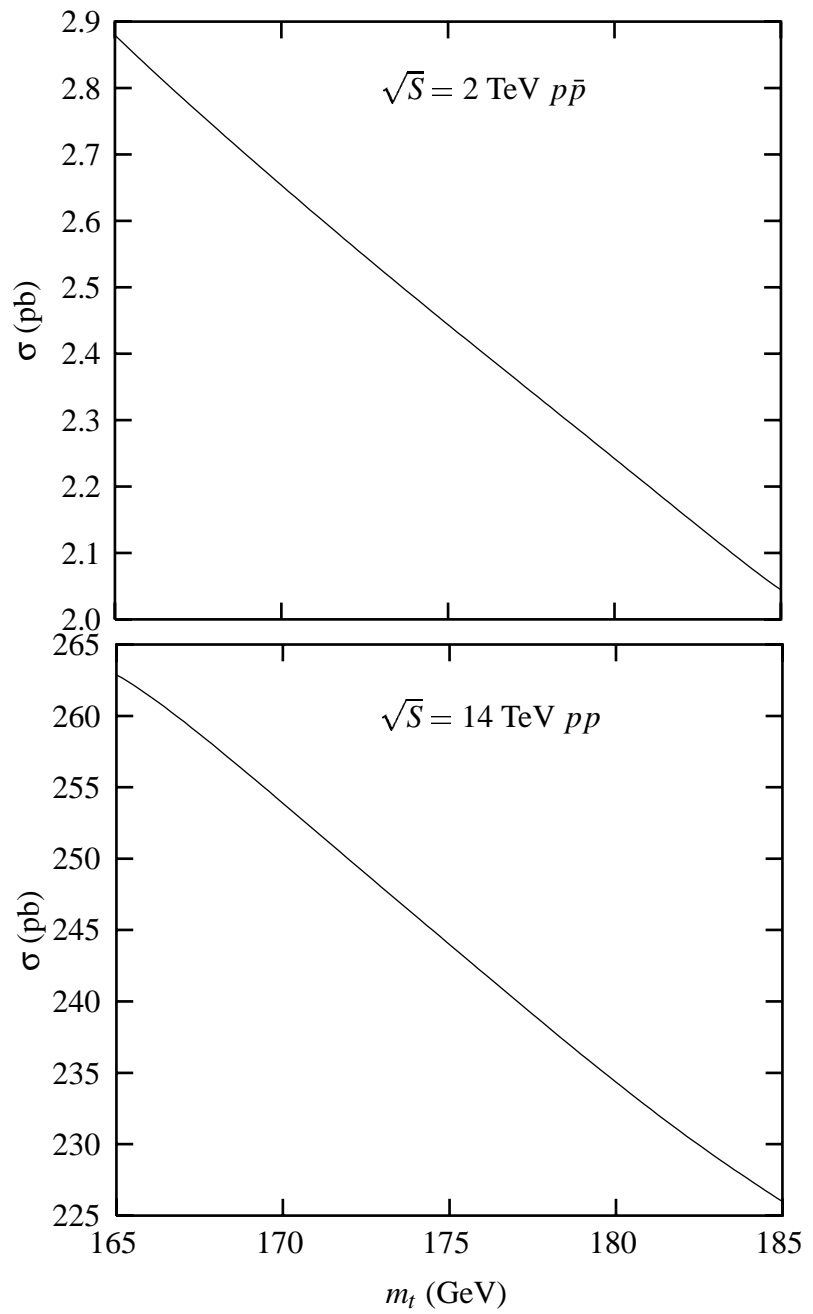
Figure 3.9: Next-to-leading-order cross section for single-top-quark production via
W-gluon fusion at the Tevatron and the LHC as a function of the top-quark mass.

single-top-quark production, given the relevant range of $x \sim 0.01$–0.1 and scale μ, the error is less than 10% at both the Tevatron and the LHC. This is not as good an estimate of the error as having a parton distribution set with an associated error-correlation matrix. However, Ref. [77] points out that there is currently no known way to quantify the theoretical uncertainties in combining the experimental data sets. Also, only a few experiments themselves have provided correlation information. Thus we shall have to use 10% as a benchmark for the uncertainty due to parton distribution functions for now.

We present the first complete and correct calculation of the next-to-leading-order corrections to single-top-quark production via W-gluon fusion. We estimate the uncertainty due to uncalculated higher-order corrections to be about $\pm 5\%$ at the Tevatron and the LHC. Assuming the uncertainty in the gluon distribution function can be further quantified and reduced below 10%, single-top-quark production via W-gluon fusion will be an accurate probe of the charged-current interaction of the top quark at the Tevatron and the LHC. In conjunction with $q\bar{q} \to t\bar{b}$, it will yield an accurate measurement of V_{tb} and possibly indicate the presence of new physics.

In this chapter, we resum large logarithms $\ln[(Q^2 + m_t^2)/m_b^2]$ via DGLAP evolution which leads to a reordering of perturbation theory. In Sec. 3.1 we show that there are two independent corrections, of order $1/\ln(m_t^2/m_b^2)$ and α_s, which are numerically comparable. Because this is double deep-inelastic scattering, a structure-function approach is used in Sec. 3.2 to evaluate the cross sections listed in Table 3.1. In Sec. 3.2.1 we show that the appropriate choice of scale μ in deep-inelastic scattering is $\mu^2 = Q^2 + m_q^2$, where m_q is the mass of the final state quark. Finally, we argue in Sec. 3.1.4 that the CTEQ4D charm and bottom-quark parton distribution functions are not actually in the DIS scheme. Therefore,

we recommend the use of the $\overline{\text{MS}}$ scheme for calculations with heavy-quark initial states.

Chapter 4

Single-top-quark production at hadron colliders

Single-top-quark production at the Fermilab Tevatron and the CERN Large Hadron Collider (LHC) provides an opportunity to study the charged-current weak-interaction of the top quark [27, 57–61, 73]. Within the standard model, single-top-quark production offers a means to directly measure the Cabibbo-Kobayashi-Maskawa (CKM) matrix element V_{tb}. Beyond the standard model, it is sensitive to a non-standard Wtb vertex, and to exotic single-top-quark production processes involving new particles [27–35]. In order to be a useful probe, the measurement of single-top-quark production must be accompanied by an accurate calculation of the standard-model production cross section and experimental acceptance, as well as an analysis of the associated backgrounds.

It is useful to distinguish between three different types of single-top-quark production, based on the virtuality of the W boson. Fig. 4.1(a) shows the leading-order Feynman diagram for s-channel[1] single-top-quark production [57, 58]. This process has the theoretical advantage of proceeding via quark-antiquark annihilation, so the partonic flux can be constrained from Drell-Yan data [78]. The next-to-leading-order calculation has been per-

---

[1] The s-channel process is sometimes referred to as the W^* process; however, the W boson in the t-channel process is also off-shell.
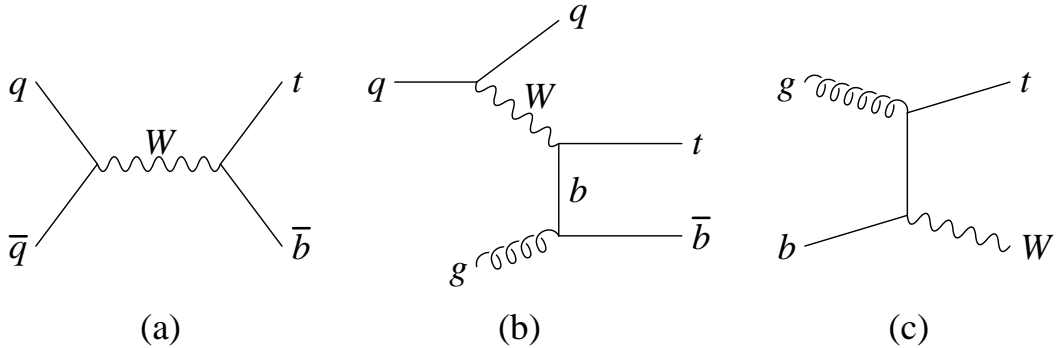
Figure 4.1: Feynman diagrams for single-top-quark production at hadron colliders: (a) s-channel production, (b) t-channel production (W-gluon fusion), and (c) associated production with a W boson.

formed for this channel [38], as well as a study of the acceptance and backgrounds [5, 58].

Fig. 4.1(b) shows a Feynman diagram for t-channel single-top-quark production, often referred to as W-gluon fusion [27,59–61,73]. The primary advantage of this channel is statistics. The cross section is almost three times larger than that of the s-channel process at the Tevatron, and the cross section at the LHC is 100 times larger than at the Tevatron. The production cross section was recently calculated by us at next-to-leading order (see Chapter 3, [8, 62]), and the acceptance and backgrounds have been most completely studied in Ref. [5]. Fig. 4.1(c) shows a Feynman diagram for Wt production, where an on-shell W is produced [73, 79]. This process proceeds via a gluon-b interaction, which makes the cross section negligible at the Tevatron. However, at the LHC it contributes about 20% of the total single-top-quark cross section. Neither the next-to-leading-order cross section,[2] nor the calculation of the acceptance and backgrounds for this process, are yet available.

In this chapter we calculate the acceptance and backgrounds for single-top-quark pro-

---

[2]The next-to-leading-order cross section is available for the identical process of Wc production [80].

65

duction via W-gluon fusion at the Tevatron and LHC. There are a number of differences with the analysis of Ref. [5]. The most significant improvement is that we perform an accurate calculation of the acceptance, using our next-to-leading-order calculation of the total cross section. This is an essential ingredient in the extraction of the cross section from experiment, and can be used to normalize any future studies. The acceptance cannot simply be calculated by comparing the cross section from Fig. 4.1(b) with and without cuts, because the total cross section is not obtained solely from Fig. 4.1(b), due to the breakdown of perturbation theory in the region where the initial gluon splits into a nearly-collinear $b\bar{b}$ pair. The correct way to treat the collinear region and calculate the acceptance is discussed in detail in Sec. 4.1.

Our analysis of backgrounds differs from that of Ref. [5] in that we advocate the use of one and only one b tag to isolate the signal, while Ref. [5] requires one or more b tags. The main motivation for this is that we desire to separate single-top-quark production via W-gluon fusion (which usually has only the b quark from top decay in the fiducial region) from the s-channel process (which usually has a b and a $\bar{b}$ in the fiducial region, and is found by double b-tagging). This provides two independent measures of V_{tb} with different backgrounds and theoretical uncertainties. Perhaps more importantly, the two processes are generally influenced by new physics in different ways, so looking for a deviation of each process from the standard model would be a useful diagnostic [27–35]. For discovery of single-top-quark production, and first measurements of V_{tb}, we also consider the total single-top-quark production cross section with only one b tag.

Since the top quark is produced via the weak interaction in single-top-quark processes, it has significant polarization [60]. An optimal basis for the measurement of this polarization,

66

both for the *s*-channel process and for *W*-gluon fusion, was recently introduced in Ref. [39]. We quantify the integrated luminosity required to observe and measure this polarization, including the effects of acceptance and jet reconstruction.

The chapter is organized as follows. In Sec. 4.1 we calculate the acceptance for single-top-quark production via *W*-gluon fusion. We pay particular attention to the issues associated with the splitting of the initial gluon into a nearly-collinear $b\bar{b}$ pair. In Sec. 4.2 we briefly discuss our calculational techniques. In Sec. 4.3 we present results for the signal and backgrounds at the Tevatron and the LHC. Sec. 4.4 is concerned with the polarization of the top quark in single-top-quark processes. We summarize our results in Sec. 4.5.

4.1   Acceptance for *W*-gluon fusion

In Chapter 3 (Ref. [8]), we calculated the inclusive next-to-leading-order cross section for single-top-quark production via *W*-gluon fusion. The results are listed in the second column of Table 4.1. Experimentally, only the cross section which lies within the geometrical acceptance of the detector is measurable, so it is important to calculate this acceptance. Normally this is straightforward; one simply compares the tree-level cross section with and without cuts. However, the total cross section for *W*-gluon fusion cannot simply be calculated from Fig. 4.1(b), because perturbation theory breaks down in the region where the initial gluon splits into a nearly-collinear $b\bar{b}$ pair. Thus we must first find the correct way to calculate the acceptance.

The E_T spectrum of the $\bar{b}$ antiquark is shown with a solid line in Fig. 4.2. It is peaked at small E_T, because the internal *b*-quark propagator is close to being on shell when the initial gluon splits into a nearly-collinear $b\bar{b}$ pair. Since $d\sigma/dp_T^2 \sim 1/(p_T^2 + m_b^2)$, the cross section

Table 4.1: Cross sections (pb) for single-top-quark production via W-gluon fusion with $m_t = 175$ GeV. The second column is the total next-to-leading-order cross section (see Table 3.1, or Ref. [8]), and the third the cross section with the $\bar{b}$ antiquark below $p_{Tmax} = 20$ GeV. The uncertainty is estimated from the scale variation of the cross section, and does not include the uncertainty in the parton distribution functions nor the uncertainty in the top-quark mass.

$\sqrt{S}$	σ_{NLO}	$p_{Tmax} = 20$ GeV
1.8 TeV	1.70 ± 0.09	1.34 ± 0.14
2 TeV	2.44 ± 0.12	1.90 ± 0.20
14 TeV	245 ± 12	157 ± 16

with the p_T of the $\bar{b}$ antiquark above p_{Tmin} is proportional to $\ln[m_t^2/(p_{Tmin}^2 + m_b^2)]$. Another power of this logarithm appears at every order in perturbation theory via collinear gluon radiation from the internal b quark, so the expansion parameter is $\alpha_s \ln[m_t^2/(p_{Tmin}^2 + m_b^2)]$. Thus the calculation of the cross section is more accurate the larger the choice of p_{Tmin}.

Unfortunately, it is not practical to simply choose a large value of p_{Tmin} and measure the cross section for $Wb\bar{b}j$ (j denotes the light-quark jet from the emission of the t-channel W boson in Fig. 4.1(b); Wb are the decay products of the t quark). There is a large background from $t\bar{t}$ production, which yields the final state $WWb\bar{b}$; this mimics the signal when the additional W boson decays to two jets, and one jet is missed. To suppress this background we search for the signal in the final state Wbj, i.e. we demand that the $\bar{b}$ antiquark *not* appear in the final state.

Fortunately, the cross section with the $\bar{b}$ antiquark below p_{Tmax} can be calculated with good accuracy, provided p_{Tmax} is sufficiently large. This is achieved via a two-step procedure. In Chapter 3 we calculated the total cross section ($p_{Tmin} = 0$) and summed the logarithmically-enhanced terms, $\alpha_s^n \ln^n(m_t^2/m_b^2)/n!$, to all orders [27,67,68,72,73]. To calculate
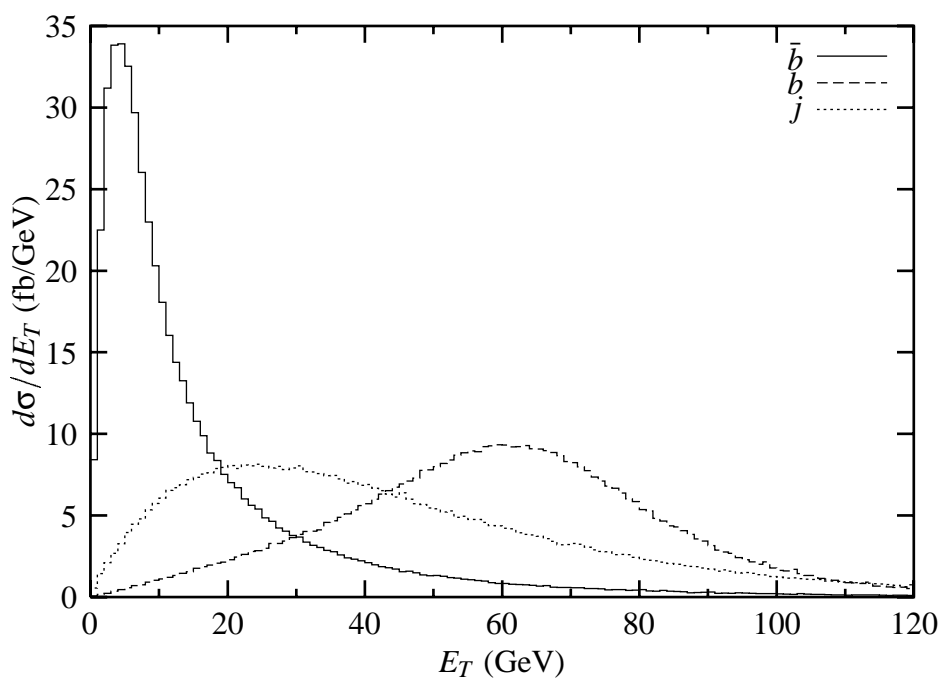
Figure 4.2: Transverse energy distributions for the spectator $\bar{b}$ antiquark (solid line), the b quark from top-quark decays (dashed line), and the light-quark jet j (dotted line), in single-top-quark production via W-gluon fusion at the Fermilab Tevatron.

the cross section with the $\bar{b}$ antiquark below p_{Tmax}, we simply take the total cross section and subtract from it the cross section with the $\bar{b}$ antiquark *above* $p_{Tmin} = p_{Tmax}$.

$$\sigma(p_{T\bar{b}} < p_{Tmax}) = \sigma_{NLO} - \sigma(p_{T\bar{b}} > p_{Tmax}) \, . \tag{4.1}$$

This amounts to integrating the momentum of the $\bar{b}$ antiquark over all momenta below p_{Tmax}. Since we do not want to detect this $\bar{b}$ antiquark (due to the $t\bar{t}$ background), it is not necessary to know its p_T spectrum below p_{Tmax} anyway.

We give in the third column of Table 4.1 the cross section for single-top-quark production via W-gluon fusion with the $\bar{b}$ antiquark below $p_{Tmax} = 20$ GeV. These numbers can be used to normalize future studies. For example, Ref. [5] studied the signal for the final state Wbq, using the process $qb \to qt$ to approximate the W-gluon fusion process, and normalizing to the total cross section. However, it is more accurate to normalize to the cross section with the $\bar{b}$ antiquark below some chosen p_{Tmax} (20 GeV in Ref. [5]).[3] HERWIG [81] and PYTHIA [82] also simulate single-top-quark production via W-gluon fusion using $qb \to qt$.

Our strategy is therefore as follows. We use the process in Fig. 4.1(b) to calculate the differential cross section for single-top-quark production via W-gluon fusion. If the p_T of the $\bar{b}$ antiquark is below p_{Tmax}, we normalize to the cross section calculated as described above. This yields most of signal cross section (Wbq in the fiducial region). If the p_T of the $\bar{b}$ antiquark is *above* p_{Tmax}, we simply use the cross section obtained from Fig. 4.1(b). This yields the final state $Wb\bar{b}q$, which we reject if all three jets are in the fiducial region, but which contributes to the signal if one jet is missed, one and only one of the two remaining jets is b-tagged and it, with the W boson, reconstructs to the top-quark mass (within some

---

[3]Ref. [5] normalized to a cross section of 1.6 pb; we see from Table 4.1 that a more accurate cross section is 1.90 pb.

70

resolution). This strategy avoids the occurrence of powers of $\alpha_s^n \ln^n(m_t^2/m_b^2)/n!$ at higher orders in perturbation theory, which would degrade the accuracy of the calculation.

4.1.1   Theoretical uncertainties

In Sec. 3.3, we studied the uncertainty in the next-to-leading-order total cross section for single-top-quark production via W-gluon fusion by varying the factorization scale in the b-quark distribution function. This indicated an uncertainty in the total cross section of $\pm 5\%$, not including the uncertainty in the parton distribution functions, or in the top-quark mass. However, to obtain the cross section with the p_T of the $\bar{b}$ antiquark below p_{Tmax}, we need to subtract from the total cross section the cross section with the p_T of the $\bar{b}$ antiquark above $p_{Tmin} = p_{Tmax}$, as discussed above. Since the latter is a tree-level calculation, its scale dependence is relatively large.

Using the scale $\mu^2 = p_{T\bar{b}}^2 + m_b^2$ in the gluon distribution function and the strong coupling, we find a $\pm 30\%$ uncertainty in the cross section with $p_{T\bar{b}} > 20$ GeV at the Tevatron ($\pm 15\%$ at the LHC) by varying μ between one half and twice its central value. Fortunately, this only accounts for 22% of the cross section at the Tevatron (35% at the LHC). Adding in quadrature the absolute uncertainty in the NLO cross section, and the cross section with $p_{T\bar{b}} > 20$ GeV, we find an uncertainty of about $\pm 10\%$ in the cross section with $p_{T\bar{b}} < 20$ GeV at both the Tevatron and the LHC. This uncertainty is reflected in the numbers in Table 4.1. To reduce this uncertainty would require the resummation of the large logarithms $\alpha_s \ln[m_t^2/(p_{Tmin}^2 + m_b^2)]$ which appear in the calculation of the cross section with the p_T of the $\bar{b}$ above p_{Tmin}.

Another source of uncertainty in the cross section is the uncertainty in the parton distri-

bution functions, especially the gluon distribution function. This uncertainty has recently been studied in Ref. [77], and it appears to be less than $\pm 10\%$ at both the Tevatron and the LHC. This is comparable to the uncertainty stemming from the scale variation described above. That study indicates that the uncertainty in the parton distribution functions could potentially be pushed below $\pm 10\%$.

The uncertainty in the top-quark mass also leads to an uncertainty in the cross section. The present uncertainty of ± 5.4 GeV [6] corresponds to an uncertainty in the cross section of $\pm 9\%$ (see Sec. 3.3). Anticipating an uncertainty of ± 3 GeV from Run II at the Tevatron corresponds to an uncertainty in the cross section of $\pm 5\%$, much less than the uncertainty from the scale variation and the parton distribution functions. The uncertainty in the top-quark mass at the Tevatron and the LHC will ultimately reach ± 2 GeV or less, corresponding to an uncertainty in the cross section of $\pm 3\%$ at the Tevatron, and $\pm 2\%$ at the LHC.

Combining all theoretical uncertainties in quadrature, we estimate a theoretical uncertainty of about $\pm 15\%$ in the cross section at the Tevatron and the LHC, assuming an uncertainty in m_t of ± 3 GeV or less.

4.2   Calculation

In this section we optimize our study for the dominant single-top-quark production mechanism, W-gluon fusion. The final state, $Wb\bar{b}j$, consists of a recoiling light-quark jet from the production of the t-channel W boson, a $\bar{b}$ antiquark from the splitting of the initial gluon, and the decay products of the top quark. As discussed in Sec. 4.1, the large $t\bar{t}$ background requires that we use Wbj as our signal, i.e. we wish to reject events in which the $\bar{b}$ is detected above some p_{Tmax}. Thus our signal is a leptonically-decaying W boson (to reduce

QCD backgrounds) plus two jets, with one and only one b tag. In addition to the $t\bar{t}$ background, the other principal backgrounds are $Wb\bar{b}$ and Wjj (with one jet mistagged), as well as $Wc\bar{c}$ and Wcj (with one c quark mistagged). The background WZ, with $Z \to b\bar{b}$, is small and can be neglected.[4] Requiring one and only one b tag helps reduce the $t\bar{t} \to WWb\bar{b}$, $Wb\bar{b}$, and $Wc\bar{c}$ backgrounds, while maintaining almost all of the signal.

The signal and backgrounds for single-top-quark production are calculated using tree-level matrix elements generated by MadGraph [84]. The normalization of the W-gluon-fusion cross section is set by the next-to-leading-order cross section evaluated in Chapter 3, as described in Sec. 4.1. The factorization scale used for the initial gluon in Fig. 4.1(b) is $\mu^2 = p_{T\bar{b}}^2 + m_b^2$. For the light-quark $\mu^2 = Q^2$, the virtuality of the W, since this is deep-inelastic scattering. The s-channel process is also normalized to the next-to-leading-order cross section [38]. The $t\bar{t}$ cross section is normalized to the next-to-leading-order result [85, 86],[5] not including soft-gluon resummation [87–89]. The $Wb\bar{b}$, Wjj, $Wc\bar{c}$, and Wcj cross sections are calculated at leading order using the CTEQ4L [70] parton distribution functions with the renormalization and factorization scales chosen to be $\mu^2 = \hat{s}$. Since their cross sections will be directly measured by experiment, theoretical uncertainties in the normalization of these backgrounds will not limit the accuracy of the measurement of the signal cross section. The $gb \to Wt$ cross section is also calculated at leading order using CTEQ4L and $\mu^2 = \hat{s}$.

We use a Gaussian function of width $\Delta E_j/E_j = 0.80/\sqrt{E_j} \oplus 0.05$ (added in quadrature) to smear the jet energies in order to simulate the resolution of the hadron calorimeter. We do

---

[4]In contrast, WZ with $Z \to b\bar{b}$ is an important background to WH with $H \to b\bar{b}$, because M_Z is near m_H in the Higgs mass range of interest [83].

[5]We use the central values given in the last paper of Ref. [87].

Table 4.2: Cuts used to simulate the acceptance of the detector. The rapidity coverage for jets is taken to be 2.5 at the Tevatron and 4 at the LHC. The $p_{T\ell}$ threshold is greater for charged leptons which are used as triggers (in parentheses).

$\|\eta_b\| < 2$	$E_{Tb} > 20$ GeV
$\|\eta_\ell\| < 2.5$	$p_{T\ell} > 10$ GeV (20 GeV)
$\|\eta_j\| < 2.5$ (4)	$E_{Tj} > 20$ GeV
$\|\Delta R_{b\bar{b}}\| > 0.7$	$\|\Delta R_{b\ell}\| > 0.7$
$\not{E}_T > 20$ GeV	

not smear the lepton energy, since this is a small effect compared with the smearing of the jet energies. The two solutions for the neutrino momentum which satisfy the missing-p_T and W-mass constraints are reconstructed and the solution with the smallest magnitude of rapidity is chosen. This reconstructed event must pass the cuts listed in Table 4.2 used to simulate the acceptance of the detector. The rapidity and E_T coverage are chosen to simulate a generic detector. Most of the jets are central at the Tevatron, so it is only necessary to have jet coverage to $|\eta_j| < 2.5$, while the jets are distributed over a wider range of rapidities at the LHC, necessitating coverage to $|\eta_j| < 4$. Experimental results will be slightly modified depending on actual detector capabilities. We assume a b-tagging efficiency of 60% (50% at Run I) with a mistag rate of 15% for charm quarks and 0.5% for light quarks at both the Tevatron [90] and the LHC [91]. As we shall see, the large charm background suggests it may be advantageous to employ a strategy to reject charm (and light-quark) jets. Therefore we estimate how well we may do in a scenario where the mistag rate for charm quarks is reduced.

The E_T spectrum of the $\bar{b}$ antiquark, the b quark from the top decay, and the light-quark jet j from the emission of the t-channel W boson, from single-top-quark production via W-

gluon fusion, are shown in Fig. 4.2. The b-quark E_T spectrum peaks at about 60 GeV. The mean E_T of the light-quark jet is about $M_W/2 = 40$ GeV. The $\bar{b}$ antiquark is produced mostly at low p_T, and so the combination of $\bar{b}\ell^+\nu$ does not often reconstruct to a top-quark mass. Hence the majority of our signal comes from tagging the b quark, with the light quark providing the second jet.[6] However, we include in our signal *any* final state with two and only two jets with $p_T > 20$ GeV, with one and only one b tag.

4.3 Numerical results

Our results are summarized in Tables 4.3–4.5. The second column shows the total cross section times the branching ratio for the top quark to decay semileptonically. The signal cross section includes both t and $\bar{t}$ production times the branching ratio $\frac{2}{9}$ (we do not include the $t \to b\bar{\tau}\nu$ semileptonic decay in the signal since τ is seen as a jet). Similarly, the Wjj, $Wb\bar{b}$, $Wc\bar{c}$, and Wcj backgrounds account for both W^+ and W^- production times the branching ratio $\frac{2}{9}$. The $t\bar{t}$ background is multiplied by the branching ratio $\frac{4}{9}$ to include the possibility that either the t or the $\bar{t}$ decays semileptonically (a $t\bar{t}$ event can be a background to either single t or single $\bar{t}$ production).

The third column of Tables 4.3–4.5 shows the cross section for events which pass the detector acceptance cuts listed in Table 4.2. These events have one and only one b-tagged jet, and at least one other jet. We have used a b-tagging efficiency of 60% (50% in Table 4.3), with a mistag rate of 15% for charm and 0.5% for light-quark jets [90, 91]. The detector response is primarily important in reducing the Wjj, $Wb\bar{b}$, $Wc\bar{c}$, and Wcj backgrounds. The numbers in parentheses are the cross sections for events which have a reconstructed $b\ell^+\nu$

---

[6]After the veto cut and top-quark mass reconstruction described in Sec. 4.2, this is 94% of the signal at the Tevatron, and 93% of the signal at the LHC.

Table 4.3: Cross sections (fb) for single-top-quark production and a variety of background processes at Run I of the Fermilab Tevatron. The W-gluon-fusion signal is denoted by $t\bar{b}j$, and the s-channel by $t\bar{b}$. Listed in parenthesis are the cross sections for events in which the reconstructed $b\ell^{+}\nu$ invariant mass is within $\pm 20\,\mathrm{GeV}$ of the top-quark mass. The bottom two rows show the statistical sensitivity for discovery and a cross section measurement, respectively, given $110\,\mathrm{pb}^{-1}$ of data.

	Tevatron	1.8 TeV $p\bar{p}$	
	Total$\times$ BR	Detector (peak)	Veto (peak)
$t\bar{b}j$	378	79 (54)	64 (46)
$t\bar{b}$	162	40 (20)	40 (20)
Wt	16	8.3 (4.2)	1.9 (1.0)
Wjj	—	205 (40)	205 (40)
$Wb\bar{b}$	6500	128 (24)	128 (24)
$Wc\bar{c}$	—	65 (12)	65 (12)
Wcj	—	195 (37)	195 (37)
$t\bar{t}$	2160	606 (268)	53 (15)
$\frac{S}{\sqrt{B}}$	—	1.3	2.0
$\frac{\sqrt{S+B}}{S}$	—	0.81	0.63

76

Table 4.4: Cross sections (fb) for single-top-quark production and a variety of background processes at Run II of the Fermilab Tevatron. The W-gluon-fusion signal is denoted by $t\bar{b}j$, and the s-channel by $t\bar{b}$. Listed in parenthesis are the cross sections for events in which the reconstructed $b\ell^+\nu$ invariant mass is within $\pm 20\,\mathrm{GeV}$ of the top-quark mass. The bottom two rows show the statistical sensitivity for discovery and a cross section measurement, respectively, given 1 fb^{-1} of data.

| | Tevatron | 2 TeV $p\bar{p}$ | |
	Total$\times$ BR	Detector (peak)	Veto (peak)
$t\bar{b}j$	542	133 (90)	107 (76)
$t\bar{b}$	196	48 (24)	48 (24)
Wt	26.5	16.6 (8.4)	3.8 (2.1)
Wjj	—	257 (54)	257 (54)
$Wb\bar{b}$	7420	146 (28)	146 (28)
$Wc\bar{c}$	—	74 (14)	74 (14)
Wcj	—	274 (53)	274 (53)
$t\bar{t}$	2980	838 (364)	80 (24)
$\frac{S}{\sqrt{B}}$	—	5.4	7.8
$\frac{\sqrt{S+B}}{S}$	—	0.21	0.16

77

Table 4.5: Cross sections (fb) for single-top-quark production and a variety of background processes at the CERN LHC. The W-gluon-fusion signal is denoted by $t\bar{b}j$, and the s-channel by $t\bar{b}$. Listed in parenthesis are the cross sections for events in which the reconstructed $b\ell^+\nu$ invariant mass is within ± 20 GeV of the top-quark mass. The bottom two rows show the statistical sensitivity for discovery and a cross section measurement, respectively, given 1 fb^{-1} of data.

	LHC	14 TeV pp	
	Total$\times$ BR	Detector (peak)	Veto (peak)
$t\bar{b}j$	54400	12500 (7510)	8930 (6110)
$t\bar{b}$	2270	470 (229)	470 (229)
Wt	13700	7510 (3610)	1650 (820)
Wjj	—	7000 (1460)	7000 (1460)
$Wb\bar{b}$	70700	1140 (230)	1140 (230)
$Wc\bar{c}$	—	750 (150)	750 (150)
Wcj	—	24200 (5070)	24200 (5070)
$t\bar{t}$	357000	95600 (40700)	9040 (2770)
$\frac{S}{\sqrt{B}}$	—	52	73
$\frac{\sqrt{S+B}}{S}$	—	0.021	0.018

invariant mass within 20 GeV of the top-quark mass (to account for detector resolution). Note that 70% of the single-top-quark events survive this cut, while only 43% of the $t\bar{t}$ events survive, and only 20% of the Wjj, $Wb\bar{b}$, $Wc\bar{c}$, and Wcj events survive. The low acceptance for Wjj, $Wb\bar{b}$, $Wc\bar{c}$, and Wcj is easily understood since there is no kinematic preference towards the top-quark mass. The $t\bar{t}$ acceptance is only 43% because one half of the time the tagged b quark will be associated with the other top quark in the event and thus has no preference to reconstruct to the mass of the top quark.

It is evident from Tables 4.3–4.5 that the largest background is $t\bar{t} \rightarrow W^+W^-b\bar{b}$, and it is much larger than the signal. This background is particularly worrisome because it produces a peak in the $b\ell^+\nu$ invariant-mass spectrum at the top-quark mass, as does the signal.[7] Hence it is important to apply additional cuts to reduce this background. Since this background has an additional W boson in the final state, we reject events which have an additional charged lepton with $p_{T\ell} > 10$ GeV, or additional jets[8] with $E_{Tj} > 20$ GeV and $|\eta_j| < 2.5$ at the Tevatron[9] ($|\eta_j| < 4$ at the LHC). This reduces the $t\bar{t}$ background by more than a factor of 15, while reducing the signal by a modest amount, since the signal rarely has a third jet with $E_{Tj} > 20$ GeV. This "veto" yields the signal and background cross sections listed in the fourth column of Tables 4.3–4.5.

We show in Figs. 4.3, 4.4 the $b\ell^+\nu$ invariant-mass distribution for single-top-quark production and the various visible backgrounds after the veto. The W-gluon-fusion process is prominent at both the Tevatron and the LHC, but the backgrounds are non-negligible. The

---

[7]In contrast, the $t\bar{t}$ background is not as problematic for the process WH with $H \rightarrow b\bar{b}$, because it does not produce a peak in the $b\bar{b}$ invariant mass near the Higgs mass [83].

[8]The τ lepton is treated as a jet.

[9]Since jets from the backgrounds are typically central, increasing the jet rapidity coverage to $|\eta_j| < 4$ at the Tevatron does not decrease the backgrounds significantly.
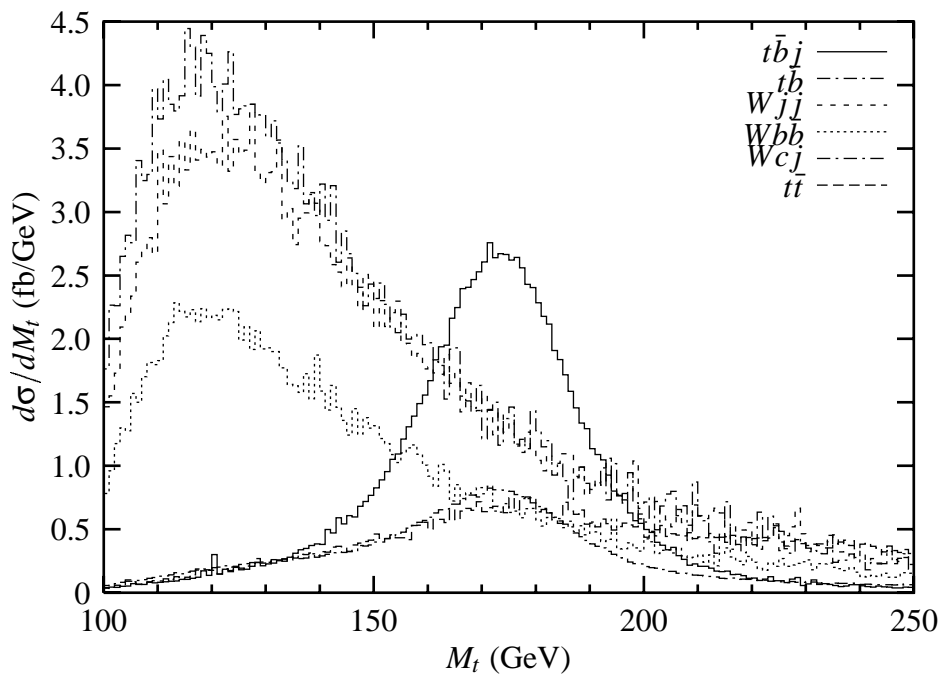
Figure 4.3: The $b\ell^+\nu$ invariant-mass distribution for single-top-quark production and backgrounds at the Run II of the Fermilab Tevatron. The W-gluon-fusion signal is denoted by $t\bar{b}j$, and the s-channel by $t\bar{b}$.
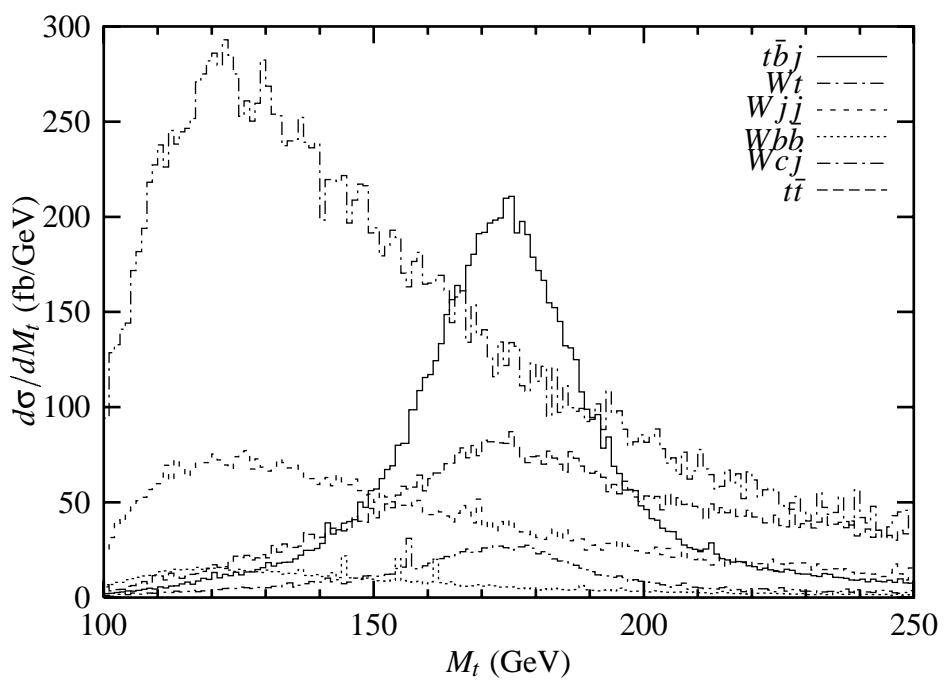
Figure 4.4: The $b\ell^+\nu$ invariant-mass distribution for single-top-quark production and backgrounds at the CERN LHC. The W-gluon-fusion signal is denoted by $t\bar{b}j$.

81

$t\bar{t}$ background has been reduced to an acceptable level, but it is still significant, and because it has the same shape as the signal it will be necessary to calibrate this background by measuring it with looser cuts and then extrapolating it to the present cuts with the help of simulations. If we desire to separate single-top-quark production via W-gluon fusion from the s-channel process, it will also be necessary to measure the latter and subtract it from the signal. This can be achieved by double b-tagging [58]. However, for an analysis of V_{tb} at the Tevatron we want to use all single-top-quark data. This is unnecessary at the LHC, where the s-channel process is negligible.

The remaining backgrounds — $Wb\bar{b}$, Wjj, $Wc\bar{c}$, and Wcj — all yield continuous spectra, and therefore can be calibrated by measuring them in the invariant-mass regions away from the peak region. These backgrounds are significant and comparable to each other at the Tevatron, but only Wcj is significant at the LHC. It may be desirable to reject more strongly events in which a charm or light quark fakes a b jet, both at the Tevatron and the LHC. This can be achieved by imposing the condition that the invariant mass of the system which points to the secondary vertex exceed 2 GeV [92]. The VXD3 vertex detector in SLD has achieved a b-tagging efficiency of 50%, with a mistag rate of 1.24% from charm and 0.07% from light quarks. We use these mistag rates to estimate what might be achieved with the vertex detectors at the Tevatron and LHC detectors.

The statistics for discovering a signal are different from those for measuring its cross section. To claim a discovery, one needs to demonstrate that the signal is not consistent with a fluctuation in the background. The discovery significance is therefore governed by the number of signal events divided by the square root of the number of background events $\frac{S}{\sqrt{B}}$. Reducing the background can provide substantial improvement on the significance for dis-
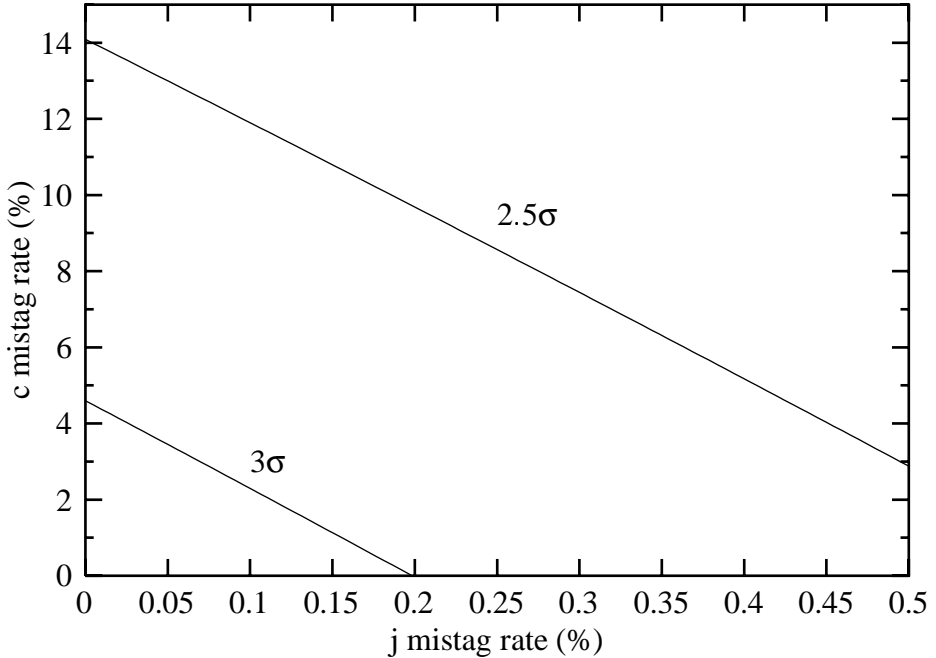
Figure 4.5: Required mistag rates for charm and the light-quark jets j in order to reach a discovery significance of 2.5σ, or 3σ with data from Run I of the Fermilab Tevatron.

covery. In the next-to-last row of Tables 4.3–4.5, we present the significance for discovery

of single-top-quark production (all modes) for Run I at the Tevatron, and for the first fb^{-1} at

Run II and the LHC. Even though there were about 7–8 events in the top-quark mass-peak

region at Run I, the significance is only 2σ. If a discovery of single-top-quark production is

to be made from Run I data, the charm and light-quark-jet j mistag rates must be reduced.

In Fig. 4.5 we show 2.5σ, and 3σ discovery curves as functions of the rate to mistag charm

and light-quark jets, assuming a b-tagging of 50%. At Run II single-top-quark production

will be discovered at the 5σ level in the first 410 pb^{-1} of data, and at the LHC in the first

5 pb^{-1}.

The last row of Tables 4.3–4.5 shows the statistical sensitivity for measurement of the

total single-top-quark production cross section compared to the backgrounds. This corresponds to measuring the total single b-tagged single-top-quark cross section. This provides the best statistical result for extracting V_{tb}. Run II of the Tevatron will provide a measurement of the cross section with a statistical uncertainty of $\pm 11\%$ (with $2\,\mathrm{fb}^{-1}$ of data) which combined in quadrature with the theoretical uncertainty of $\pm 15\%$ from the W-gluon fusion NLO calculation gives a total estimated uncertainty of $\pm 19\%$. Systematic uncertainties such as the total luminosity are estimated to be on the order of 5%. Furthermore, these uncertainties will tend to cancel in the ratio of single-top-quark production over $t\bar{t}$ production. Since this ratio is proportional to $|V_{tb}|^2$, the error on V_{tb} will be reduced by a factor of two, resulting in a measurement of $\pm 10\%$ with $2\,\mathrm{fb}^{-1}$ of data at Run II. If VXD3 mistag rates can be achieved [92], the statistical uncertainty on single-top-quark production improves to $\pm 9\%$ with $2\,\mathrm{fb}^{-1}$ of data at Run II. The LHC will have ~ 100 times the number of events per fb^{-1} as Run II, which means V_{tb} can be extracted as accurately as theoretical and systematic effects can be controlled. Since many of the systematic effects cancel in the ratio, theory will need to provide higher order corrections to both single-top-quark production and $t\bar{t}$ production.

Because new physics may affect the s-channel, and t-channel modes of single-top-quark production independently, we also wish to know how well the t-channel cross section can be measured separately. At Run II, the W-gluon-fusion cross section can be measured to $\pm 15\%(stat)$ with $2\,\mathrm{fb}^{-1}$ of data [$\pm 12\%(stat)$ with VXD3 efficiencies]. After including theoretical and estimated systematic errors as above, we estimate the cross section will be measured to $\pm 22\%$ (with VXD3 rates, $\pm 20\%$). A measurement of V_{tb} from this calculation will be made to $\pm 11\%$. At the LHC, again the theoretical uncertainties determine how well the

cross section can be measured.

The relatively simple set of cuts in Table 4.2 provides us with a measurement of the W-gluon-fusion cross section within 60% of the theoretical limit (100% signal acceptance with 100% background rejection) at both machines. We therefore restrain ourselves from optimizing our cuts without including a more realistic simulation of detector and hadronization effects. However, we would like to remind the reader that another unique feature of single-top-quark production is the forward jet associated with the production of the t-channel W boson [73, 93]. Fig. 4.6 shows the rapidity η of the identified jet for W-gluon fusion, compared with the rapidity of jets in the background processes at the Tevatron.

The $t\bar{t}$ background naturally has several additional jets associated with the decay of the second top quark. Although each of these decay products tends to be central, it is sufficient for any one of the three jets to be forward which reduces the discriminating power of this cut on the $t\bar{t}$ background. Additionally, while the forward jet peaks at a rapidity $\eta = 1.8$ at the Tevatron, one-third of the W-gluon-fusion cross section is at $\eta < 1$. Hence even a weak forward tag $\eta_j > 1$ does not improve the significance for measurement or discovery. The situation at the LHC is shown in Fig. 4.7. The forward jet peaks at $\eta = 2.5$, and only 20% of the W-gluon signal is at $\eta < 1$. However, all of the backgrounds also spread out in rapidity. Thus it remains difficult to make any significant gain by tagging the forward jet. A forward jet tag should be considered when determining a set of fully-optimized experimental cuts, but it is unlikely to provide more than a small improvement to the what is achieved above.

4.4   Measuring the top-quark polarization

Single-top-quark production proceeds via the electroweak interaction, therefore, the top
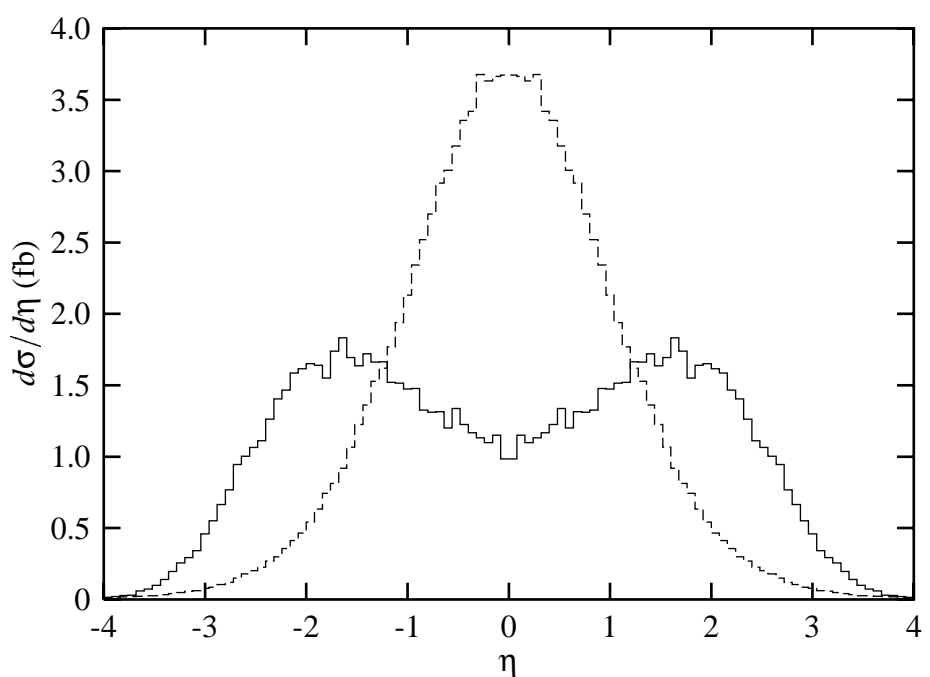
Figure 4.6: Rapidity distributions for the identified jet j in W-gluon fusion (solid line) and background events (dashed line) at the Fermilab Tevatron.
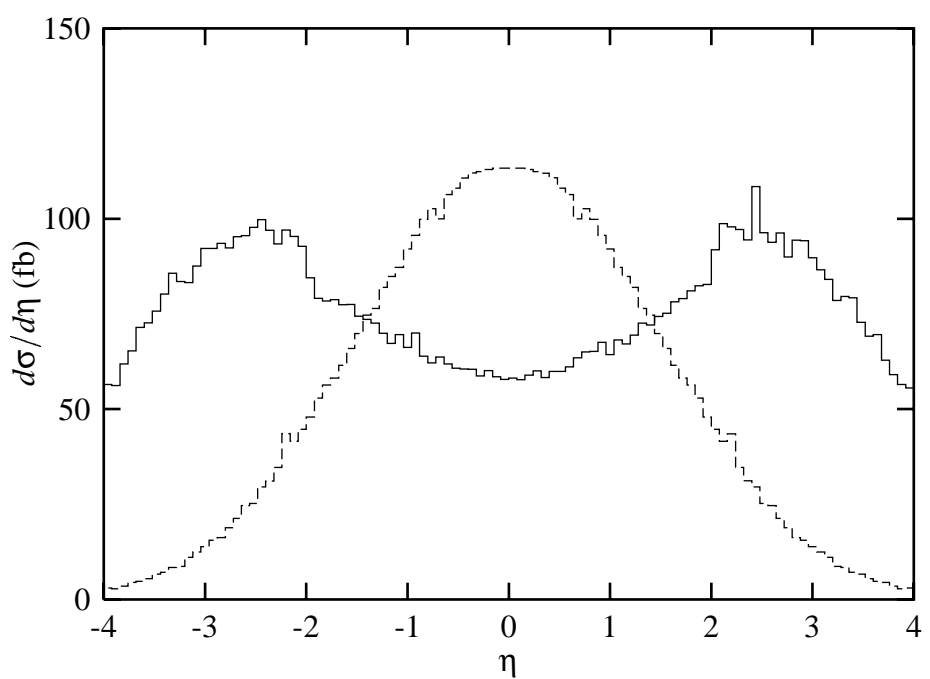
Figure 4.7: Rapidity distributions for the identified jet j in W-gluon fusion (solid line) and background events (dashed line) at the CERN LHC.

quarks produced are highly polarized in the direction of the spectator quark in the event [39]. Since the top quark decays before QCD interactions can flip the spin [40],[10] the polarization of the top quark may be observable in the distribution of its decay products. For semileptonic top-quark decays, the lepton is particularly sensitive to the spin of the top quark.

$$\frac{1}{\sigma}\frac{d\sigma}{d[\cos(\theta_{j\ell+})]} = \frac{1}{2}[1 + \cos(\theta_{j\ell+})] \,. \qquad (4.2)$$

Here, $\theta_{j\ell+}$ is the angle in the top-quark rest frame, between the spin direction of the top quark, and the direction of the lepton [41].

Fig. 4.8 shows the normalized distribution versus $\cos(\theta_{j\ell+})$ for W-gluon fusion, where $\theta_{j\ell+}$ is the angle of the lepton in the top-quark rest frame with respect to the direction of the spectator jet j (identified as in Sec. 4.2). There are four different initial state configurations for W-gluon fusion; $u + g$, $g + u$, $\bar{d} + g$ and $g + \bar{d}$. At the Tevatron, the dominant initial state is ug, providing 3/4 of the cross section. Single-top-quarks are 100% polarized in the direction of the d-type quark in the event. In events where the d-type quark is the initial quark, the angle between this quark and the spectator jet is relatively small. Therefore using the spectator jet as the direction is very efficient. Similarly, for s-channel single-top-quark production, the direction of the $\bar{b}$ is correlated with the initial state $\bar{d}$ antiquark. The dashed line in Fig. 4.8 shows the distribution versus $\cos(\theta_{j\ell+})$ after the detector acceptance, jet smearing, and reconstruction of the neutrino's momentum are taken in to account, and the top-quark mass peak reconstructed. The suppression at $\cos(\theta_{j\ell+}) \simeq 1$ is due to the δR cut between the lepton and the spectator jet. The dotted line shows this same distribution including the veto cuts.

---

[10]The revolution time $T \sim 1/(\mu\alpha_s^2)$ for a bound state is less than the lifetime of the top quark $\tau \sim 1/1.5\,\mathrm{GeV}$. For a detailed calculation using potential models and heavy-quark effective theory see Ref. [94].
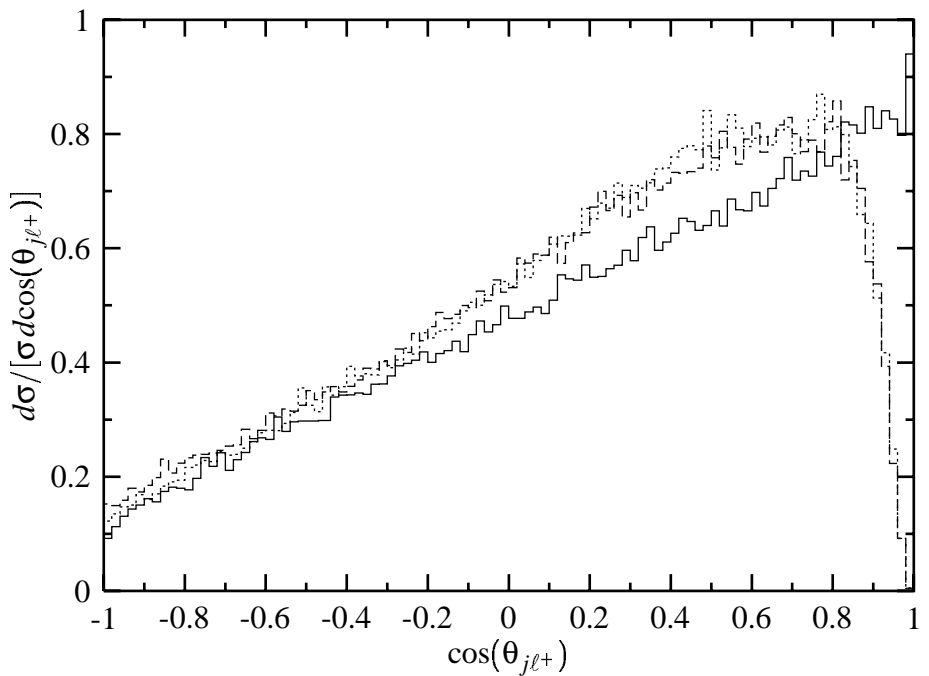
Figure 4.8: Normalized distributions of reconstructed top-quark-mass events versus $\cos(\theta_{j\ell+})$, where $\theta_{j\ell+}$ is the angle between the decay lepton, and the spectator jet in the top-quark rest frame for W-gluon fusion. The solid line shows events without any cuts. Events which pass the detector cuts are shown with a dashed line. The dotted line shows events which pass the veto.
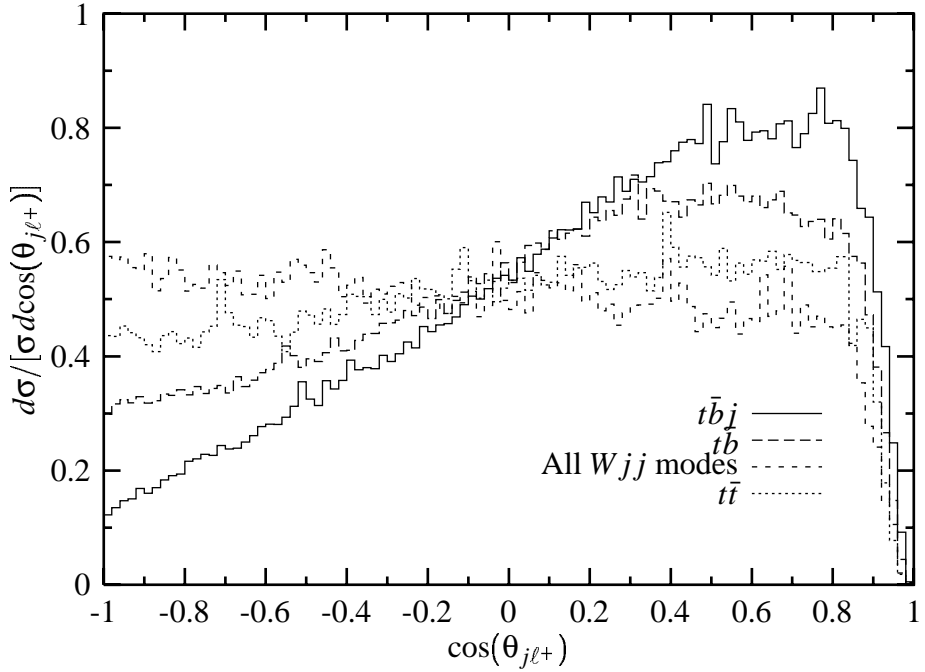
Figure 4.9: Normalized distributions of W-gluon fusion, s-channel production, and backgrounds versus $\cos(\theta_{j\ell+})$, where $\theta_{j\ell+}$ is the angle between the decay lepton, and the spectator jet in the top-quark rest frame. These plots are for reconstructed top-quark-mass events which pass the cuts listed in Table 4.2 in addition to the jet veto.

In Fig. 4.9 we show the normalized distribution versus $\cos(\theta_{j\ell+})$ after the veto cuts, and top-mass reconstruction, for W-gluon fusion, s-channel production, and the backgrounds. A simple test to observe the top-quark spin polarization is to measure the asymmetry in this plot. Since jet reconstruction cuts off the small angle region, we define an asymmetry between $-1.0 < \cos(\theta_{j\ell+}) < 0.8$,

$$A \equiv \frac{N[\cos(\theta_{j\ell+}) < -0.1] - N[-0.1 < \cos(\theta_{j\ell+}) < 0.8]}{N[\cos(\theta_{j\ell+}) < -0.1] + N[-0.1 < \cos(\theta_{j\ell+}) < 0.8]} . \qquad (4.3)$$

The standard model predicts an asymmetry of -40% for W-gluon fusion, and -23.5% for s-channel single-top-quark production, from the reconstructed events after cuts. This

90

gives a total single-top-quark asymmetry of -36%. An unpolarized top quark would have a zero asymmetry. A nonzero asymmetry measurement would therefore be observation of the polarization of the top-quark in single-top-quark production. There is a slight positive bias evident in the $t\bar{t}$ background events in Fig. 4.9 due to the jet reconstruction algorithm. The total background, $t\bar{t}$ plus the various Wjj backgrounds, however, is nearly flat in $\cos(\theta_{j\ell+})$, with an asymmetry of less than $+4\%$. If we treat the background as flat, the measured asymmetry is $A_{Measured} = -13\%$. This can be observed at the 3σ level with 2 fb^{-1} of data. An observation of nonzero asymmetry at the 5σ level requires $\simeq 525$ single-top-quark events with a background of $\simeq 910$ unpolarized events. This would require approximately 5.3 fb^{-1} of luminosity.

The accuracy with which the top-quark polarization can be extracted from this asymmetry is limited both by the statistical uncertainty in the asymmetry measurement, as well as uncertainty in the ratio of the total number of events N_{Total} to the number of single-top-quark events N_t. The extracted asymmetry A_t is:

$$A_t = A_{Measured} \times \left(N_{Total}/N_t \right) . \tag{4.4}$$

The fractional uncertainty is obtained by adding the fractional uncertainty of $A_{Measured}$, and N_{Total}/N_t in quadrature. Given 2 fb^{-1} of luminosity at Run II the experiments should be able to measure an asymmetry of $A_t = -36 \pm 9\%$, giving the polarization to $\pm 25\%$. The large statistical uncertainty $\pm 9\%$ will be greatly improved at the LHC. Assuming the same asymmetry at the LHC, with 2 fb^{-1} of data the statistical uncertainty will be reduced to $\pm 3\%$, allowing the top-quark polarization to be measured to $\pm 8\%$.

4.5   Conclusions

Single-top-quark production will be an important tool for studying the Wtb vertex. The W-gluon fusion channel offers large statistics, and therefore the possibility to study the vertex with high precision. We have outlined a set of discovery cuts which may provide evidence for single-top-quark production in the data from Run I at the Fermilab Tevatron, provided the rates for charm and light-quark jets to be misidentified as b quarks can be controlled. In Run II, single-top-quark production, and W-gluon fusion specifically, will be observed. The W-gluon-fusion cross section can be measured to $\pm 22\%$ or better with 2 fb^{-1} of data, from which V_{tb} can be extracted to $\pm 11\%$ if it is close to unity. This is comparable with the $\pm 12\%$ measurement possible with a double b-tagging analysis optimized to find s-channel production [58]. Combining these independent measurements, V_{tb} may be measured to $\pm 8\%$. Using the full single-top-quark cross section in this analysis, V_{tb} can be measured to $\pm 10\%$.

Run II may also provide an opportunity to observe the $V - A$ nature of the Wtb vertex by observing the distribution of the lepton from the semileptonic decay of the top quark. With 2 fb^{-1} of data, the polarization of the top quark can be seen at the 3σ level. A measurement of the polarization can be made to $\pm 25\%$.

Unlike s-channel single-top-quark production, the W-gluon-fusion cross section grows rapidly with collider energy. The CERN LHC will provide a measurement of the cross section accurate to 2%(*stat*) with the first fb^{-1} of data. In principle this will allow for detailed studies of the Wtb vertex, provided systematic uncertainties can be controlled.

We describe an improved method for measuring single-top-quark production via W-

gluon fusion at hadron colliders. With simple cuts, the cross section can be measured to within a factor of 1.6 of the maximum statistical sensitivity. This study looks for only two jets, with one and only one b tag, and a W that decays leptonically. It also incorporates the correct method for scaling the differential W-gluon cross section to the full NLO result. Because perturbation theory breaks down in the region of where $\bar{b}$ antiquarks are collinear with the b quarks, we avoid results that are sensitive to the distribution of the $\bar{b}$ at low transverse momenta. Our choice of signal, Wbj, integrates over much of the problem region. Thus the uncertainty from this effect is reduced from 30% to 10%.

If we wish to obtain smaller errors for the Run II data, or reach high sensitivities at the LHC, there are a few theoretical issues that need to be resolved. While it is possible to reduce the uncertainty due to the collinear region by raising the E_T cuts to 40 GeV, the huge $t\bar{t}$ background returns since the extra jets escape detection. Hence, a full NLO cross section that is differential in the p_T spectrum of the $\bar{b}$ antiquark needs to be calculated. The other main uncertainty is due to the parton distribution function for the gluon. Hopefully, this will become more constrained when data from the relevant region of x and Q^2, is incorporated.

Appendix A

Supersymetric QCD form factors

The form factors for the one-loop matrix elements in Eq. 2.7 of the supersymmetric QCD correction to top-quark production are given below. The integrals are written in terms of n-point integrals [49], in the notation of FF [50]. The code used to evaluate the tensor integrals is listed in Appendix B. For each appearance of a heavy squark $\widetilde{q}$, or top squark $\widetilde{t}$, the term should be summed with $\widetilde{q}_1$ or $\widetilde{t}_1$ first, and then $\pm\widetilde{q}_2$ or $\pm\widetilde{t}_2$ as indicated. The vacuum polarization is separated into terms proportional to the top squarks $\widetilde{t}$ and the heavy squarks $\widetilde{q}$. With $\Delta = 1/\varepsilon - \gamma_E + \ln 4\pi$,

$$
\begin{aligned}
\Pi \;=\; & \frac{1}{s}\Big[(4m_{\widetilde{g}}^2 + 2s)B_0(m_{\widetilde{g}}^2, m_{\widetilde{g}}^2, s) - 4A_0(m_{\widetilde{g}}^2) + \frac{2}{3}[A_0(m_{\widetilde{t}}^2) + 5A_0(m_{\widetilde{q}}^2)] \\
& + \frac{1}{6}(s - 4m_{\widetilde{t}}^2)B_0(m_{\widetilde{t}}^2, m_{\widetilde{t}}^2, s) + \frac{5}{6}(s - 4m_{\widetilde{q}}^2)B_0(m_{\widetilde{q}}^2, m_{\widetilde{q}}^2, s) \\
& - 4s\Delta + 4m_{\widetilde{g}}^2 + \frac{2}{3}(s - m_{\widetilde{t}}^2 - 5m_{\widetilde{q}}^2)\Big] \; .
\end{aligned}
\tag{A.1}
$$

The initial- and final-state vertex correction form factors have the same functional form. For the initial state, $m_q = 0$, and $m_{\widetilde{Q}} = m_{\widetilde{q}}$. For the final state, $m_q = m_t$, and $m_{\widetilde{Q}} = m_{\widetilde{t}}$. The two squarks $\widetilde{Q}_1$ and $\pm\widetilde{Q}_2$ are summed as before. Arbitrary mixing is allowed for both the

top squarks and the heavy squarks. The three-point integrals have the form

$$C(m_1^2, m_2^2, m_3^2) = C(m_1^2, m_2^2, m_3^2, m_{\tilde{q}}^2, m_{\tilde{q}}^2, s) \, , \tag{A.2}$$

$$
\begin{aligned}
V = & -\frac{3}{2} \Big[m_q^2 C_{21}(m_{\tilde{g}}^2, m_{\tilde{Q}}^2, m_{\tilde{g}}^2) + m_q^2 C_{22}(m_{\tilde{g}}^2, m_{\tilde{Q}}^2, m_{\tilde{g}}^2) + (s - 2m_q^2) C_{23}(m_{\tilde{g}}^2, m_{\tilde{Q}}^2, m_{\tilde{g}}^2) \\
& + 2 C_{24}(m_{\tilde{g}}^2, m_{\tilde{Q}}^2, m_{\tilde{g}}^2) - 1 + 2 m_q^2 C_{11}(m_{\tilde{g}}^2, m_{\tilde{Q}}^2, m_{\tilde{g}}^2) + (s - 2 m_q^2) C_{12}(m_{\tilde{g}}^2, m_{\tilde{Q}}^2, m_{\tilde{g}}^2) \\
& - m_{\tilde{g}}^2 C_0(m_{\tilde{g}}^2, m_{\tilde{Q}}^2, m_{\tilde{g}}^2) \pm 2 m_q m_{\tilde{g}} \sin(2\theta_{\tilde{Q}}) C_0(m_{\tilde{g}}^2, m_{\tilde{Q}}^2, m_{\tilde{g}}^2) \Big] + \frac{1}{3} C_{24}(m_{\tilde{Q}}^2, m_{\tilde{g}}^2, m_{\tilde{Q}}^2) \\
& + \frac{4}{3} \Big[-B_1(m_{\tilde{Q}}^2, m_{\tilde{g}}^2, m_q^2) + (m_q^2 + m_{\tilde{g}}^2 - m_{\tilde{Q}}^2) B_0'(m_{\tilde{Q}}^2, m_{\tilde{g}}^2, m_q^2) \\
& \mp 2 m_q m_{\tilde{g}} \sin(2\theta_{\tilde{Q}}) B_0'(m_{\tilde{Q}}^2, m_{\tilde{g}}^2, m_q^2) \Big] \, ,
\end{aligned}
\tag{A.3}
$$

$$
\begin{aligned}
S = & \, 3 \Big[m_q^2 C_{22}(m_{\tilde{g}}^2, m_{\tilde{Q}}^2, m_{\tilde{g}}^2) - m_q^2 C_{23}(m_{\tilde{g}}^2, m_{\tilde{Q}}^2, m_{\tilde{g}}^2) \mp m_q m_{\tilde{g}} \sin(2\theta_{\tilde{Q}}) C_{12}(m_{\tilde{g}}^2, m_{\tilde{Q}}^2, m_{\tilde{g}}^2) \Big] \\
& - \frac{1}{3} \Big[-m_q^2 C_{22}(m_{\tilde{Q}}^2, m_{\tilde{g}}^2, m_{\tilde{Q}}^2) + m_q^2 C_{23}(m_{\tilde{Q}}^2, m_{\tilde{g}}^2, m_{\tilde{Q}}^2) \\
& \mp m_q m_{\tilde{g}} \sin(2\theta_{\tilde{Q}}) [C_{12}(m_{\tilde{Q}}^2, m_{\tilde{g}}^2, m_{\tilde{Q}}^2) + \frac{1}{2} C_0(m_{\tilde{Q}}^2, m_{\tilde{g}}^2, m_{\tilde{Q}}^2)] \Big] \, ,
\end{aligned}
\tag{A.4}
$$

$$
\begin{aligned}
A = & \pm \frac{3}{2s} \cos(2\theta_{\tilde{Q}}) \Big[m_q^2 C_{21}(m_{\tilde{g}}^2, m_{\tilde{Q}}^2, m_{\tilde{g}}^2) + m_q^2 C_{22}(m_{\tilde{g}}^2, m_{\tilde{Q}}^2, m_{\tilde{g}}^2) \\
& + (s - 2 m_q^2) C_{23}(m_{\tilde{g}}^2, m_{\tilde{Q}}^2, m_{\tilde{g}}^2) + 2 C_{24}(m_{\tilde{g}}^2, m_{\tilde{Q}}^2, m_{\tilde{g}}^2) + s C_{12}(m_{\tilde{g}}^2, m_{\tilde{Q}}^2, m_{\tilde{g}}^2) \\
& - m_{\tilde{g}}^2 C_0(m_{\tilde{g}}^2, m_{\tilde{Q}}^2, m_{\tilde{g}}^2) - \frac{2}{9} C_{24}(m_{\tilde{Q}}^2, m_{\tilde{g}}^2, m_{\tilde{Q}}^2) + \frac{8}{9} B_1(m_{\tilde{Q}}^2, m_{\tilde{g}}^2, m_q^2) \Big] \, .
\end{aligned}
\tag{A.5}
$$

The four-point integrals in the box terms are

$$D = D(m_{\tilde{g}}^2, m_{\tilde{q}}^2, m_{\tilde{g}}^2, m_{\tilde{t}}^2, 0, 0, m_t^2, m_t^2, s, m_t^2 - 2 p_1 \cdot p_3) \, , \tag{A.6}$$

$$D^c = D^c(m_{\tilde{g}}^2, m_{\tilde{q}}^2, m_{\tilde{g}}^2, m_{\tilde{t}}^2, 0, 0, m_t^2, m_t^2, s, m_t^2 - 2 p_2 \cdot p_3) \, ,$$

where $p_1 \cdot p_3 = s(1 - \beta z)/4$ and $p_2 \cdot p_3 = s(1 + \beta z)/4$. The box and crossed-box terms are summed over each combination of squarks $\tilde{q}_i \tilde{t}_j$, where $i, j = 1, 2$. The mixing of the squarks

95

is parameterized as

$$ac + bd = \mp \frac{1}{4} \sin(2\theta_{\tilde{t}}) \,, \tag{A.7}$$

for $\tilde{t}_1$ and $\tilde{t}_2$ respectively, and, for $\tilde{q}_i \tilde{t}_j$,

$$\begin{aligned}
a^2 + b^2 &= \frac{1}{4}[\cos^2(\theta_{\tilde{t}} - \theta_{\tilde{q}}) + \cos^2(\theta_{\tilde{t}} + \theta_{\tilde{q}})] \,, i = j \,, \tag{A.8} \\
c^2 + d^2 &= \frac{1}{4}[\sin^2(\theta_{\tilde{t}} - \theta_{\tilde{q}}) + \sin^2(\theta_{\tilde{t}} + \theta_{\tilde{q}})] \,, i = j \,, \\
a^2 + b^2 &= \frac{1}{4}[\sin^2(\theta_{\tilde{t}} - \theta_{\tilde{q}}) + \sin^2(\theta_{\tilde{t}} + \theta_{\tilde{q}})] \,, i \neq j \,, \\
c^2 + d^2 &= \frac{1}{4}[\cos^2(\theta_{\tilde{t}} - \theta_{\tilde{q}}) + \cos^2(\theta_{\tilde{t}} + \theta_{\tilde{q}})] \,, i \neq j \,.
\end{aligned}$$

$$\begin{aligned}
B = {} & m_t m_{\tilde{g}} s^2 (ac + bd)[D_{11} - D_{12} + D_{13} + D_0] + m_t^2 s^2 (a^2 + b^2)[-D_{12} - D_{23} - D_{24} \\
& + D_{26} - 2D_{27}/s] + 4s(p_2 \cdot p_3)^2 (a^2 + b^2)[-D_{12} + D_{13} - D_{24} + D_{25} - 2D_{27}/s] \\
& + [m_t^2 s + 4(p_1 \cdot p_3)^2][m_t^2 (a^2 + b^2)D_{23} + m_{\tilde{g}}^2 (c^2 + d^2)D_0 - 2m_t m_{\tilde{g}}(ac + bd)D_{13}] \,,
\end{aligned}$$

$$(A.9)$$

$$\begin{aligned}
C = {} & m_t m_{\tilde{g}} s^2 (ac + bd)[D_{11}^c - D_{12}^c + D_{13}^c + D_0^c] + m_t^2 s^2 (c^2 + d^2)[-D_{12}^c - D_{23}^c - D_{24}^c \\
& + D_{26}^c - 2D_{27}^c/s] + 4s(p_1 \cdot p_3)^2 (c^2 + d^2)[-D_{12}^c + D_{13}^c - D_{24}^c + D_{25}^c - 2D_{27}^c/s] \\
& + [m_t^2 s + 4(p_2 \cdot p_3)^2][m_t^2 (c^2 + d^2)D_{23}^c + m_{\tilde{g}}^2 (a^2 + b^2)D_0^c - 2m_t m_{\tilde{g}}(ac + bd)D_{13}^c] \,.
\end{aligned}$$

$$(A.10)$$

A few equations in the appendix of Ref. [46] appear to be misprinted. As written they lead to divergent behavior that does not match Fig. 8 in that paper. With the following replacements, our analytic results agree up to the sign discrepency discussed in Sec. 2.1.

$$\begin{aligned}
F_{12}^{\text{DB}} &= \frac{\alpha_s}{\pi} \{ -\hat{s}(2A_5^{\dagger}A_5^{\dagger})[2\hat{s}m_t^2 + 2(\hat{u} - m_t^2)^2] - m_{\tilde{g}}m_t(2A_5^{\dagger}A_{5x})[2\hat{s}^2] \} D_{12} \\
F_{13}^{\text{DB}} &= \frac{\alpha_s}{\pi} \{ \hat{s}(2A_5^{\dagger}A_5^{\dagger})[2(\hat{u} - m_t^2)^2] + m_{\tilde{g}}m_t(2A_5^{\dagger}A_{5x})[2\hat{s}(\hat{s} - 2m_t^2) - 4(\hat{t} - m_t^2)^2] \} D_{13}
\end{aligned}$$

$$F_{12}^{\text{CB}} = \frac{\alpha_s}{\pi}\{-\hat{s}(2A_5^\dagger A_5^\dagger)[2\hat{s}m_t^2 + 2(\hat{t} - m_t^2)^2] - m_{\tilde{g}}m_t(2\overline{A_5^\dagger A_{5x}})[2\hat{s}^2]\}D_{12}$$

$$F_{13}^{\text{CB}} = \frac{\alpha_s}{\pi}\{\hat{s}(2A_5^\dagger A_5^\dagger)[2(\hat{t} - m_t^2)^2] + m_{\tilde{g}}m_t(2\overline{A_5^\dagger A_{5x}})[2\hat{s}(\hat{s} - 2m_t^2) - 4(\hat{u} - m_t^2)^2]\}D_{13}$$

Appendix B

Numerical evaluation of tensor loop integrals

This appendix reproduces the Fortran subroutines in the file `zffbcd.f`. These subroutines extend the package FF [50] (which numerically evaluates scalar n-point integrals) to allow for numerical evaluation of n-point tensor integrals up through $n = 4$ and rank 2. The notation used in the subroutines is identical to that of FF, except where noted.

The tensor n-point integrals are analytically reduced to sets of scalar n-point integrals before numerical evaluation. The routines are based on the work of Passarino and Veltman in Ref. [49] with a few modifications:

1. In order to be consistent with FF, the functions are evaluated in the Minkowski metric $(+---)$.

2. As was first pointed out in Ref. [38], on p. 199 in Appendix E of Ref. [49], C_{22} and C_{23} were transposed. All reductions were rederived for this work, and the correct ordering is used below.

3. The numerical solutions to B'_0 in the subroutine `zffb0p` were derived analytically, and checked with the results of Aeppli [95] and Djouadi [43] where possible.

The tensor integrals used in the code below are defined as

$$A(m^2) = \frac{1}{i\pi^2} \int d^n q \frac{1}{(q^2 - m^2)} \, , \tag{B.1}$$

$$B_0; B_\mu(k^2, m_1^2, m_2^2) = \frac{1}{i\pi^2} \int d^n q \frac{1; q_\mu}{\left(q^2 - m_1^2\right)\left((q+k)^2 - m_2^2\right)} \, , \tag{B.2}$$

$$B_0'(k^2, m_1^2, m_2^2) = \frac{d}{dk^2} B_0(k^2, m_1^2, m_2^2) \tag{B.3}$$

$$C_0; C_\mu; C_{\mu\nu}(p_1^2, p_2^2, m_1^2, m_2^2, m_3^2) = \frac{1}{i\pi^2} \int d^n q$$

$$\times \frac{1; q_\mu; q_{\mu\nu}}{\left(q^2 - m_1^2\right)\left((q+p_1)^2 - m_2^2\right)\left((q+p_1+p_2)^2 - m_3^2\right)} \, , \tag{B.4}$$

$$D_0; D_\mu; D_{\mu\nu} = \frac{1}{i\pi^2} \int d^n q$$

$$\times \frac{1; q_\mu; q_{\mu\nu}}{\left(q^2 - m_1^2\right)\left((q+p_1)^2 - m_2^2\right)\left((q+p_1+p_2)^2 - m_3^2\right)\left((q+p_1+p_2+p_3)^2 - m_4^2\right)} \, . \tag{B.5}$$

where

$$B_\mu = k_\mu B_1 \, , \tag{B.6}$$

$$C_\mu = p_{1\mu} C_{11} + p_{2\mu} C_{12} \, , \tag{B.7}$$

$$C_{\mu\nu} = p_{1\mu} p_{1\nu} C_{21} + p_{2\mu} p_{2\nu} C_{22} + \{p_1 p_2\}_{\mu\nu} C_{23} + g_{\mu\nu} C_{24} \, , \tag{B.8}$$

$$D_\mu = p_{1\mu} D_{11} + p_{2\mu} D_{12} + p_{3\mu} D_{13} \, , \tag{B.9}$$

$$D_{\mu\nu} = p_{1\mu} p_{1\nu} D_{21} + p_{2\mu} p_{2\nu} D_{22} + p_{3\mu} p_{3\nu} D_{23} + \{p_1 p_2\}_{\mu\nu} D_{24}$$

$$+ \{p_1 p_3\}_{\mu\nu} D_{25} + \{p_2 p_3\}_{\mu\nu} D_{26} + g_{\mu\nu} D_{27} \, , \tag{B.10}$$

and $\{p,k\}_{\mu\nu} = p_\mu k_\nu + k_\mu p_\nu$.

```
C     File: zffbcd.f
C
C     This is a set of subroutines that evaluates B(mu), C(mu), C(mu,nu)
C      D(mu), or D(mu,nu) given the appropriate entries. The analytic
C      substitutions are from Passarino & Veltman pp. 196+.
```

```
C     NOTE: These functions are evaluated in the Minkowski metric.
C
C     NOTE: In dimensional regularization, terms appear as epsilon*fnc,
C          let epsilon == e
C          then: e*A0(m^2)           = m^2
C                e*B0(k^2,m1^2,m2^2)  = 1
C                e*B0p(k^2,mq^2,m2^2) = 0
C                e*B1(k^2,m1^2,m2^2)  = -1/2
C                e*C0(p1^2,p2^2,m1^2,m2^2,m3^2) = 0
C                e*C1(p1^2,p2^2,m1^2,m2^2,m3^2) => C11 = C12 => 0
C                e*C2(p1^2,p2^2,m1^2,m2^2,m3^2) => C21 = C22 = C23 => 0
C                                              C24 => 1/4
C                e*D0(pi^2,mi^2) = 0
C                e*D1(pi^2,mi^2) = 0
C
C     Subroutine zffb0p(cb0p,xk,xma,xmb,ier) calculates the value of B0p
C       for all cases except B0p(0;0,0).
C
C     Subroutine zffb1(cb1,ca0(2),cb0,d0,xmm,xk,xma,xmb,ier) calculates
C       the coefficients for B(mu) = k(mu)*cb1.
C
C     Subroutine zffc1(cc11,cc12,d0,xmm,xpi,ier) calculates the
C       coefficients for C(mu).
C
C     Subroutine zffc2(cc21,cc22,cc23,cc24,d0,xmm,xpi,ier) calculates
C       the coefficients for C(mu,nu).
C
C     Subroutine zffd1(cd1,xpi,ier) calculates the coefficients for D(mu).
C
C     Subroutine zffd2(cd2,d0,xmm,xpi,ier) calculates the coefficients
C      for D(mu,nu).
C
C     The subroutines call: ffxa0
C                           ffxb0
C                           ffxc0
C                           ffxd0
C
C     The file 'ff.h' is included.
C
C
      SUBROUTINE ZFFB0P(cb0p,xk,xma,xmb,ier)
C
C     Input: (xk=k^2), (xma=ma^2), (xmb=mb^2)
C
C     Returns: cb0p, ier
C
C     NOTE: Integral in FF-format
C
```

```
C      Most results are from the dissertation of Aeppli, 'Radiative
C        Corrections in the Electroweak Theory', Zurich 1992. ALL were
C        rederived by hand as a check. B0p(k,ma,mb) non-zero is from
C        Djouadi, PRD 48,7 p. 3088.
C
       implicit none
       integer ier
       double precision xk,xma,xmb
       double precision k,ma,mb
       double complex cp,cm
       double complex cb0p
C
       k = xk
       ma = xma
       mb = xmb
C      ** If xi < 1d-12 then xi = 0d0 **
       if (xk .lt. 1d-12) then
         k = 0d0
       endif
       if (xma .lt. 1d-12) then
         ma = 0d0
       endif
       if (xmb .lt. 1d-12) then
         mb = 0d0
       endif
C
C      ** k = 0 **
       if (k .lt. 1d-12) then
C        ** ma .eq. mb > 0 **
         if ((ma .eq. mb) .and. (ma .gt. 1d-12)) then
           cb0p = 1d0/6d0/ma
         else
C        ** ma .ne. mb , ma .or. mb = 0 **
           if ((ma .ne. mb) .and. (ma .lt. 1d-12)) then
             cb0p = 1d0/2d0/mb
           else
           if ((ma .ne. mb) .and. (mb .lt. 1d-12)) then
             cb0p = 1d0/2d0/ma
           else
C        ** ma .ne. mb , > 0 **
             if (ma. ne. mb) then
             cb0p = (ma+mb-2d0*ma*mb/(ma-mb)*log(ma/mb))/2d0/(ma-mb)**2
             else
C        ** ma = mb = 0 **
                 print *, 'ERROR> B0p (0,0,0) is not defined here.'
                 ier = 999
                 cb0p = 0d0
                 return
```

```fortran
                  endif
               endif
               endif
            endif
         else
C
C     ** k .ne. 0 **
C         ** ma = mb = 0 **
          if ((ma .lt. 1d-12) .and. (mb .lt. 1d-12)) then
            cb0p = -1d0/k
          else
C         ** ma .ne. mb, one is = 0, k .gt. other
            if (((k .gt. ma) .and. (mb .lt. 1d-12)) .or.
     1          ((k .gt. mb) .and. (ma .lt. 1d-12))) then
              print *,'ERROR> B0p(k,m,0), k > m is not defined here.'
              ier=999
              cb0p = 0d0
              return
            endif
C         ** ma .ne. mb , one is = 0, k .le. other **
            if ((ma .lt. 1d-12) .and. (k .le. mb)) then
              cb0p = -(1d0+mb/k*log(1d0-k/mb))/k
            else
              if ((mb .lt. 1d-12) .and. (k .le. ma)) then
                cb0p = -(1d0+ma/k*log(1d0-k/ma))/k
              else
C         ** ma .ne. mb > 0 **
C           ** p = m1+m2 is singular **
                if (abs(sqrt(k)-sqrt(ma)-sqrt(mb)) .lt. 1d-12) then
                 print *,'ERROR> B0p(p,m1,m2) is singular at p=m1+m2.'
                 cb0p =0d0
                 ier=999
                 return
                endif
C           ** m2 = p-m1 or m1 = p-m2 is special **
                if ((abs(sqrt(ma)-sqrt(k)-sqrt(mb)) .lt. 1d-12) .or.
     1              (abs(sqrt(mb)-sqrt(k)-sqrt(ma)) .lt. 1d-12)) then
                  cb0p = -(2d0+(mb-ma)/k*log(ma/mb)+2d0*(k-ma-mb)*(1d0/
     1                 (k+ma-mb)+1d0/(k+mb-ma)))/2d0/k
                  return
                endif
C           ** otherwise **
                  cp = k-ma-mb+sqrt(dcmplx(k**2-2*k*(ma+mb)+(ma-mb)**2))
                  cm = k-ma-mb-sqrt(dcmplx(k**2-2*k*(ma+mb)+(ma-mb)**2))
                  cb0p = -(2d0+(mb-ma)/k*log(ma/mb)+2d0/k*((ma-mb)**2-k*
     1                 (ma+mb))/(cp-cm)*log(cm/cp))/2d0/k
C
                endif
```

102

```fortran
            endif
          endif
        endif
C
C
      return
      end
C
C
      SUBROUTINE ZFFB1(cb1,ca0,cb0,d0,xmm,xk,xma,xmb,ier)
C
C     Input: (ca0(2)=a0(ma^2),a0(mb^2)), (cb0=b0(xk,xma,xmb)), d0, xmm,
C            (xk=k^2), (xma=ma^2), (xmb=mb^2)
C     Returns: cb1, ier
C
C     NOTE: Integral in FF-format
C
      implicit none
      integer ier
      double precision d0,xmm,xk,xma,xmb
      double complex ca0(2),cb0
      double complex cb1
C
      include '/home/theorist/theory/ff/ff.h'
C
C     ** xk < 1d-12 then xk = 0 **
C
      if (xk .lt. 1d-12) then
        if (xma .eq. xmb) then
          cb1 = -(d0 - log(xma/xmm))/2d0
        else
C     ** xma .neq. xmb **
          cb1 = -(d0 + 1d0/2d0 - xma/(xmb-xma) - xma**2*log(xma/
     1          xmb)/(xmb-xma)**2 - log(xmb/xmm))/2d0
        endif
      else
C
        cb1 = (ca0(1)-ca0(2)-(xk-xmb+xma)*cb0)/(2d0*xk)
C
      endif
      return
      end
C
C
      SUBROUTINE ZFFC1(cc11,cc12,d0,xmm,xpi,ier)
C
C     Input: d0,xmm, (xpi=m1^2,m2^2,m3^2,p1^2,p2^2,p3^2)
C     Calls: ffxb0, ffxc0
```

```
C     Returns: cc11, cc12, ier
C
      implicit none
      integer ier, i
      double precision d0,xmm,xpi(6)
      double complex cc11,cc12
      double complex cb012,cb013,cb023,cc0,r1,r2
      double precision f1,f2,xxdet,x12,xx(2,2)
C
      include '/home/theorist/theory/ff/ff.h'
C
C     Simple error trapping:  Uncomment to debug.
C
C      do 10 i=1,6
C         if (xpi(i) .lt. 0) then
C            print *, 'xpi',i,' < 0 needs to be handled another way.'
C            cc11 = 1d0
C            cc12 = 1d0
C            return
C         endif
C 10   continue
C
C     Call B0 functions
C
      call ffxb0(cb012,d0,xmm,xpi(4),xpi(1),xpi(2),ier)
      call ffxb0(cb013,d0,xmm,xpi(6),xpi(1),xpi(3),ier)
      call ffxb0(cb023,d0,xmm,xpi(5),xpi(2),xpi(3),ier)
C
C     Call C0
C
      call ffxc0(cc0,xpi,ier)
C
      f1 = -xpi(1) + xpi(2) - xpi(4)
      f2 = -xpi(2) + xpi(3) - xpi(6) + xpi(4)
C
      r1 = (cc0*f1 + cb013 - cb023)/2d0
      r2 = (cc0*f2 + cb012 - cb013)/2d0
      x12 = (xpi(6) - xpi(4) - xpi(5))/2d0
      xxdet = xpi(4)*xpi(5) - x12**2
      xx(1,1) = xpi(5)/xxdet
      xx(2,2) = xpi(4)/xxdet
      xx(1,2) = -x12/xxdet
      xx(2,1) = xx(1,2)
C
      cc11 = xx(1,1)*r1 + xx(1,2)*r2
      cc12 = xx(2,1)*r1 + xx(2,2)*r2
C
      return
```

```
      end
C
C
      SUBROUTINE ZFFC2(cc21,cc22,cc23,cc24,d0,xmm,xpi,ier)
C
C     Input: d0,xmm, (xpi=m1^2,m2^2,m3^2,p1^2,p2^2,p3^2)
C     Calls: ffax0, ffxb0, ffxc0, zffb1
C     Returns: cc21, cc22, cc23, cc24, ier
C
      implicit none
      integer ier, i
      double precision d0,xmm,xpi(6)
      double complex cc21,cc22,cc23,cc24
      double complex ca01,ca02,ca03,cc23b,temp23
      double complex cc11,cc12,ca0(2)
      double complex cb012,cb013,cb023,cc0,r1,r2
      double complex cb112,cb113,cb123,r3,r4,r5,r6
      double precision f1,f2,xxdet,x12,xx(2,2)
C
      include '/home/theorist/theory/ff/ff.h'
C
C     Simple error trapping:  Uncomment to debug.
C
C      do 10 i=1,6
C        if (xpi(i) .lt. 0) then
C          print *, 'xpi',i,' < 0 needs to be handled another way.'
C          cc21 = 1d0
C          cc22 = 1d0
C          cc23 = 1d0
C          cc24 = 1d0
C          return
C        endif
C 10   continue
C
C     Call A0 functions
C
      call ffxa0(ca01,d0,xmm,xpi(1),ier)
      call ffxa0(ca02,d0,xmm,xpi(2),ier)
      call ffxa0(ca03,d0,xmm,xpi(3),ier)
C
C     Call B0 functions
C
      call ffxb0(cb012,d0,xmm,xpi(4),xpi(1),xpi(2),ier)
      call ffxb0(cb013,d0,xmm,xpi(6),xpi(1),xpi(3),ier)
      call ffxb0(cb023,d0,xmm,xpi(5),xpi(2),xpi(3),ier)
C
C     Call C0
C
```

105

```
      call ffxc0(cc0,xpi,ier)
C
C     Define B1 functions
C
      ca0(1) = ca01
      ca0(2) = ca02
      call zffb1(cb112,ca0,cb012,d0,xmm,xpi(4),xpi(1),xpi(2),ier)
      ca0(2) = ca03
      call zffb1(cb113,ca0,cb013,d0,xmm,xpi(6),xpi(1),xpi(3),ier)
      ca0(1) = ca02
      call zffb1(cb123,ca0,cb023,d0,xmm,xpi(5),xpi(2),xpi(3),ier)
C     Note:
C      cb112 = (ca01-ca02-(xpi(4)-xpi(2)+xpi(1))*cb012)/(2d0*xpi(4))
C      cb113 = (ca01-ca03-(xpi(6)-xpi(3)+xpi(1))*cb013)/(2d0*xpi(6))
C      cb123 = (ca02-ca03-(xpi(5)-xpi(3)+xpi(2))*cb023)/(2d0*xpi(5))
C
      f1 = -xpi(1) + xpi(2) - xpi(4)
      f2 = -xpi(2) + xpi(3) - xpi(6) + xpi(4)
C
      r1 = (cc0*f1 + cb013 - cb023)/2d0
      r2 = (cc0*f2 + cb012 - cb013)/2d0
      x12 = (xpi(6) - xpi(4) - xpi(5))/2d0
      xxdet = xpi(4)*xpi(5) - x12**2
      xx(1,1) = xpi(5)/xxdet
      xx(2,2) = xpi(4)/xxdet
      xx(1,2) = -x12/xxdet
      xx(2,1) = xx(1,2)
C
C     Define C1 functions
C
      cc11 = xx(1,1)*r1 + xx(1,2)*r2
      cc12 = xx(2,1)*r1 + xx(2,2)*r2
C
C     Define C2 functions
C
      cc24 = 0.25d0 + cc0*xpi(1)/2d0 + (cb023 - f1*cc11 - f2*cc12)/4d0
C
      r3 = (f1*cc11 + cb113 + cb023)/2d0 - cc24
      r4 = (f1*cc12 + cb113 - cb123)/2d0
      r5 = (f2*cc11 + cb112 - cb113)/2d0
      r6 = (f2*cc12 - cb113)/2d0 - cc24
C
      cc21 = xx(1,1)*r3 + xx(1,2)*r5
      cc22 = xx(2,1)*r4 + xx(2,2)*r6
      cc23 = xx(2,1)*r3 + xx(2,2)*r5
C
C     Check C23
C
```

106

```
      cc23b = xx(1,1)*r4 + xx(1,2)*r6
      temp23 = (cc23+cc23b)/2d0
      cc23 = temp23
C      if (abs(1d0-cc23b/cc23) .ge. 1d-2) then
C       print *,'ERROR in C23-C23b =',abs(1d0-cc23b/cc23)
C      endif
C
      return
      end
C
C
      SUBROUTINE ZFFD1(cd1,xpi,ier)
C
C     Input: (xpi=m1^2,m2^2,m3^2,m4^2,p1^2,p2^2,p3^2,p4^2,
C                 (p1+p2)^2,(p2+p3)^2)
C                 NOTE: All momenta are positive coming in,
C                       labelled as in FF.
C     Calls: ffxc0, ffxd0
C     Returns: cd1(1), cd1(2), cd1(3), ier
C
      implicit none
      integer ier, i
      double precision xpi(13),xpj(6)
      double complex cd1(3)
      double complex cd0,cc0134,cc0234,cc0124,cc0123,r20,r21,r22
      double precision f1,f2,f3,xxdet,xxinv(3,3)
      double precision m1,m2,m3,m4,p1,p2,p3,p4,p12,p13,p23,p5,p6
C
      include '/home/theorist/theory/ff/ff.h'
C
C     Simple error trapping:  Uncomment to debug.
C
C      do 10 i=1,8
C         if (xpi(i) .lt. 0) then
C           print *, 'xpi',i,' < 0 needs to be handled another way.'
C           cd1(1) = 1d0
C           cd1(2) = 1d0
C           cd1(3) = 1d0
C           return
C         endif
C 10   continue
C
      m1 = xpi(1)
      m2 = xpi(2)
      m3 = xpi(3)
      m4 = xpi(4)
      p1 = xpi(5)
      p2 = xpi(6)
```

107

```
      p3 = xpi(7)
      p4 = xpi(8)
      p5 = xpi(9)
      p6 = xpi(10)
      p12 = (p5 - p1 - p2)/2d0
      p23 = (p6 - p2 - p3)/2d0
      p13 = (p2 + p4 - p5 - p6)/2d0
C
C     Call C0
C
      xpj(1) = m1
      xpj(2) = m3
      xpj(3) = m4
      xpj(4) = p5
      xpj(5) = p3
      xpj(6) = p4
      call ffxc0(cc0134,xpj,ier)
C
      xpj(1) = m2
      xpj(4) = p2
      xpj(5) = p3
      xpj(6) = p6
      call ffxc0(cc0234,xpj,ier)
C
      xpj(1) = m1
      xpj(2) = m2
      xpj(4) = p1
      xpj(5) = p6
      xpj(6) = p4
      call ffxc0(cc0124,xpj,ier)
C
      xpj(3) = m3
      xpj(4) = p1
      xpj(5) = p2
      xpj(6) = p5
      call ffxc0(cc0123,xpj,ier)
C
C     Call D0
C
      ier=0
      call ffxd0(cd0,xpi,ier)
C
C
C     Define D11,D12,D13
C
      xxdet = p1*p2*p3-p3*p12**2-p2*p13**2-p1*p23**2+2d0*p12*p13*p23
      xxinv(1,1) = (p2*p3 - p23**2)/xxdet
      xxinv(1,2) = (p23*p13 - p3*p12)/xxdet
```

108

```
      xxinv(1,3) = (p12*p23 - p2*p13)/xxdet
      xxinv(2,1) = xxinv(1,2)
      xxinv(2,2) = (p1*p3 - p13**2)/xxdet
      xxinv(2,3) = (p12*p13 - p1*p23)/xxdet
      xxinv(3,1) = xxinv(1,3)
      xxinv(3,2) = xxinv(2,3)
      xxinv(3,3) = (p1*p2 - p12**2)/xxdet
C
      f1 = m2 - m1 - p1
      f2 = m3 - m2 + p1 - p5
      f3 = m4 - m3 - p4 + p5
C
      r20 = (f1*cd0 + cc0134 - cc0234)/2d0
      r21 = (f2*cd0 + cc0124 - cc0134)/2d0
      r22 = (f3*cd0 + cc0123 - cc0124)/2d0
C
      cd1(1) = xxinv(1,1)*r20 + xxinv(1,2)*r21 + xxinv(1,3)*r22
      cd1(2) = xxinv(2,1)*r20 + xxinv(2,2)*r21 + xxinv(2,3)*r22
      cd1(3) = xxinv(3,1)*r20 + xxinv(3,2)*r21 + xxinv(3,3)*r22
C
      return
      end
C
C
      SUBROUTINE ZFFD2(cd2,d0,xmm,xpi,ier)
C
C     Input: d0,xmm, (xpi=m1^2,m2^2,m3^2,m4^2,p1^2,p2^2,p3^2,p4^2,
C                     (p1+p2)^2,(p2+p3)^2)
C             NOTE: All momenta are positive coming in,
C                     labelled as in FF.
C     Calls: zffc1, ffxc0, ffxd0
C     Returns: cd2(1), cd2(2), cd2(3), cd2(4), cd2(5), cd2(6),
C              cd2(7), ier
C
      implicit none
      integer ier, i
      double precision xpi(13),xpj(6),d0,xmm
      double complex cd1(3),cd2(7)
      double complex cd0,cc0134,cc0234,cc0124,cc0123,r20,r21,r22
      double complex c11134,c12134,c11234,c12234,c11124,c12124
      double complex c11123,c12123
      double complex r30,r31,r32,r33,r34,r35,r36,r37,r38
      double precision f1,f2,f3,xxdet,xxinv(3,3)
      double precision m1,m2,m3,m4,p1,p2,p3,p4,p12,p13,p23,p5,p6
      double complex temp,cd24,cd25,cd26
C
      include '/home/theorist/theory/ff/ff.h'
C
```

```
C     Simple error trapping:  Uncomment to debug.
C
C      do 10 i=1,8
C         if (xpi(i) .lt. 0) then
C            print *, 'xpi',i,' < 0 needs to be handled another way.'
C            cd2(1) = 1d0
C            cd2(2) = 1d0
C            cd2(3) = 1d0
C            cd2(4) = 1d0
C            cd2(5) = 1d0
C            cd2(6) = 1d0
C            cd2(7) = 1d0
C            return
C         endif
C 10   continue
C
      m1 = xpi(1)
      m2 = xpi(2)
      m3 = xpi(3)
      m4 = xpi(4)
      p1 = xpi(5)
      p2 = xpi(6)
      p3 = xpi(7)
      p4 = xpi(8)
      p5 = xpi(9)
      p6 = xpi(10)
      p12 = (p5 - p1 - p2)/2d0
      p23 = (p6 - p2 - p3)/2d0
      p13 = (p2 + p4 - p5 - p6)/2d0
C
C     Call C0
C
      xpj(1) = m1
      xpj(2) = m3
      xpj(3) = m4
      xpj(4) = p5
      xpj(5) = p3
      xpj(6) = p4
      call ffxc0(cc0134,xpj,ier)
      call zffc1(c11134,c12134,d0,xmm,xpj,ier)
C
      xpj(1) = m2
      xpj(4) = p2
      xpj(5) = p3
      xpj(6) = p6
      call ffxc0(cc0234,xpj,ier)
      call zffc1(c11234,c12234,d0,xmm,xpj,ier)
C
```

```fortran
      xpj(1) = m1
      xpj(2) = m2
      xpj(4) = p1
      xpj(5) = p6
      xpj(6) = p4
      call ffxc0(cc0124,xpj,ier)
      call zffc1(c11124,c12124,d0,xmm,xpj,ier)
C
      xpj(3) = m3
      xpj(4) = p1
      xpj(5) = p2
      xpj(6) = p5
      call ffxc0(cc0123,xpj,ier)
      call zffc1(c11123,c12123,d0,xmm,xpj,ier)
C
C     Call D0
C
      ier=0
      call ffxd0(cd0,xpi,ier)
C
C
C     Define D11,D12,D13
C
      xxdet = p1*p2*p3-p3*p12**2-p2*p13**2-p1*p23**2+2d0*p12*p13*p23
      xxinv(1,1) = (p2*p3 - p23**2)/xxdet
      xxinv(1,2) = (p23*p13 - p3*p12)/xxdet
      xxinv(1,3) = (p12*p23 - p2*p13)/xxdet
      xxinv(2,1) = xxinv(1,2)
      xxinv(2,2) = (p1*p3 - p13**2)/xxdet
      xxinv(2,3) = (p12*p13 - p1*p23)/xxdet
      xxinv(3,1) = xxinv(1,3)
      xxinv(3,2) = xxinv(2,3)
      xxinv(3,3) = (p1*p2 - p12**2)/xxdet
C
      f1 = m2 - m1 - p1
      f2 = m3 - m2 + p1 - p5
      f3 = m4 - m3 - p4 + p5
C
      r20 = (f1*cd0 + cc0134 - cc0234)/2d0
      r21 = (f2*cd0 + cc0124 - cc0134)/2d0
      r22 = (f3*cd0 + cc0123 - cc0124)/2d0
C
      cd1(1) = xxinv(1,1)*r20 + xxinv(1,2)*r21 + xxinv(1,3)*r22
      cd1(2) = xxinv(2,1)*r20 + xxinv(2,2)*r21 + xxinv(2,3)*r22
      cd1(3) = xxinv(3,1)*r20 + xxinv(3,2)*r21 + xxinv(3,3)*r22
C
C     Define D21,D22,D23,D24,D25,D26,D27
C
```

```fortran
      cd2(7) = m1*cd0 - (f1*cd1(1)+f2*cd1(2)+f3*cd1(3)-cc0234)/2d0
C
      r30 = (f1*cd1(1) + c11134 + cc0234)/2d0 - cd2(7)
      r31 = (f2*cd1(1) + c11124 - c11134)/2d0
      r32 = (f3*cd1(1) + c11123 - c11124)/2d0
      r33 = (f1*cd1(2) + c11134 - c11234)/2d0
      r34 = (f2*cd1(2) + c12124 - c11134)/2d0 - cd2(7)
      r35 = (f3*cd1(2) + c12123 - c12124)/2d0
      r36 = (f1*cd1(3) + c12134 - c12234)/2d0
      r37 = (f2*cd1(3) + c12124 - c12134)/2d0
      r38 = (f3*cd1(3) - c12124)/2d0 - cd2(7)
C
      cd2(1) = xxinv(1,1)*r30 + xxinv(1,2)*r31 + xxinv(1,3)*r32
      cd2(4) = xxinv(2,1)*r30 + xxinv(2,2)*r31 + xxinv(2,3)*r32
      cd2(5) = xxinv(3,1)*r30 + xxinv(3,2)*r31 + xxinv(3,3)*r32
      cd24 = xxinv(1,1)*r33 + xxinv(1,2)*r34 + xxinv(1,3)*r35
      cd2(2) = xxinv(2,1)*r33 + xxinv(2,2)*r34 + xxinv(2,3)*r35
      cd2(6) = xxinv(3,1)*r33 + xxinv(3,2)*r34 + xxinv(3,3)*r35
      cd25 = xxinv(1,1)*r36 + xxinv(1,2)*r37 + xxinv(1,3)*r38
      cd26 = xxinv(2,1)*r36 + xxinv(2,2)*r37 + xxinv(2,3)*r38
      cd2(3) = xxinv(3,1)*r36 + xxinv(3,2)*r37 + xxinv(3,3)*r38
C
      temp = (cd2(4) + cd24)/2d0
      cd2(4) = temp
      temp = (cd2(5) + cd25)/2d0
      cd2(5) = temp
      temp = (cd2(6) + cd26)/2d0
      cd2(6) = temp
C
      return
      end
C
C     End of file: zffbcd.f
C
```

Appendix C

Next-to-leading order structure functions

The structure functions for the charged-current production of a heavy quark were calculated at next-to-leading order many years ago in Ref. [96]. This calculation was recently repeated in Ref. [97], which discovered a misprint in the previous result, and also adopted the modern convention of treating the gluon as having $N-2$ helicity states in N dimensions. We verified the structure functions, and present them below for completeness.

Our calculation utilizes the charged-current structure functions for top-quark production, $F_i(x, Q^2)$ ($i = 1, 2, 3$), calculated in the $\overline{\text{MS}}$ scheme. The bottom-quark mass is neglected throughout. To make contact with Refs. [96, 97] we define a related set of structure functions, $\mathcal{F}_i(x, Q^2)$, via $F_1 \equiv \mathcal{F}_1$, $F_2 \equiv 2x\mathcal{F}_2$, and $F_3 \equiv 2\mathcal{F}_3$. These structure functions are related to the parton distribution functions by

$$
\mathcal{F}_i^q(x, Q^2) = q(x, \mu^2) + \frac{\alpha_s(\mu^2)}{2\pi} \int_x^1 \frac{dz}{z} \left[H_i^q(z, Q^2, \mu^2, \lambda) q\left(\frac{x}{z}, \mu^2\right) \right.
$$
$$
\left. + H_i^g(z, Q^2, \mu^2, \lambda) g\left(\frac{x}{z}, \mu^2\right) \right], \quad \text{(C.1)}
$$

where

$$
\lambda = \frac{Q^2}{Q^2 + m_t^2} . \quad \text{(C.2)}
$$

Table C.1: Coefficients in the expression for $h_i^q(z, \lambda)$.

i	A_i	$B_{1,i}$	$B_{2,i}$	$B_{3,i}$
1	0	$1 - 4z + z^2$	$z - z^2$	$\frac{1}{2}$
2	K_A	$2 - 2z^2 - \frac{2}{z}$	$\frac{2}{z} - 1 - z$	$\frac{1}{2}$
3	0	$-1 - z^2$	$1 - z$	$\frac{1}{2}$

The coefficient function for real and virtual gluon emission (Fig. 3.3) is

$$H_i^q(z, Q^2, \mu^2, \lambda) = P_{qq}(z) \ln \frac{Q^2 + m_t^2}{\mu^2} + h_i^q(z, \lambda),\tag{C.3}$$

where[1]

$$P_{qq}(z) = \frac{4}{3} \left(\frac{1 + z^2}{1 - z} \right)_+,\tag{C.4}$$

$$h_i^q(z, \lambda) = \frac{4}{3} \left\{ h^q + A_i \delta(1 - z) + B_{1,i} \frac{1}{(1 - z)_+} \right.$$
$$\left. + B_{2,i} \frac{1}{(1 - \lambda z)_+} + B_{3,i} \left[\frac{1 - z}{(1 - \lambda z)^2} \right]_+ \right\},\tag{C.5}$$

$$h^q = -\left(4 + \frac{1}{2\lambda} + \frac{\pi^2}{3} + \frac{1 + 3\lambda}{2\lambda} K_A \right) \delta(1 - z)$$
$$- \frac{(1 + z^2) \ln z}{1 - z} + (1 + z^2) \left[\frac{2 \ln(1 - z) - \ln(1 - \lambda z)}{1 - z} \right]_+,\tag{C.6}$$

$$K_A = \frac{1}{\lambda}(1 - \lambda) \ln(1 - \lambda).\tag{C.7}$$

The coefficients in the expression for $h_i^q(z, \lambda)$ are given in Table C.1.

---

[1] The expression for h^q corrects a misprint in Ref. [97], where the $\pi^2/3$ term was written as $\pi^3/3$.

Table C.2: Coefficients in the expression for $h_i^g(z,\lambda)$.

i	$C_{1,i}$	$C_{2,i}$	$C_{3,i}$	$C_{4,i}$
1	$4 - 4(1-\lambda)$	$\frac{(1-\lambda)z}{1-\lambda z} - 1$	2	-4
2	$8 - 18(1-\lambda)$ $+ 12(1-\lambda)^2$	$\frac{1-\lambda}{1-\lambda z} - 1$	6λ	-12λ
3	$2(1-\lambda)$	0	$-2(1-z)$	2

The coefficient function for initial gluons [Figs. 3.2(b), 3.2(c)] is

$$H_{i=\frac{1,2}{3}}^g(z,Q^2,\mu^2,\lambda) \;=\; P_{qg}(z)\left(\pm L_\lambda + \ln\frac{Q^2+m_t^2}{\mu^2}\right) + h_i^g(z,\lambda)\,, \qquad \text{(C.8)}$$

where

$$P_{qg}(z) \;=\; \frac{1}{2}\left[z^2 + (1-z)^2\right]\,, \qquad \text{(C.9)}$$

$$L_\lambda \;=\; \ln\frac{1-\lambda z}{(1-\lambda)z}\,, \qquad \text{(C.10)}$$

$$h_i^g(z,\lambda) \;=\; C_0 + C_{1,i}z(1-z) + C_{2,i} + (1-\lambda)zL_\lambda(C_{3,i} + \lambda z C_{4,i})\,, \qquad \text{(C.11)}$$

$$C_0 \;=\; P_{qg}(z)\left[2\ln(1-z) - \ln(1-\lambda z) - \ln z\right]\,. \qquad \text{(C.12)}$$

The coefficients in the expression for $h_i^g(z,\lambda)$ are given in Table C.2.

The explicit logarithms in $H_i^q(z,Q^2,\mu^2,\lambda)$ and $H_i^g(z,Q^2,\mu^2,\lambda)$ show that the appropriate scale for the process is $\mu^2 = Q^2 + m_t^2$, as discussed in Sec. 3.2.

The structure functions for light quarks (Fig. 3.4) in the $\overline{\text{MS}}$ scheme can be obtained from these expressions by taking $m_t \to 0$ ($\lambda \to 1$). This limit is unambiguous, except for

the factor L_λ; the correct substitution is

$$L_\lambda \quad \rightarrow \quad \ln \frac{1-z}{z} \, . \qquad\qquad (C.13)$$

References

[1] CDF Collaboration, F. Abe *et al.*, Phys. Rev. D **50**, 2966 (1994); Phys. Rev. Lett. **73**, 225 (1994).

[2] CDF Collaboration, F. Abe *et al.*, Phys. Rev. Lett. **74**, 2626 (1995); D0 Collaboration, S. Abachi *et al.*, Phys. Rev. Lett. **74**, 2632 (1995).

[3] M. Kobayashi and T. Maskawa, Prog. Theor. Phys. **49**, 652 (1973); N. Cabibbo, Phys. Rev. Lett. **10**, 531 (1963).

[4] R. Raja, talk given at the *XXXII Rencontres de Moriond on Electroweak Interactions and Unified Theories*, Les Arcs, Savoie, France, March 15–22, 1997; M. Cobal, talk given at the *Fifth Topical Seminar on the Irresistible Rise of the Standard Model*, San Miniato, Tuscany, Italy, April 21–25, 1997; CDF Collaboration, D. Gerdes, FERMILAB-CONF-96/342-E. Proceedings of the 1996 DPF/DPB Summer Study, "New Directions for High Energy Physics," Snowmass, CO, June 25-July 12, 1996.

[5] "Future of Electroweak Physics at the Fermilab Tevatron: Report of the tev_2000 Study Group", edited by D. Amidei and R. Brock, FERMILAB-PUB-96/082, 1996.

[6] R. M. Barnett, *et al.*, *Review of Particle Properties*, Phys. Rev. D **54**, 1 (1996)and 1997 off-year partial update for the 1998 edition available on the PDG WWW pages (URL: http://pdg.lbl.gov).

[7] Zack Sullivan, Phys. Rev. D **56**, 451 (1997).

[8] T. Stelzer, Z. Sullivan, and S. Willenbrock, Phys. Rev. D **56**, 5919 (1997).

[9] T. Stelzer, Z. Sullivan, and S. Willenbrock, ILL-(TH)-97-8, in preparation.

[10] E. Witten, Nucl. Phys. **B188**, 513 (1981).

[11] M. Drees and S. Martin, hep-ph/9504324.

[12] H. Haber and G. Kane, Phys. Rep. **117**, 75 (1985).

[13] For reviews, see H. P. Nilles, Phys. Rep. **110**, 1 (1984); P. Nath, R. Arnowitt, and A. Chamseddine, *Applied N=1 Supergravity*, ICTP series in Theoretical Physics, (World Scientific, Singapore, 1984)

[14] See references in J. Amundson *et al.*, in Proceedings of the 1996 DPF/DPB Summer Study on High Energy Physics, Snowmass, June 25–July 12, 1996, eds. D. Cassel, L. T. Gennari, and R. H. Siemann (Stanford Linear Accelerator Center, 1997), p. 655.

[15] J. Ellis and S. Rudaz, Phys. Lett. B **128**, 248 (1983); A. Bouquet, J. Kaplan and C. Savoy, Nucl. Phys. **B262**, 299 (1985).

[16] ALEPH Collaboration, "Searches for scalar top and scalar bottom quarks at LEP2", ALEPH Ref. 622.

[17] OPAL Collaboration, "Search for scalar top and scalar bottom quarks at $\sqrt{S} = 170$–172 GeV in e^+e^- collisions", Report No. CERN-PPE/97-046.

[18] ALEPH Collaboration, "Preliminary ALEPH results at 183 GeV", ALEPH Ref. 856.

[19] D0 Collaboration, S. Abachi *et al.*, Phys. Rev. Lett. **75**, 618 (1995).

[20] CDF Collaboration, F. Abe *et al.*, Phys. Rev. Lett. **76**, 2006 (1996).

[21] H1 Collaboration, S. Aid *et al.*, Phys. Lett. B **380**, 461 (1996).

[22] D0 Collaboration, S. Abachi *et al.*, Phys. Rev. Lett. **76**, 2222 (1996).

[23] G. C. Cho, Y. Kizukuri, N. Oshimo, Phys. Lett. B **372**, 101 (1996).

[24] A. Datta, M. Guchait, and N. Parua, Phys. Lett. B **395**, 54 (1997)and references therein.

[25] J. Bagger, hep-ph/9508392 (1995).

[26] R. Hempfling, hep-ph/9506408.

[27] D. Carlson and C.-P. Yuan, Phys. Lett. B **306**, 386 (1993).

[28] D. Carlson, E. Malkawi, and C.-P. Yuan, Phys. Lett. B **337**, 145 (1994).

[29] D. Atwood, S. Bar-Shalom, G. Eilam, and A. Soni, Phys. Rev. D **54**, 5412 (1996).

[30] A. Datta and X. Zhang, Phys. Rev. D **55**, 2530 (1997).

[31] C. S. Li, R. Oakes, and J. M. Yang, Phys. Rev. D **55**, 1672 (1997); Phys. Rev. D **55**, 5780 (1997).

[32] E. Simmons, Phys. Rev. D **55**, 5494 (1997).

[33] G. Lu Y. Cao, J. Huang, J. Zhang, and Z. Xiao, hep-ph/9701406.

[34] A. Datta, J. Yang, B.-L. Young, and X. Zhang, Phys. Rev. D **56**, 3107 (1997).

[35] T. Tait and C.-P. Yuan, hep-ph/9710372.

[36] P. Tipton, presented at the XXVIII International Conference on High-Energy Physics, Warsaw, Poland, July 1996.

[37] J. Sender, Phys. Rev. D **54**, 3271 (1996).

[38] M. Smith and S. Willenbrock, Phys. Rev. D **54**, 6696 (1996).

[39] G. Mahlon and S. Parke, Phys. Rev. D **55**, 7249 (1997).

[40] I. Bigi, Y. Dokshitzer, V. Khoze, J. Kühn, and P. Zerwas, Phys. Lett. B **181**, 157 (1986).

[41] M. Jeżabek, Nucl. Phys. B (Proc. Suppl.) **37B**, 197 (1994).

[42] P. Nason, S. Dawson, and R. K. Ellis, Nucl. Phys. **B303**, 607 (1988); Nucl. Phys. **B327**, 49 (1989); W. Beenakker, H. Kuijf, W. van Neerven, and J. Smith, Phys. Rev. D **40**, 54 (1989); W. Beenakker, W. van Neerven, R. Meng, G. Schuler, and J. Smith, Nucl. Phys. **B351**, 507 (1991); E. Laenen, J. Smith, and W. van Neerven, Nucl. Phys. **B369**, 543 (1992); Phys. Lett. B **321**, 254 (1994); S. Catani, M. Mangano, P. Nason, and L. Trentadue, Phys. Lett. B **378**, 329 (1996); hep-ph/9604351; E. Berger and H. Contopanagos, Phys. Lett. B **361**, 115 (1995); Phys. Rev. D **54**, 3085 (1996).

[43] A. Djouadi, M. Drees, and H. König, Phys. Rev. D **48**, 3081 (1993).

[44] C. Li, B. Hu, J. Yang, and C. Hu, Phys. Rev. D **52**, 5014 (1995); **53**, 4112(E) (1996).

[45] J. Kim, J. Lopez, D. V. Nanopoulos, and R. Rangarajan, Phys. Rev. D **54**, 4364 (1996).

[46] S. Alam, K. Hagiwara, and S. Matsumoto, Phys. Rev. D **55**, 1307 (1997).

[47] W. Marciano, Nucl. Phys. B (Proc. Suppl.) **11**, 5 (1989).

[48] C. Li, C.-P. Yuan, H. Zhou, hep-ph/9709275.

[49] G. Passarino and M. Veltman, Nucl. Phys. **B160**, 151 (1979).

[50] G. J. van Oldenborgh, Comp. Phys. Comm. **66**, 1 (1991).

[51] A. D. Martin, W. J. Stirling, and R. G. Roberts, Phys. Rev. D **51**, 4756 (1995).

[52] H. Lai, J. Botts, J. Huston, J. Morfin, J. Owens, J. Qiu, W.-K. Tung, and H. Weerts, Phys. Rev. D **51**, 4763 (1995).

[53] W. Marciano, Phys. Rev. D **29**, 580 (1984).

[54] G. 't Hooft and M. Veltman, Nucl. Phys. **B153**, 365 (1979).

[55] C. Itzykson and J. Zuber, *Quantum Field Theory* (McGraw-Hill, New York, 1980), p. 311.

[56] J. Ellis and D. Ross, Phys. Lett. B **383**, 187 (1996).

[57] S. Cortese and R. Petronzio, Phys. Lett. B **253**, 494 (1991).

[58] T. Stelzer and S. Willenbrock, Phys. Lett. B **357**, 125 (1995).

[59] S. Willenbrock and D. Dicus, Phys. Rev. D **34**, 155 (1986).

[60] C.-P. Yuan, Phys. Rev. D **41**, 42 (1990).

[61] R. K. Ellis and S. Parke, Phys. Rev. D **46**, 3785 (1992).

[62] G. Bordes and B. van Eijk, Nucl. Phys. **B435**, 23 (1995).

[63] CTEQ Collaboration, J. Botts, J. Morfin, J. Owens, J. Qiu, W.-K. Tung, and H. Weerts, Phys. Lett. B **304**, 159 (1993).

[64] J. Collins and W.-K. Tung, Nucl. Phys. **B278**, 934 (1986).

[65] J. Lindfors, Phys. Lett. B **167**, 471 (1986).

[66] T. Han, G. Valencia, and S. Willenbrock, Phys. Rev. Lett. **69**, 3274 (1992).

[67] F. Olness and W.-K. Tung, Nucl. Phys. **B308**, 813 (1988); M. Aivazis, J. Collins, F. Olness, and W.-K. Tung, Phys. Rev. D **50**, 3102 (1994).

[68] R. Barnett, H. Haber, and D. Soper, Nucl. Phys. **B306**, 697 (1988).

[69] M. Aivazis, J. Collins, F. Olness, and W.-K. Tung, Phys. Rev. D **50**, 3102 (1994).

[70] CTEQ Collaboration, H. Lai, J. Huston, S. Kuhlmann, F. Olness, J. Owens, D. Soper, W.-K. Tung, and H. Weerts, Phys. Rev. D **55**, 1280 (1997).

[71] J. Smith, hep-ph/9708212.

[72] C.-P. Yuan, in *6th Mexican School of Particles and Fields*, edited by J. D'Olivo, M. Moreno, and M. Perez (World Scientific, Singapore, 1995), p. 16; D. Carlson, hep-ph/9508278.

[73] A. Heinson, A. Belyaev, and E. Boos, Phys. Rev. D **56**, 3114 (1997).

[74] J. van der Bij and U. Baur, Nucl. Phys. **B304**, 451 (1988).

[75] G. Schuler, Nucl. Phys. **B229**, 21 (1988).

[76] J. van der Bij and G. J. van Oldenborgh, Z. Phys. C **51**, 477 (1991).

[77] J. Huston, S. Kuhlmann, H. L. Lai, F. Olness, J. Owens, D. Soper, and W.-K. Tung, hep-ph/9801444.

[78] M. Dittmar, F. Pauss, and D. Zürcher, Phys. Rev. D **56**, 7284 (1997).

[79] S. Moretti, Phys. Rev. D **56**, 7427 (1997).

[80] W. Giele, S. Keller, and E. Laenen, Phys. Lett. B **372**, 141 (1996).

[81] HERWIG by G. Marchesini, B. Webber, G. Abbiendi, I. Knowles, M. Seymour, L. Stanco, Comp. Phys. Comm. **67**, 465 (1992); hep-ph/9607393.

[82] PYTHIA by T. Sjostrand, Comp. Phys. Comm. **82**, 74 (1994); hep-ph/9508391.

[83] A. Stange, W. Marciano, and S. Willenbrock, Phys. Rev. D **49**, 1354 (1994); **50**, 4491 (1994).

[84] T. Stelzer and W. F. Long, Comp. Phys. Comm. **81**, 357 (1994).

[85] P. Nason, S. Dawson and R. K. Ellis, Nucl. Phys. **B303**, 607 (1988); **327**, 49 (1989); Erratum **B335**, 260 (1990).

[86] W. Beenakker, H. Kuijf, W. van Neerven, and J. Smith, Phys. Rev. D **40**, 54 (1989); R. Meng, G. Schuler, J. Smith, and W. van Neerven, Nucl. Phys. **B339**, 325 (1990); W. Beenakker, W. van Neerven, R. Meng, G. Schuler, and J. Smith, Nucl. Phys. **B351**, 507 (1991).

[87] S. Catani, M. Mangano, P. Nason, L. Trentadue, Phys. Lett. B **378**, 329 (1996); Nucl. Phys. **B478**, 273 (1996); hep-ph/9801375.

[88] E. Laenen, J. Smith, and W. van Neerven, Nucl. Phys. **B369**, 543 (1992).

[89] E. Berger and H. Contopanagos, Phys. Lett. B **361**, 115 (1995); Phys. Rev. D **54**, 3085 (1996); **57**, 253 (1998).

[90] W.-M. Yao, in *Proceedings of the 1996 DPF/DPB Summer Study on New Directions for High-Energy Physics*, Snowmass, eds. D. Cassel, L. Gennari, and R. Siemann (SLAC, 1997), p. 619.

[91] ATLAS Technical Proposal, CERN/LHCC/94-43, p. 98.

[92] R. Frey, hep-ex/9710016.

[93] V. Barger, K. Cheung, T. Han, and D. Zeppenfeld, Phys. Rev. D **44**, 2701 (1991); Erratum, **48**, 5444 (1993).

[94] N. Fabiano, hep-ph/9704261.

[95] A. Aeppli, *Radiative Corrections in the Electroweak Theory*, (Zurich 1992), p. 113.

[96] T. Gottschalk, Phys. Rev. D **23**, 56 (1981).

[97] M. Glück, S. Kretzer, and E. Reya, Phys. Lett. B **380**, 171 (1996).

Vita

Zack Edward Sullivan was born on August 11, 1971, in New York City, New York to James Ferguson Sullivan and Lana Shaw Levine. After graduating from Fieldston High School, Riverdale, New York, in 1989 he entered the Johns Hopkins University in Baltimore, Maryland. While completing his degree, he held the Arthur R. and Rena A. Knipp Scholarship for Excellence in the Fields of Physics and Mathematics. He was awarded the Donald E. Kerr Medal for the Most Outstanding Undergraduate in Physics. He received the degree of Bachelor of Arts with majors in physics and mathematics from the Johns Hopkins University in June, 1993, with general honors.

In September, 1993, he entered the University of Illinois at Urbana-Champaign to pursue a degree in theoretical particle physics. In October, 1994, he was awarded the degree of Master of Science from the University of Illinois at Urbana-Champaign. He worked as both a Teaching Assistant, and Research Assistant in 1993 – 1995, and 1997 – 1998. From 1995 until 1997, he held a GAANN Fellowship from the U.S. Department of Education. A list of his publications follows.

Publications in Refereed Journals

- "Supersymmetric QCD correction to top-quark production at the Fermilab Tevatron", Phys. Rev. D **56**, 451 (1997).

- "Single-top-quark production via W-gluon fusion at next-to-leading order" (with T. Stelzer and S. Willenbrock), Phys. Rev. D **56**, 5919 (1997).

- "Single-top-quark production at hadron colliders" (with T. Stelzer and S. Willenbrock), ILL-(TH)-97-8, in preparation.

Publications in Conference Proceedings

- "Top Quark Physics: Future Measurements" (with R. Frey, *et al.*), in *Proceedings of the 1996 DPF/DPB Summer Study on High Energy Physics*, Snowmass, June 25–July 12, 1996, eds. D. Cassel, L. T. Gennari, and R. H. Siemann (Stanford Linear Accelerator Center, 1997), p. 760.

- "Supersymmetric QCD correction to top-quark production at the Tevatron," in *Proceedings of the 1996 DPF/DPB Summer Study on High Energy Physics*, Snowmass, June 25–July 12, 1996, eds. D. Cassel, L. T. Gennari, and R. H. Siemann (Stanford Linear Accelerator Center, 1997), p. 797.